UNIVERSITY OF CALIFORNIA,
IRVINE

Air Pollution Impacts on the Global Methane and Ozone Budgets

DISSERTATION

submitted in partial satisfaction of the requirements
for the degree of

DOCTOR OF PHILOSOPHY

in Earth System Science

by

Calum Wilson

Dissertation Committee:
Professor Michael Prather, Chair
Professor Eric Saltzman
Professor Alex Guenther
Associate Professor Kim Saewung

2026

DEDICATION

To the family, friends, and mentors who supported me along the way.

In memory of Francois Primeau

TABLE OF CONTENTS

LIST OF FIGURES

Page

LIST OF TABLES

Page

ACKNOWLEDGMENTS

The text of Chapter 2 of this dissertation is a reprint of the material as it appears in Wilson, C. P. and Prather, M. J.: Gridded surface O3, NOx, and CO abundances for model metrics from the South Korean ground station network, Atmospheric Measurement Techniques, 18, 1757–1769, https://doi.org/10.5194/amt-18-1757-2025, 2025, used with permission from Copernicus Publications on behalf of the European Geosciences Union (CC BY 4.0). Michael Prather directed and supervised research which forms the basis for the dissertation.

The text of Chapter 3 of this dissertation is a reprint of the material as it appears in Wilson, C. P. and Prather, M. J.: Life–cycle impacts of South Korean air pollution on tropospheric ozone and methane: sensitivity to dispersion time, Atmospheric Chemistry and Physics, 26, 3995–4017, https://doi.org/10.5194/acp-26-3995-2026, 2026, used with permission from Copernicus Publications on behalf of the European Geosciences Union (CC BY 4.0). Michael Prather directed and supervised research which forms the basis for the dissertation.

The text of Chapter 4 of this dissertation is a reprint of the material as it appears in Wilson, C. P. and Prather, M. J.: Impact of urban-industrial air pollution on chemically reactive greenhouse gases is highly sensitive to organic nitrate formation, Atmospheric Chemistry and Physics, n.d., used with permission from Copernicus Publications on behalf of the European Geosciences Union (CC BY 4.0). Michael Prather directed and supervised research which forms the basis for the dissertation.

The text of Chapter 5 of this dissertation is adapted from the material as it appears in Prather, M. J. and Wilson, C. P.: Projecting nitrous oxide over the 21st century, uncertainty related to stratospheric loss, Proceedings of the National Academy of Sciences, 123, e2524123123, https://doi.org/10.1073/pnas.2524123123, 2026., used with permission from Proceedings of the National Academy of Sciences of the United States of America (CC BY 4.0). Michael Prather conducted the research, and Calum Wilson cowrote the paper that forms the basis for this dissertation.

Financial support was provided by the University of California, Irvine, NSF Grant AGS-2135749, and NASA grant 80NSSC21K1454.

VITA

Calum Wilson

2017 MSci in Chemistry,
Imperial College London

2026 PhD in Earth System Science,
University of California, Irvine

FIELD OF STUDY
Atmospheric Chemistry

PUBLICATIONS
Wilson, C. P. and Prather, M. J.: Life–cycle impacts of South Korean air pollution on tropospheric ozone and methane: sensitivity to dispersion time, Atmospheric Chemistry and Physics, 26, 3995–4017, https://doi.org/10.5194/acp-26-3995-2026, 2026.

Wilson, C. P. and Prather, M. J.: Gridded surface O3, NOx, and CO abundances for model metrics from the South Korean ground station network, Atmospheric Measurement Techniques, 18, 1757–1769, https://doi.org/10.5194/amt-18-1757-2025, 2025.

Prather, M. J. and Wilson, C. P.: Projecting nitrous oxide over the 21st century, uncertainty related to stratospheric loss, Proceedings of the National Academy of Sciences, 123, e2524123123, https://doi.org/10.1073/pnas.2524123123, 2026.

MANUSCRIPTS
Wilson, C. P. and Prather, M. J.: Impact of urban-industrial air pollution on chemically reactive greenhouse gases is highly sensitive to organic nitrate formation, Atmospheric Chemistry and Physics, n.d.

DATASETS
Methane loss (L-CH_4) and tropospheric ozone (O_3) burden in response to a 10% KORUS-AQ emission perturbation in the UCI chemistry-transport model, https://doi.org/10.5061/dryad.djh9w0wgm, 2026. [Dataset]

Wilson, C.: Modelling system for computing the tropospheric O3 and CH4 perturbations from South Korean Emissions (KORUS-AQ period), https://doi.org/10.5061/dryad.f4qrfj78x, 2026. [Dataset]

Wilson, C.: KORUS-AQ gridded O3, NOx, and CO observations created using ground station data, https://doi.org/10.5061/DRYAD.SF7M0CGF5, 2024. [Dataset]

ABSTRACT OF THE DISSERTATION

Reactive Greenhouse Gas Chemistry caused by Urban and Industrial Pollution Plumes from South Korea

by
Calum Wilson
Doctor of Philosophy in Earth System Science
University of California, Irvine, 2026
Professor Michael Prather, Chair

Recent industrialisation across Asia has produced increased air pollution emissions, altering the chemistry of reactive greenhouse gases (GHGs) in the troposphere. We compute the additional loss of methane (L-CH_4) and net production of ozone (P-O_3) attributable to urban and industrial emissions from South Korea during the May-June Korea-US Air quality (KORUS-AQ) mission. We build a three-stage hybrid modelling system (HMS) equipped with detailed chemical mechanisms to simulate the full life-cycle of emissions over several months (Chapter 3). The first stage processes the fresh emissions in the well-mixed boundary layer over terrestrial South Korea. The model fields of O_3, carbon monoxide, and nitrogen oxides are compared with surface observation data, which are interpolated and gridded in Chapter 2 to match the model discretisation. The second stage integrates the chemistry of the transboundary pollution plumes transported offshore, and the final stage disperses the residual pollutants. We find that the KORUS-AQ summertime emissions cause +4.3 Gmol CH_4 loss and +31.2 Gmol net O_3 production, which are about 0.1% and 0.3% of the respective global budget terms during an equivalent time period. These reactivities are greatly amplified when pollution plumes are dispersed more rapidly. A parallel study using the UCI chemistry-transport model (CTM) reveals a similar integrated O_3 enhancement in both models, but with lower total P-O_3 and L-CH_4 by factors of 71% and 46% respectively (Chapter 4). The lower CTM values are attributed to insufficient organic nitrate formation near emission sources on account of simplified chemical mechanisms.

CHAPTER 1: INTRODUCTION

This atmospheric chemistry dissertation addresses the science question of how air pollution emissions change the reactivity of the reactive greenhouse gases (GHGs) in the atmosphere. The sources and sinks of methane (CH_4) and tropospheric ozone (O_3) have previously been budgeted in the global atmosphere (Saunois *et al*., 2025; Griffiths *et al*., 2020). However, these budgets do not isolate the chemical budgets perturbed by pollution plumes, and the models that were used might not accurately simulate pollution plume chemistry. The modelling work here resolves the CH_4 and O_3 budget alterations caused by 45 days of South Korean air pollution with higher chemical detail and horizontal resolution than the traditional models. This case study could serve as a benchmark for future model intercomparison with a focus on pollution plume GHG reactivity, which we demonstrate using a chemistry-transport model (CTM).

The dissertation contains two published first-author papers (Chapters 2 and 3), one first-author manuscript in preprint (Chapter 4), and one coauthored paper (Chapter 5). The present chapter provides scientific context for the work here (Section 1.1). Sections 1.2-1.6 are summaries of the published research findings, the challenges involved, and the research contributions of the dissertation author. The conclusion (Chapter 6) presents holistic findings from Chapters 2-5, their significance, and proposes avenues for future work.

1.1 Background

Since the pre-industrial era, GHG emissions have altered the balance of incoming and outgoing radiation through the top-of-atmosphere, placing the Earth on a warming trajectory. The dominant GHG, carbon dioxide, is rising due to fossil fuel emissions. The next most important GHGs are chemically reactive, methane (CH_4), ozone (O_3), and nitrous oxide (N_2O). They respectively account for 14%, 12%, and 5% of anthropogenic GHG forcing in the present

day (Forster *et al.*, 2021). The rise in reactive GHG abundances over the last century is mainly driven by direct emission of CH_4 and N_2O, and precursors of O_3. The O_3 precursor pollution, which includes nitrogen oxides (NO_x), carbon monoxide (CO), and volatile organic compounds (VOCs), has also altered the chemistry of the atmosphere and the CH_4 lifetime (Stevenson et al., 2020).

Air pollution from Asia is largely responsible for the recent rise in tropospheric O_3 burden which is concentrated over the Pacific (Gaudel *et al.*, 2018; Ziemke *et al.*, 2019). Generally, NO_x emissions promote O_3 formation by accelerating key pathways in radical-VOC chemistry of the free troposphere. This process directly increases the loss of CH_4 by converting hydroperoxyl (HO_2) to hydroxyl (OH) radical and by forming primary OH from the reaction of O_3 photolysis product with water vapour. Carbon monoxide and long-lived VOCs raise background O_3 slightly while suppressing OH. Radical abundance and NO_x-O_3 chemistry respond nonlinearly to emission intensity and dilution and are therefore impacted by spatial discretisation of the models (Zakoura and Pandis, 2018; Li *et al.*, 2023). Wild *et al.* (2004) showed that net O_3 production in urban outflow regions is largely independent of meteorological variability, but the study could not reproduce the high-percentile statistics of O_3 reactivity observed within pollution plumes. Another issue with air pollution modelling is chemical complexity. Most 3D models use abbreviated chemical mechanisms, and this treatment is appropriate in the remote troposphere where the large VOCs have mostly decayed. However, in the intensely polluted boundary layer, O_3 production and radical abundances are sensitive to the complexity of the VOC chemistry, particularly that of aromatic species (Oak *et al*., 2019).

High resolution GHG budgets have been previously computed for maritime shipping pollution. Charlton-Perez *et al.* (2009) found a large overestimation of CH_4-OH loss

(+60%) and tropospheric O_3 production (+30%) caused by ship plumes at the resolution of typical CTMs *vs*. large eddy simulation at a single tropical site. Holmes *et al*. (2014) evaluated the net radiative forcing caused by a global shipping NO_x using sub-grid parametric plume chemistry and found it to be reduced relative to instantly diluted emissions. Terrestrial air pollution is more challenging to simulate as it is enriched in VOCs from the biosphere and human industries, and the boundary layer dynamics are more complex over land. Budgets for tropospheric O_3 and CH_4 have been computed at global scale using all known emission sources (Griffiths *et al*., 2020; Saunois *et al*., 2025). However, the Earth system models that were used to derive the O_3 chemical budget – or the bottom-up CH_4-OH loss – are subject to the structural issues outlined above. The models might have inaccurately simulated the chemistry in the intensely polluted atmosphere as a consequence.

A large body of air pollution research has emerged from the Korea-US Air Quality (KORUS-AQ) mission of May-June 2016, where detailed *in situ* chemical observations of South Korean air pollution were collected via aircraft alongside surface air quality observations (O_3, CO, and NO_x). Much of the past KORUS-AQ research has focused on O_3 production near the urban and industrial sources in light of public health concern. This dissertation presents a GHG perspective on KORUS-AQ air pollution by modelling the resulting net production of O_3 (P-O_3) and loss of CH_4 (L-CH_4) over >120 days from emission to dispersion. The budget terms are integrated over a model run with KORUS-AQ emissions (Woo *et al*., 2020), and a control run is subtracted. The net production of O_3 is determined using calculated O_3 perturbation lifetimes, which include the lifetime feedbacks (Prather and Zhu, 2024).

We build a specialised hybrid modelling system (HMS; Chapter 3) that simulates the chemical evolution of air pollution across three dynamical stages with full MCM chemistry. The

first stage (BL-RL) models the mixture of pollution in the South Korean boundary layer and overlying residual layer on a refined grid. The processing of pollution in the BL-RL stage determines the initial composition of transboundary pollution plumes in the second (PL) stage. The BL-RL processes include boundary-layer dynamics, emissions, 2-layer horizontal transport, photochemistry, surface and aerosol deposition. In the subsequent PL stage, plumes that leave the South Korean shoreline are chemically aged over 0-to-3 days under standard meteorological conditions at 2 km altitude. The plumes are then dispersed in the final (DP) stage where the P-O_3 and L-CH_4 reactivities are calculated as a linear superposition of the individual residual pollutants. The HMS attributes significant net O_3 production and CH_4 loss to South Korean pollution.

The BL abundances of O_3, CO, and NO_x are validated using gridded KORUS-AQ surface observations derived in Chapter 2. We also test the accuracy and predictive capability of the interpolated fields via leave-one-out cross validation (LOOCV) and compare the gridded data with airborne transects in the boundary layer.

The overall HMS budget terms are greatly amplified when the plumes are aged for less time before dispersion (*e.g.*, after 1 day *vs*. 3 days of aging). We then pose the question of how well the GHG reactivities agree when calculated by a more conventional CTM. In Chapter 4 we perturb the UCI CTM with identical KORUS-AQ emissions, pre-processed to match the abbreviated CTM species. The integrated O_3 mass perturbation was similar in the CTM and HMS, but P-O_3 and L-CH_4 are lower in the CTM by factors 71% and 47% respectively. This result is surprising because the dilution of emissions in the coarser CTM grid was expected to amplify the budget terms (Charlton-Perez *et al.*, 2009; Holmes *et al.*, 2014). The airborne vertical profiling suggests insufficient organic nitrate formation in the polluted air of the CTM,

which decreases NO_x availability in the aged or dispersed plumes where P-O_3 and L-CH_4 are more NO_x-efficient.

This dissertation author is also a coauthor of Chapter 5, which discusses the trend in N_2O lifetime, the components of climate change driving the trend, and the range of N_2O projections by the year 2100 that emerge from the uncertainty in the projected trend.

1.2 Overview of Chapter 2: Gridded Observations for Model Metrics

This chapter describes and analyses the interpolation of surface air pollution observations (O_3, CO, and NO_x) in South Korea to obtain gridded data at the 10 km resolution of our hybrid model in Chapter 3. We apply the inverse distance weighting (IDW) technique of Schnell et al. (2014) and find significant mean absolute deviation between the IDW and the more common arithmetic mean gridded data in urban regions where the interpolation quality was demonstrably highest. We were also met with significant challenges. The surface site data are unprocessed, containing large spikes (errors) and lengthy dropouts that require careful treatment. Ideally, we would have used processed data that is allegedly available from the AirKorea website, but the data was publicly inaccessible. The interpolations were likely biased by roadside stations which we were unable to remove. We find inexplicably high CO readings by the network even in rural regions, which were biased by around +100 ppb relative to the aircraft and the Taehwa Forest wilderness research station. Such high mixing ratios are not reproduced in our modelling efforts, nor previous work (e.g., Kim *et al.*, 2024). Improvements in the CO and NO_x interpolation could be made using more sophisticated techniques as reviewed by Karroum *et al*. (2020). When testing an early version of the HMS (Chapter 3) against the gridded datasets, we found catastrophically high urban CO and NO_x because this version assumed most pollution was exported to the free troposphere via vertical boundary layer dynamics without the need for

horizontal transport. Upon recognising the importance of horizontal wind ventilation, we rebuilt the HMS with *u*, *v* transport and found much better agreement with the gridded observations.

This dissertation author applied the IDW technique, analysis, and wrote most of the paper; the PhD advisor strategised much of the analysis, edited the paper, and guided the review process.

1.3 Overview of Chapter 3: Life-Cycle Impacts of Air Pollution on Methane and Ozone

This Chapter reviews the HMS modelling of the life-cycle of KORUS-AQ air pollution in detail and integrates the budget terms (P-O_3 and L-CH_4) therein. The results from the paper confirm that summertime South Korean emissions cause significant additional GHG reactivity, impacting the global budgets. A range of plume dynamical lifetimes are tested from 0-3 days aging; we find the total budget terms are mostly converged after 2 days, and drastically amplified for shorter lifetimes (*i.e.*, 0-1 day or instant emission dispersion). These results suggest that global CH_4 and O_3 budget calculations could be overestimated in models with high numerical diffusion (Zhuang *et al*., 2018) and serve as a benchmark for future modelling efforts (e.g., Chapter 4). One limitation to the HMS is a lack of secondary aerosol chemistry, which is not available in MCM v3.3.1, but needed for modelling winter air pollution. Another limitation is the lack of resolved plume transport. The standard plume aging conditions reflect westerly transport above the marine boundary layer at 2 km, which is a probable trajectory, but assumes none of the plumes are lifted over fronts or warm conveyor during transport (Crawford *et al.*, 2004). Aging the plumes over a range of altitudes, as for the dispersed plumes, would reveal the importance of this model uncertainty and provide a better understanding of the dynamical and diverse lifecycle of pollution plumes.

The HMS was built using the Framework for 0-D Atmospheric Modeling (F0AM; Wolfe et al., 2016), chemical mechanisms from MCM v3.3.1, and data collected from KORUS-AQ and the ECMWF Copernicus program. The dissertation author built the model, conducted the analysis, and wrote the paper under the supervision of the PhD advisor, who contributed to the study strategy, paper edits, and reviewing.

1.4 Overview of Chapter 4: Chemistry-Transport vs. Hybrid Model Air Pollution Budgets

This chapter compares the budget terms (P-O_3 and L-CH_4) caused by KORUS-AQ emissions in the UCI CTM *vs*. the HMS in Chapter 3. The CTM and HMS produce similar integrated O_3 perturbations, but the CTM produces lower P-O_3 and L-CH_4. The sequestration of NO_x as organic nitrates is shown to increase ozone production efficiency (OPE) and methane destruction efficiency (MDE) in the HMS plumes as NO_x is slowly re-released into a cleaner environment. We identify missing net peroxyacetyl nitrate (PAN) formation in CTM pollution, caused by less reactive VOC representations, as the cause of muted P-O_3 and L-CH_4. Adding aromatic species to the CTM, or running the HMS with UCI chemistry, would substantiate our conclusion assuming it is correct. There is a difference in experimental approaches: the CTM runs a 10% KORUS-AQ emission perturbation on top of full CMIP5 emissions and scales the budgets by 10; the HMS runs the full KORUS-AQ emissions on top of clean air. Running 110% emissions in the HMS would test the linearity of the budget responses to the emissions.

The UCI CTM was developed by the PhD advisor and collaborators over decades. The dissertation author ran the CTM, adjusting model inputs and diagnostics, and analysed the model output. He drafted the manuscript described in this Chapter. The PhD advisor edited and reviewed the manuscript.

1.5 Overview of Chapter 5: Projecting Nitrous Oxide.

This chapter computes the trend in N_2O lifetime from microwave limb sounding (MLS) data over the last 20 years, updating the value to -1.4% dec^{-1}. The N_2O lifetime broadly depends on the rate of tropical upwelling, which trends upward, and the chemical kinetics of N_2O photolysis and $N_2O + O^1D$ oxidation. Modelling the vertical N_2O distribution due to increased tropical upwelling, combined with the change in N_2O reaction kinetics, produces a similar decadal lifetime trend to MLS-derived results. The magnitude of the lifetime trends found here result in substantially different N_2O projections in the year 2100.

The work in this chapter was carried out by the PhD advisor, with proof-reading and review by the dissertation author.

1.6 Praxis

The journey to producing the dissertation material is outlined here. The goal was to evaluate the impact of intense air pollution on the global CH_4 and O_3 budgets using KORUS-AQ data and extrapolate these terms globally. The DC-8 aircraft observed a plethora of chemical species across South Korea and the nearby oceans at 10 s (~200 m) resolution. Pollution from the Seoul Metropolitan Area, South coastal cities, and East coast points sources was targeted. The author developed the ability to integrate the chemistry of any air volume using the F0AM v3.1 photochemical box model. The first problem to emerge was how to define "pollution plumes" in the observations, and how representative the observations were of the actual atmosphere over Korea. Another concern was how the plumes age in the model *vs.* the real atmosphere.

We sought to build statistics on the sources and ages of KORUS-AQ pollution plumes using publicly available back trajectory data. Source attribution was a major challenge because the back-trajectories were represented as clusters with centroids and mean squared deviations of

particle spread. Attributing the likely source of a polluted aircraft segment became a geometry problem of integrating the overlap of circular clusters passing over rectilinear EDGAR grid cells. We were ultimately able to hash map the emission source cells to a range of observations and ages. However, the aircraft did not pursue South Korean pollution aged more than a few hours, so the statistics were, in the end, not useful for our analysis.

We then pursued the GHG budgets through the more principled approach of modelling the formation of pollution plumes from South Korea *ab initio*, *i.e.*, the hybrid modelling system (HMS). Based on the resolution of the KORUS v5 inventory grid, we constructed a box model using the ERA5 boundary layer height as a cap on vertical mixing. The collapse of the boundary layer at night would export air to the free troposphere as pollution plumes, while the rise in daytime mixing would entrain background air. Operators for horizontal turbulent mixing, emissions, photochemistry, surface- and aerosol deposition were constructed. Integrating the chemistry of the isolated plume exported plumes was straight-forward. The treatment of dispersed pollutants was a key novelty that posed some challenges. The behaviour of a perturbation to the background air was not realistic unless the background air composition were maintained, and so adding sources and sinks of background species was necessary. Optimising N chemical fluxes to maintain N specified background mixing ratios was challenging. Ultimately, our initial sequence of operations in the boundary layer was insufficient to ventilate the boundary layer, and super-concentrated urban pollution remained in urban grid cells.

We compared the model O_3, CO, and NO_x fields against KORUS-AQ surface observations as our primary model-observation metric. We applied the IDW interpolation of Schnell *et al*. (2014), optimising it for the South Korean surface network, and gridding the quasi-continuous fields to match our model. In order to test our interpolations against observations

(*e.g.*, excluded stations and aircraft transects), we had to decide on the appropriate metrics, of which there are several. Frequently used model-observation metrics include mean absolute deviation, root-mean-squared deviation, mean bias, min- and max- difference, Pearson's r and r^2, and the coefficient of determination (R^2). We used R^2, which describes the fraction of variance in the "truth" that is explained by the prediction after applying a regression. We consistently applied R^2 to three separate regressions on our data series: a "null" regression (no correction), mean bias correction, and ordinary least squares fitting (bias + slope correction). This provided three useful and related metrics.

Subsequent research efforts went into fixing the boundary layer of the hybrid modelling system. We realised that the horizontal ventilation timescales in the boundary layer were sub-hourly, and wind (u, v) transport would be needed. The new HMS transport scheme had to conserve mass onshore and in the fresh offshore plumes, maintain the vertically discrete boundary layer masses, and strain the emissions across the wind trajectories. The source-receptor relationships were eventually configured in the model start-up, and transport was realised as a linear algebra operation. Parallelising the boundary layer chemistry and running the model on the high performance computing (HPC) nodes posed challenges but was achieved with high CPU efficiency. Running the HMS on 10 HPC cores *vs*. 6 threads on a personal computer drastically sped up the simulation.

The author does not take knowledge for granted and has invested much thought into understanding the mathematical basis behind atmospheric chemistry concepts (*e.g.*, the unintuitive calculation of lifetime feedbacks). Learning to solve first-order matrix ordinary differential equations was perhaps the most important step towards understanding the timescales of a chemical system. In a tracked air mass, the lifetime of O_3 can be conceptualised as the

timescale with which an O_3 perturbation decays to the background level; a key advantage of the HMS was the ability to derive such lifetimes. In an Eulerian framework, the O_3 budget becomes confusing, as the timescales in the chemistry-transport system have spatial and temporal dimensions. Most literature separates O_3 production and loss using rates within the "odd-oxygen" family, and this framing has known problems that we avoid with our current model structure.

References

1. Charlton-Perez, C. L., Evans, M. J., Marsham, J. H., and Esler, J. G.: The impact of resolution on ship plume simulations with NO_x chemistry, Atmospheric Chemistry and Physics, 9, 7505–7518, https://doi.org/10.5194/acp-9-7505-2009, 2009.
2. Collins, W. J., Lamarque, J.-F., Schulz, M., Boucher, O., Eyring, V., Hegglin, M. I., Maycock, A., Myhre, G., Prather, M., Shindell, D., and Smith, S. J.: AerChemMIP: quantifying the effects of chemistry and aerosols in CMIP6, Geoscientific Model Development, 10, 585–607, https://doi.org/10.5194/gmd-10-585-2017, 2017.
3. Crawford, J. H., Heald, C. L., Fuelberg, H. E., Morse, D. M., Sachse, G. W., Emmons, L. K., Gille, J. C., Edward, D. P., Deeter, M. N., Chen, G., Olson, J. R., Connors, V. S., Kittaka, C., and Hamlin, A. J.: Relationship between Measurements of Pollution in the Troposphere (MOPITT) and in situ observations of CO based on a large-scale feature sampled during TRACE-P, Journal of Geophysical Research: Atmospheres, 109, https://doi.org/10.1029/2003JD004308, 2004.
4. Forster, P., T. Storelvmo, K. Armour, W. Collins, J.-L. Dufresne, D. Frame, D.J. Lunt, T. Mauritsen, M.D. Palmer, M. Watanabe, M. Wild, and H. Zhang, 2021: The Earth's Energy Budget, Climate Feedbacks, and Climate Sensitivity. In Climate Change 2021: The Physical Science Basis. Contribution of Working Group I to the Sixth Assessment Report of the Intergovernmental Panel on Climate Change [Masson-Delmotte, V., P. Zhai, A. Pirani, S.L.
5. Gaudel, A., Cooper, O. R., Ancellet, G., Barret, B., Boynard, A., Burrows, J. P., Clerbaux, C., Coheur, P.-F., Cuesta, J., Cuevas, E., Doniki, S., Dufour, G., Ebojie, F., Foret, G., Garcia, O., Granados-Muñoz, M. J., Hannigan, J. W., Hase, F., Hassler, B., Huang, G., Hurtmans, D., Jaffe, D., Jones, N., Kalabokas, P., Kerridge, B., Kulawik, S., Latter, B., Leblanc, T., Le Flochmoën, E., Lin, W., Liu, J., Liu, X., Mahieu, E., McClure-Begley, A., Neu, J. L., Osman, M., Palm, M., Petetin, H., Petropavlovskikh, I., Querel, R., Rahpoe, N., Rozanov, A., Schultz, M. G., Schwab, J., Siddans, R., Smale, D., Steinbacher, M., Tanimoto, H., Tarasick, D. W., Thouret, V., Thompson, A. M., Trickl, T., Weatherhead, E., Wespes, C., Worden, H. M., Vigouroux, C., Xu, X., Zeng, G., and Ziemke, J.: Tropospheric Ozone Assessment Report: Present-day distribution and trends of tropospheric ozone relevant to climate and global atmospheric chemistry model evaluation, Elementa: Science of the Anthropocene, 6, 39, https://doi.org/10.1525/elementa.291, 2018.

6. Griffiths, P. T., Murray, L. T., Zeng, G., Shin, Y. M., Abraham, N. L., Archibald, A. T., Deushi, M., Emmons, L. K., Galbally, I. E., Hassler, B., Horowitz, L. W., Keeble, J., Liu, J., Moeini, O., Naik, V., O'Connor, F. M., Oshima, N., Tarasick, D., Tilmes, S., Turnock, S. T., Wild, O., Young, P. J., and Zanis, P.: Tropospheric ozone in CMIP6 simulations, Atmospheric Chemistry and Physics, 21, 4187–4218, https://doi.org/10.5194/acp-21-4187-2021, 2021.
7. Holmes, C. D., Prather, M. J., and Vinken, G. C. M.: The climate impact of ship NO_x emissions: an improved estimate accounting for plume chemistry, Atmospheric Chemistry and Physics, 14, 6801–6812, https://doi.org/10.5194/acp-14-6801-2014, 2014.
8. Karroum, K., Lin, Y., Chiang, Y.-Y., Ben Maissa, Y., El Haziti, M., Sokolov, A., and Delbarre, H.: A Review of Air Quality Modeling, MAPAN, 35, 287–300, https://doi.org/10.1007/s12647-020-00371-8, 2020.
9. Kim, K.-M., Kim, S.-W., Seo, S., Blake, D. R., Cho, S., Crawford, J. H., Emmons, L. K., Fried, A., Herman, J. R., Hong, J., Jung, J., Pfister, G. G., Weinheimer, A. J., Woo, J.-H., and Zhang, Q.: Sensitivity of the WRF-Chem v4.4 simulations of ozone and formaldehyde and their precursors to multiple bottom-up emission inventories over East Asia during the KORUS-AQ 2016 field campaign, Geoscientific Model Development, 17, 1931–1955, https://doi.org/10.5194/gmd-17-1931-2024, 2024.
10. Li, C., Martin, R. V., Cohen, R. C., Bindle, L., Zhang, D., Chatterjee, D., Weng, H., and Lin, J.: Variable effects of spatial resolution on modeling of nitrogen oxides, Atmospheric Chemistry and Physics, 23, 3031–3049, https://doi.org/10.5194/acp-23-3031-2023, 2023.
11. Oak, Y. J., Park, R. J., Schroeder, J. R., Crawford, J. H., Blake, D. R., Weinheimer, A. J., Woo, J.-H., Kim, S.-W., Yeo, H., Fried, A., Wisthaler, A., and Brune, W. H.: Evaluation of simulated O3 production efficiency during the KORUS-AQ campaign: Implications for anthropogenic NOx emissions in Korea, Elementa: Science of the Anthropocene, 7, 56, https://doi.org/10.1525/elementa.394, 2019.
12. Prather, M. J. and Zhu, X.: Lifetimes and timescales of tropospheric ozone, Elementa: Science of the Anthropocene, 12, 00112, https://doi.org/10.1525/elementa.2023.00112, 2024.
13. Saunois, M., Martinez, A., Poulter, B., Zhang, Z., Raymond, P. A., Regnier, P., Canadell, J. G., Jackson, R. B., Patra, P. K., Bousquet, P., Ciais, P., Dlugokencky, E. J., Lan, X., Allen, G. H., Bastviken, D., Beerling, D. J., Belikov, D. A., Blake, D. R., Castaldi, S., Crippa, M., Deemer, B. R., Dennison, F., Etiope, G., Gedney, N., Höglund-Isaksson, L., Holgerson, M. A., Hopcroft, P. O., Hugelius, G., Ito, A., Jain, A. K., Janardanan, R., Johnson, M. S., Kleinen, T., Krummel, P. B., Lauerwald, R., Li, T., Liu, X., McDonald, K. C., Melton, J. R., Mühle, J., Müller, J., Murguia-Flores, F., Niwa, Y., Noce, S., Pan, S., Parker, R. J., Peng, C., Ramonet, M., Riley, W. J., Rocher-Ros, G., Rosentreter, J. A., Sasakawa, M., Segers, A., Smith, S. J., Stanley, E. H., Thanwerdas, J., Tian, H., Tsuruta, A., Tubiello, F. N., Weber, T. S., van der Werf, G. R., Worthy, D. E. J., Xi, Y., Yoshida, Y., Zhang, W., Zheng, B., Zhu, Q., Zhu, Q., and Zhuang, Q.: Global Methane Budget 2000–2020, Earth System Science Data, 17, 1873–1958, https://doi.org/10.5194/essd-17-1873-2025, 2025.
14. Schnell, J. L., Holmes, C. D., Jangam, A., and Prather, M. J.: Skill in forecasting extreme ozone pollution episodes with a global atmospheric chemistry model, Atmospheric Chemistry and Physics, 14, 7721–7739, https://doi.org/10.5194/acp-14-7721-2014, 2014.

15. Stevenson, D. S., Zhao, A., Naik, V., O'Connor, F. M., Tilmes, S., Zeng, G., Murray, L. T., Collins, W. J., Griffiths, P. T., Shim, S., Horowitz, L. W., Sentman, L. T., and Emmons, L.: Trends in global tropospheric hydroxyl radical and methane lifetime since 1850 from AerChemMIP, Atmospheric Chemistry and Physics, 20, 12905–12920, https://doi.org/10.5194/acp-20-12905-2020, 2020.
16. Wild, O., Prather, M. J., Akimoto, H., Sundet, J. K., Isaksen, I. S. A., Crawford, J. H., Davis, D. D., Avery, M. A., Kondo, Y., Sachse, G. W., and Sandholm, S. T.: Chemical transport model ozone simulations for spring 2001 over the western Pacific: Regional ozone production and its global impacts, Journal of Geophysical Research: Atmospheres, 109, https://doi.org/10.1029/2003JD004041, 2004.
17. Wolfe, G. M., Marvin, M. R., Roberts, S. J., Travis, K. R., and Liao, J.: The Framework for 0-D Atmospheric Modeling (F0AM) v3.1, Geosci. Model Dev., 9, 3309–3319, https://doi.org/10.5194/gmd-9-3309-2016, 2016.
18. Woo, J.-H., Kim, Y., Kim, H.-K., Choi, K.-C., Eum, J.-H., Lee, J.-B., Lim, J.-H., Kim, J., and Seong, M.: Development of the CREATE Inventory in Support of Integrated Climate and Air Quality Modeling for Asia, Sustainability, 12, 7930, https://doi.org/10.3390/su12197930, 2020.
19. Zakoura, M. and Pandis, S. N.: Overprediction of aerosol nitrate by chemical transport models: The role of grid resolution, Atmospheric Environment, 187, 390–400, https://doi.org/10.1016/j.atmosenv.2018.05.066, 2018.
20. Zhuang, J., Jacob, D. J., and Eastham, S. D.: The importance of vertical resolution in the free troposphere for modeling intercontinental plumes, Atmospheric Chemistry and Physics, 18, 6039–6055, https://doi.org/10.5194/acp-18-6039-2018, 2018.
21. Ziemke, J. R., Oman, L. D., Strode, S. A., Douglass, A. R., Olsen, M. A., McPeters, R. D., Bhartia, P. K., Froidevaux, L., Labow, G. J., Witte, J. C., Thompson, A. M., Haffner, D. P., Kramarova, N. A., Frith, S. M., Huang, L.-K., Jaross, G. R., Seftor, C. J., Deland, M. T., and Taylor, S. L.: Trends in global tropospheric ozone inferred from a composite record of TOMS/OMI/MLS/OMPS satellite measurements and the MERRA-2 GMI simulation, Atmospheric Chemistry and Physics, 19, 3257–3269, https://doi.org/10.5194/acp-19-3257-2019, 2019.

Chapter 2: Gridded surface O_3, NO_x, and CO abundances for model metrics from the South Korean ground station network

Calum P. Wilson[1], Michael J. Prather[1]

[1]Department of Earth System Science, University of California (Irvine), Irvine, CA 92697, USA

Correspondence to: Calum P. Wilson (calumw@uci.edu)

Abstract

We present gridded surface air quality datasets over South Korea for three key species – ozone (O_3), carbon monoxide (CO), and nitrogen oxides (NO_x) during the timeframe of the Korea–US Air Quality (KORUS–AQ) mission (May–June 2016). The tenth–degree hourly averaged abundances are constructed from the 300+ air quality network sites using inverse distance weighting with simple declustering. Cross–comparing the interpolated fields against the site data that was used to create them reveals high prediction skill for O_3 (80%) throughout South Korea, and moderate skill (60%) for CO and NO_x on average in densely observed regions after individual mean bias corrections. The gridded O_3 and CO interpolations predict the NASA DC–8 observations in the planetary boundary layer (PBL) with high skill (80%) in the Seoul Metropolitan Area (SMA) after subtracting the mean bias. DC–8 NO_x observations were much less predictable on account of consistently negative vertical gradients within the PBL. Our gridded products capture the mean and variability of O_3 throughout South Korea, and of CO and surface NO_x in most site–dense urban centres (SMA, Cheongju, Gwangju, Daegu, Changwon, and Busan).

1 Introduction

Air quality control has become a priority in the Republic of Korea following an upward trend in ozone (O_3) pollution in all major cities since the 1980s (Susaya et al., 2013). In May–June 2016,

the Korea–US Air Quality (KORUS–AQ) mission was launched with the goal of improving knowledge of the factors controlling Korean air pollution; this mission gathered extensive observational data via aircraft, ground stations, ships, and remote sensing (Crawford et al., 2021).

Comparisons of modelled grid–cell values (i.e., averages) with point data from station sites remains awkward, especially in high–emission environments with high sub–grid and temporal variability. Ground site comparisons in South Korea have thus far used the arithmetic mean of sites within a grid cell or ungridded quantile analysis (Lennartson et al., 2018; Peterson et al., 2019; Eck et al., 2020; Jordan et al., 2020; Schroeder et al., 2020; Park et al., 2021; Oak et al., 2022; Travis et al., 2022), but these unweighted means can be biased by site clustering, and they lose information outside the cells. In this work we develop a gridded dataset of key surface–level pollutants (in this case, O_3, NO_x, CO) observed during the KORUS–AQ timeframe. In contrast to arithmetic means, we apply Inverse Distance Weighting (IDW) interpolations (Shepard, 1968) improved by Schnell et al. (2014) to create a country–wide continuous mapping of the National Institute of Environmental Research (NIER) ground site data. We subsequently integrate the interpolated field over a 0.1°x0.1° grid. To evaluate the interpolation, we predict NIER station measurements using the leave–one–out cross validation method; we predict observations from two research sites (Olympic Park and Taehwa Forest) to verify instrumental cohesion; and, we compare our gridded fields with DC–8 observations within the planetary boundary layer (PBL) to gauge how well the data products reproduce upper PBL abundances. In addition to providing gridded PBL datasets, we discuss the applicability and limitations of our methodology for each key species.

The observational data sets are described in Section 2, and the methods in Section 3. Results are summarized in Section 4. Conclusions and recommendations are presented in Section 5.

2 KORUS–AQ data

All KORUS–AQ datasets introduced in this section including the raw five–minute NIER station data are available via https://doi.org/10.5067/Suborbital/KORUSAQ/DATA01. The NIER station data is access–controlled, but we record our processed hourly–averaged NIER station data and our quality control flags for the raw data in our repository (see Wilson, 2024).

2.1 NIER air quality stations

The AirKorea monitoring network (https://www.airkorea.or.kr/eng) provided ground measurements of the key species averaged every 5 minutes at 323 stations across South Korea, of which 319 reported O_3, 311 reported CO, and 321 reported NO_x (Fig. 1). We calculate hourly median readings centred on the hour for each station, but omit clearly erroneous O_3 and NO_x dropouts from the average. High outliers exceeding five standard deviations above the mean of a weekly period were also discarded along with dropouts, which were manifest as stably low concentrations (1–4 ppb) persisting for multiple hours in stark contrast with the typical variability at the site. We were able to flag most dropouts algorithmically by analyzing the cumulative density functions (CDFs) of the station data partitioned into non–overlapping weekly intervals; improbably frequent low data often featured flat empirical gradients (less than 100^{th} of the median CDF gradient) at the tail of the CDF. This technique proved insufficient at some stations however, and so we manually removed dropouts that were not flagged by our algorithm, as did Eck et al, 2020. The NIER instruments and procedures are not well documented and there remain some oddities: CO was reported with 1 ppb precision at 68 sites, and with 100 ppb precision at the remaining 250 sites.

2.2 Research stations

2.2.1 Olympic Park

The Olympic Park research station lies at the southeast edge of Seoul at 37.5216°N, 127.1242°E, 30 m above sea level, and served as a reference for ground–level Seoul pollution during the KORUS–AQ campaign (red star in Fig. 1). Hourly averages for the key species were recorded using NO_x–Ecotech EC9841, CO–Ecotech EC9830, and O_3–Ecotech EC9810 instruments (PI: Cho Seogu) during the KORUS–AQ period (10 May 01:00:00 to 18 June 00:00:00 LT). As Olympic Park station has four proximal NIER stations within 5 km, reproducing this research station data from the NIER interpolation should be a test of the small scale variability of Seoul pollution provided the instruments are well calibrated.

2.2.2 Taehwa Forest

The Taehwa Forest wilderness site lies 30 km southeast of Olympic Park at 37.3123°N, 127.3105°E and at 200 m elevation (blue star in Fig. 1). It was used primarily to investigate the mixing of urban Seoul pollution with the biogenic volatile organic compounds (BVOCs) of the forest. The three key species were measured by the existing NIER instruments (PI: Youngjae Li), but supplemented by a Thermo Scientific 42i instrument for NO and a Cavity Ring–Down Spectroscopy for NO_2 (PI: Kim Saewung, Kim et al., 2022).

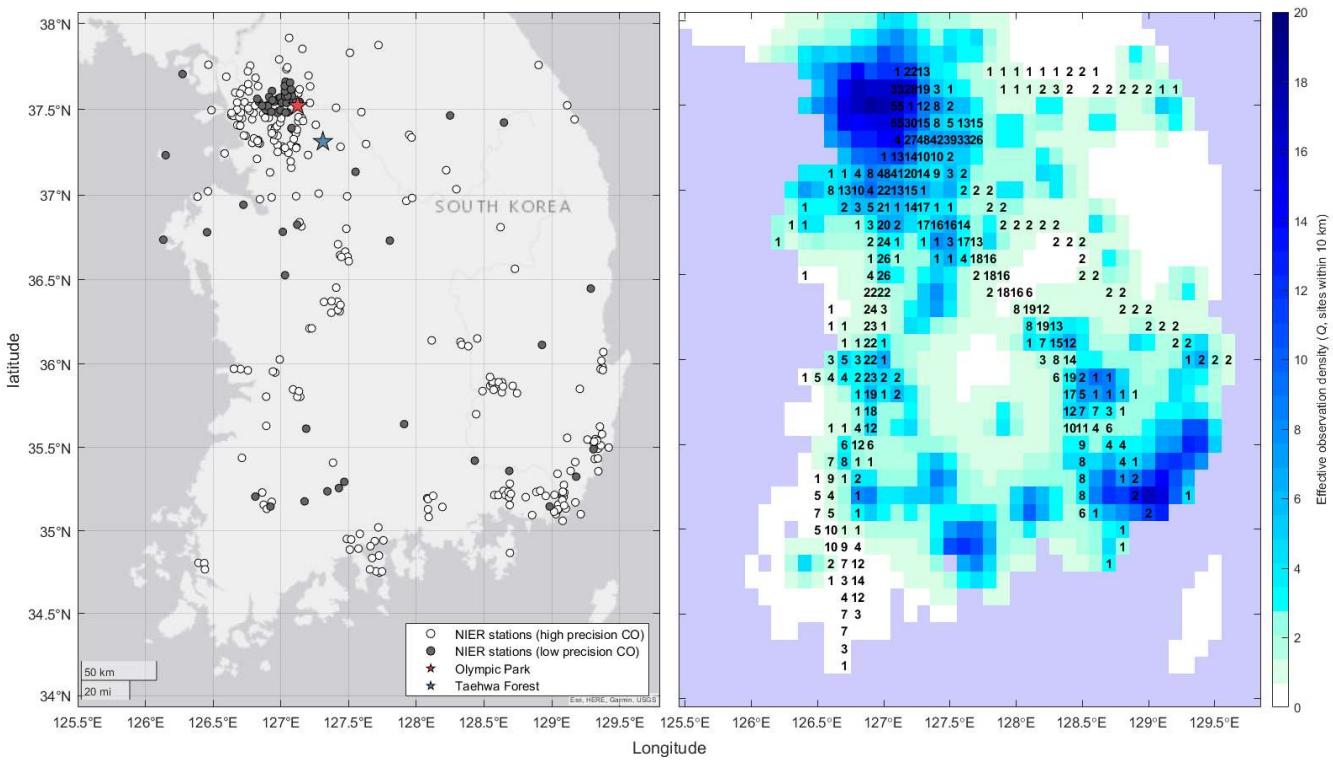

Figure 2.1: *(Left) The geographical distribution of NIER ground stations and the two surface research stations operating during the KORUS–AQ campaign.*

High–precision stations (white circles) recorded CO at 1 ppb precision; low–precision stations (grey circles) recorded CO at 100 ppb increments. (Right) Effective NIER station density (colour) within a 10 km radius (Q, see Eq. (3)) gridded over 0.1°x0.1° cells. The number of contiguous DC–8 flight transects through each box in the PBL is printed in each cell. The aircraft radar altitude was evaluated against the ERA5 PBL height (based on hourly 0.25°x0.25° gridded data, Hersbach et al., 2023). The ERA5 data was interpolated in time to match the aircraft data.

2.3 NASA DC–8

The DC–8 aircraft routinely profiled the air over Taehwa Forest via loop manoeuvres in the morning and afternoon on flight days between 2 May 2016 and 11 June 2016. It sampled other regions above South Korea and the Yellow Sea according to pollution plume transport and cloud forecasts. We use the 10 s merged data our three key species: O_3, NO, and NO_2 were measured with a 4–channel chemiluminescence instrument (Weinheimer et al., 1994); and CO, by Differential Absorption Carbon monOxide Measurement (DACOM) (Sachse et al., 1991). We

also use the 10 s data for latitude, longitude, radar altitude, UTC time, and potential temperature (PI: Melissa Yang). From the DC–8 potential temperature measurements and ERA5 surface data (Fig. A1) we can show that the ERA5 PBL heights accurately select DC–8 observations that are adiabatically mixed from the surface (i.e., $d\theta/dz \sim 0$), which is confirmed by the afternoon O_3 and CO profiles (Fig. A2). To determine when the aircraft was in the PBL and thus could be compared with the interpolated surface map, we use the ERA5 PBL height data from reanalysis (hourly, 0.25°x0.25° grid, Hersbach et al., 2023). This approach is more accurate than simply assuming that all DC–8 observations below 1.5 km radar altitude fall within the PBL (e.g., Oak et al., 2019).

3 Methods

Interpolation techniques compute an objective estimate $Z'(x,t)$ of a field $Z(x,t)$ at any geographic location x and time t as a weighted mean of observations $Z_k(t)$ at stations indexed by k with weights $w_k(x)$:

$$Z'(x,t) = \sum_k [w_k(x) Z_k(t)] \,/\, \sum_k w_k(x) \qquad (1)$$

Ordinary Kriging and Inverse Distance Weighting (IDW) are two common interpolation methods that operate by this premise but differ in how the station weights (w_k) are calculated (Matheron, 1963; Shepard, 1968). Kriging is a family of statistical techniques based on the supposition that phenomena are autocorrelated in space, relying on an empirical distance–based covariance model of $Z(x,t)$ determined from the station data. In our work we find minimal Pearson's correlation between pairwise site covariance and proximity for any of the key species, so we opt for the modified IDW approach of Schnell et al. (2014).

We examine the autocovariance functions of the sites to characterize the temporal variability of each key species at five–minute resolution. The autocovariance function for a given phase shift

(*e.g.* ten minutes) is defined as the covariance of a time series of data with itself, but phase–shifted by ten minutes. The O_3 site autocovariance functions feature strong diurnal cycles, preserving on average half of the respective site variances for a twenty–four–hour phase shift, compared with 35% for CO and NO_x. Sub–ten–minute variability accounts for 3% of the O_3 site variance and 12% of the CO and NO_x variance on average. Heterogeneous emissions and micrometeorology may be attributed to some of the CO and NO_x short timescale variability seen in some Seoul sites and many CO–measuring sites in Gwangyang–Yeosu–Suncheon zone, while rural sites suggest a possible instrumental noise component to the NO_x variability (See Fig. B of Appendix B).

3.1 Inverse Distance Weighting

In IDW techniques, weights are calculated from the reciprocal distances between estimation point x and the station coordinates x_k, scaled by the exponent β. The greater density of observations in some regions creates a source of oversampling bias. Schnell et al. (2014) address this clustering effect by reducing all station weights by M_k, the number of other stations within distance D of site k, discounting sites with missing readings on an hourly basis. In order to smooth the spatial heterogeneity in $Z'(x,t)$ at small length scales, the distance D also serves as the minimum cutoff of $x - x_k$, and hence determines the maximum weighting $w_k(x)$ of any nearby station. L is a maximum cutoff of $x - x_k$ used to reduce excess calculations for extremely distant and unimportant sites. The weight formulae are summarized in Eq. (2):

$$\begin{aligned} w_k(x) &= \frac{D^{-\beta}}{M_k} && x - x_k \le D \\ w_k(x) &= \frac{(x-x_k)^{-\beta}}{M_k} && D < x - x_k \le L \\ w_k(x) &= 0 && x - x_k > L \end{aligned} \qquad (2)$$

Our NIER station data consists of $k \in \{1, 2, \ldots, 323\}$ locations (Fig. 1) and $t \in \{1, 2, \ldots, 936\}$ hourly observations (10 May 01:00:00 to 18 June 00:00:00 LT) for each of our three key species (O_3, CO, NO_x) with some unreported or erroneous data. We optimize β and D for each key species Z by randomly removing a fifth of the stations from the algorithm and then predicting the abundance at each missing station k', adjusting each parameter until a 2D minimum was reached. In minimizing the total root–mean–square error between predictions $Z'_{k'}(t)$ and observations $Z_{k'}(t)$ over the time series, we find similar optimal values for each species ($\beta \sim 2$, $D \sim 5$ km, $L \sim$ 80 km), with no significant improvement for larger L. The *effective density of observations* $Q(x)$ is defined as the effective number of NIER sites within a 10 km radius of x in Eq. (3) (also called *Quality of prediction*, Eq. (5) of Schnell et al., 2014). We expect Q to correlate with prediction accuracy:

$$Q(x) = 10^{\beta} \sum_k w_k(x) \tag{3}$$

Compared with the arithmetic mean gridding, the gridded IDW observations show no significant mean bias. However, significant mean absolute deviations can be seen in the densely observed ($Q > 10$) Seoul Metropolitan Area and Southeast coastal cities. In such regions, the mean absolute deviations for O_3, CO, and NO_x are 5 ppb, 58 ppb, and 9 ppb respectively. Conversely, the most sparsely measured regions show the best agreement between the two methods due to mutual sampling of a single station. Both methods are fundamentally limited by sampling density, particularly in urban centres with high spatial emission variability. The differences seen in the most densely observed regions highlight the instability of the arithmetic mean method with respect to grid size and boundary manipulation.

3.2 Statistical techniques

To evaluate the accuracy and predictive capability of an interpolation, we examine the error $E(t)$ in a time series of predictions $Pre(t)$ and observations $Obs(t)$ at a given location for a given species with all time points equally weighted equally. We calculate a sequence of three error series defined as follows:

$$\begin{aligned} E1(t) &= Pre(t) - Obs(t) \\ E2(t) &= Pre(t) - Obs(t) - (\overline{Pre(t)} - \overline{Obs(t)}) \\ E3(t) &= b\,Pre(t) - Obs(t) - (b\,\overline{Pre(t)} - \overline{Obs(t)}) \end{aligned} \quad (4)$$

Where $E1(t)$ is the absolute error in the predictions, $E2(t)$ is the error after correcting for the mean prediction bias $(\overline{Pre(t)} - \overline{Obs(t)})$ and $E3(t)$ is the error relative to a simple linear regression (LR) model of $Pre(t)$ vs. $Obs(t)$ fitted by ordinary least squares, i.e., after correcting for mean bias and slope (b). We then apply the *coefficient of determination* to compute the fraction of the observed sample variance, $Var(Obs(t))$, explained by e.g. the raw predictions $(E1(t))$:

$$R^2_{E1} = 1 - \frac{Mean(E1(t)^2)}{Var(Obs(t))} \quad (5)$$

And do similarly for $E2(t)$ and $E3(t)$. R^2_{E1} is a *predictive accuracy* statistic that ranges from minus infinity to one and is identical to the forecast skill score referenced to the mean of observations (Murphy, 1988). R^2_{E2} describes how well the predictions capture the temporal variability in the observations regardless of any mean bias and has the same range as R^2_{E1}. R^2_{E3} is the common definition of R^2 in regression analysis and ranges from zero to one due to the fitting constraint. R^2_{E3} describes the *predictability* of the observations from the LR model regardless of any difference in the mean or variance of $Pre(t)$ and $Obs(t)$. A score of zero for a given R^2_E is equivalent to predicting a static mean of observations across the time domain. The

maximum score for R^2_{E1} and R^2_{E2} is limited by the interpolation variance, which is typically damped relative to the contributing stations, especially in regions with highly heterogeneous emissions. Figure 2 (right–hand side) suggests the average station predictability (R^2_{E1} and R^2_{E2}) score has an upper bound of around 0.9 for O_3 and 0.8 for CO and NO_x.

3.2.1 Leave–one–out cross validation.

In this trial, we sequentially remove each station k, then interpolate (predict) its value from the remaining stations: $Pre(k,t) = Z'(k,t)$, where $Obs(k,t) = Z(k,t)$ (see Eq. (4); Brauer et al, 2003; Hochadel et al., 2006). A perfect interpolation would accurately reproduce the mean and standard deviation of the measurements, indicating (1) no mean bias error and (2) preservation of daily maximae and minimae. Our optimized IDW interpolation has clearly worked well in terms of mean bias (left half of Fig. 2). The box quartiles and non–outlier whiskers (i.e., the full range of values within one–and–a–half interquartile ranges from the outer quartiles) are well centred on zero bias, with the spread broadening from O_3 to CO to NO_x. The symmetry of the whiskers comes from the case where two sites, distant from the remaining sites but near one another, are the only sites used to interpolate one another and hence if one site has twice the mean value of another, we get symmetric plus–minus biases for each site. The median of the mean NO_x site biases is +13%, and this appears to be an artefact of low NO_x abundances in rural ($Q < 5$) locations. The absolute mean NO_x bias averages –0.6 ppb (urban –3.0 ppb, rural +6.5 ppb). Incoherence among nearby urban stations combines to dampen the interpolation variability, especially for CO and NO_x, which feature independent high spatial variability from local sources. This is shown on the right half of Fig. 2, where most of the standard deviation ratio quantiles lie below unity. We believe this reduced standard deviation in the prediction time series better represents the average over a grid cell that contains several incoherent sites.

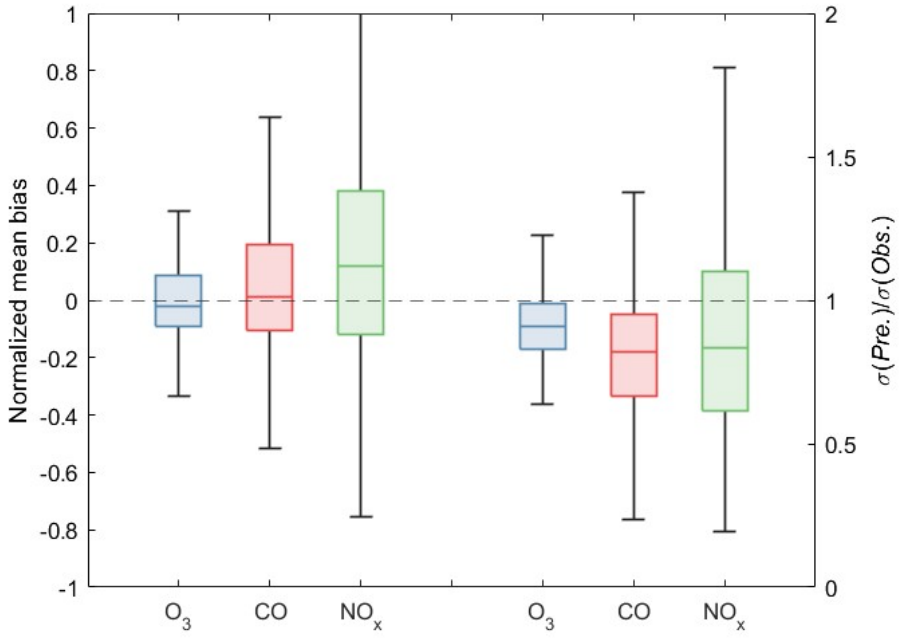

Figure 2.2: *(left) Box plots of normalized mean bias:* $NMB(k) = Mean(Pre(k,t) - Obs(k,t))/Mean(Obs(k,t))$ *and (right) standard deviation ratio* $\sigma(Pre(k,t))/\sigma(Obs(k,t))$ *for interpolated time series at each NIER site using leave–one–out cross validation.*

Whiskers show the range of non–outliers, where outliers are data beyond one–and–a–half interquartile ranges from the outer quartiles. Results are shown for O_3 (blue), CO (red), and NO_x (green). Mean bias is normalized by the observed mean, and the ratio of standard deviations is analogous to the gradient of a linear regression.

The sequence of R^2_E scores ($E1$–3) for each site and each species are shown in Fig. 3. The O_3 scores (top row) are consistently high across the sequence. R^2_{E1} through R^2_{E3} scores for O_3 indicate that the O_3 interpolation was accurate and unbiased at almost all NIER stations in South Korea. For CO (middle row) and NO_x (bottom row), there is an improvement in absolute prediction accuracy (R^2_{E1}) as the density of observations (Q) increases, and further improvement after correcting the mean bias in the predictions (R^2_{E2}). The linear regression models (R^2_{E3}) offer an obvious improvement to predictability in rural regions (low Q) where information is lacking, but no significant improvement in well sampled urban regions (high Q). With no large net mean

bias for any key species (Fig. 2), we assert that the average of our interpolations should capture the mean and possibly the variability of a well–mixed gridded domain. We test this assertion later using aircraft PBL observations averaged into 0.1°x0.1° cells. The high range of R^2_E values for NO_x and CO, even where $Q > 10$, suggests that absolute mean error in the prediction is a problem for many sites, implying they are driven by very small scale (<1 km) local emissions in contrast to O_3, which is not emitted directly. For NO_x, the sequence from *E1* to *E2* greatly improves the prediction accuracy. For CO, there remains a large fraction of unpredictable sites, often with very high standard deviations (dark red circles), implying large nearby emissions. Figure 4 (top–middle and top–right panels) shows the clustering of such sites for CO and NO_x in Daejeon (central–western South Korea) and in the southern coastal cities of Gwangyang, Yeosu, Suncheon, Jinju, and Ulsan (no NO_x data). When we compare the LOOCV performance of NO_x with the complete interpolation (*i.e.*, no stations omitted, see bottom panel of Fig. 4), we see R^2_{E2} scores change by > 0.4 at *e.g.* rural sites, the Busan shoreline, and the manufacturing district sites of Northern Yeosu and Eastern Gwangyang. These discrepancies indicate under–sampling of NO_x across rural South Korea and in some urban districts with locally contrasting emission activity.

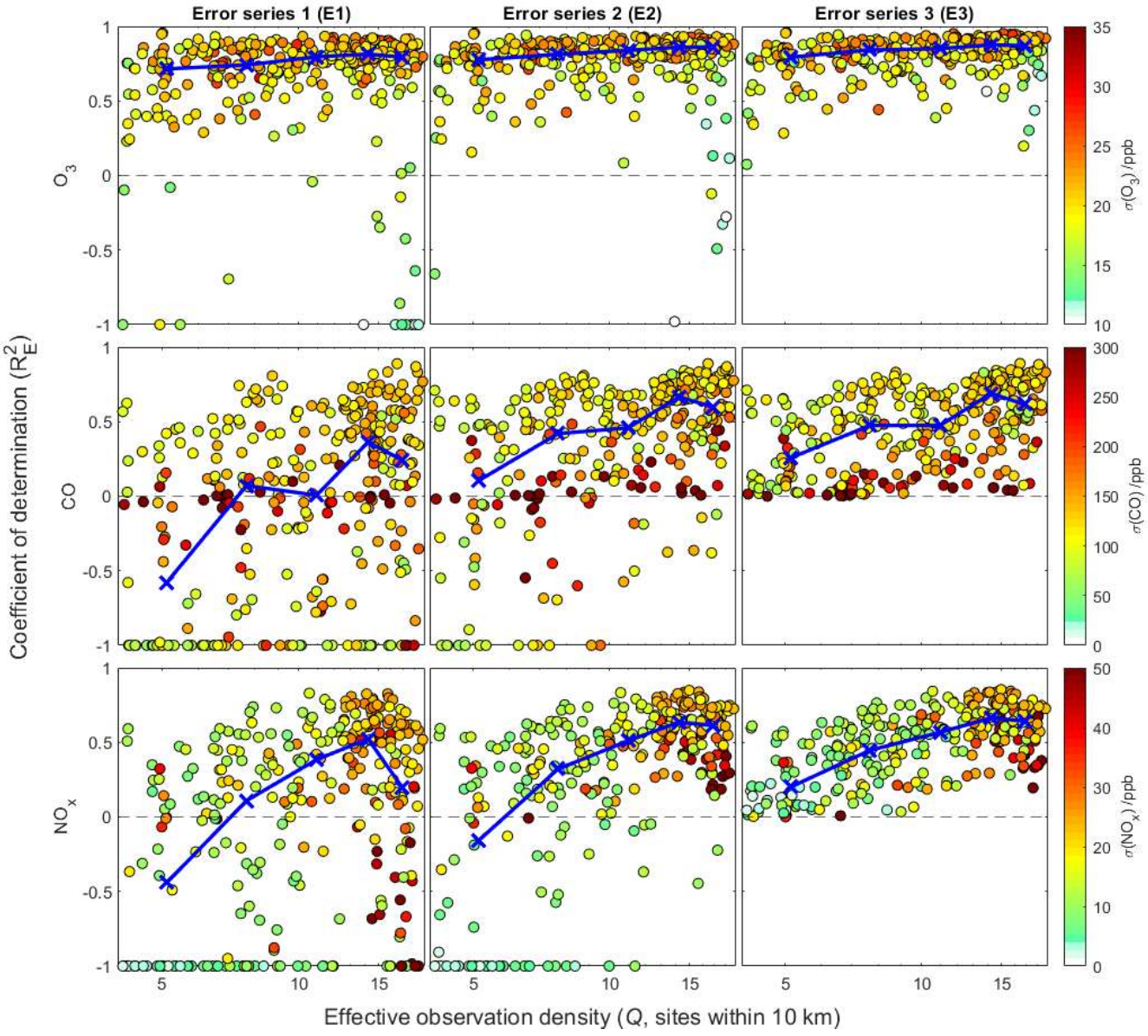

Figure 2.3: *Generalized coefficient of determinations (R^2_E, Eq. (5)) for NIER station predictions vs. the effective density of nearby observations (Q, effective number of sites in a 10 km radius).*

The three columns show the sequence R^2_{E1}, R^2_{E2}, and R^2_{E3}. The three rows are for the species O_3 (top), CO (middle), and NO_x (bottom). The calculations use the leave–one–out cross validation at each NIER station (circles) coloured by the standard deviation of observations. The blue conjoined crosses show the median R^2_E values for five percentile partitions of Q: 0–20%, 20–40%, 40–60%, 60–80%, and 80–100%.

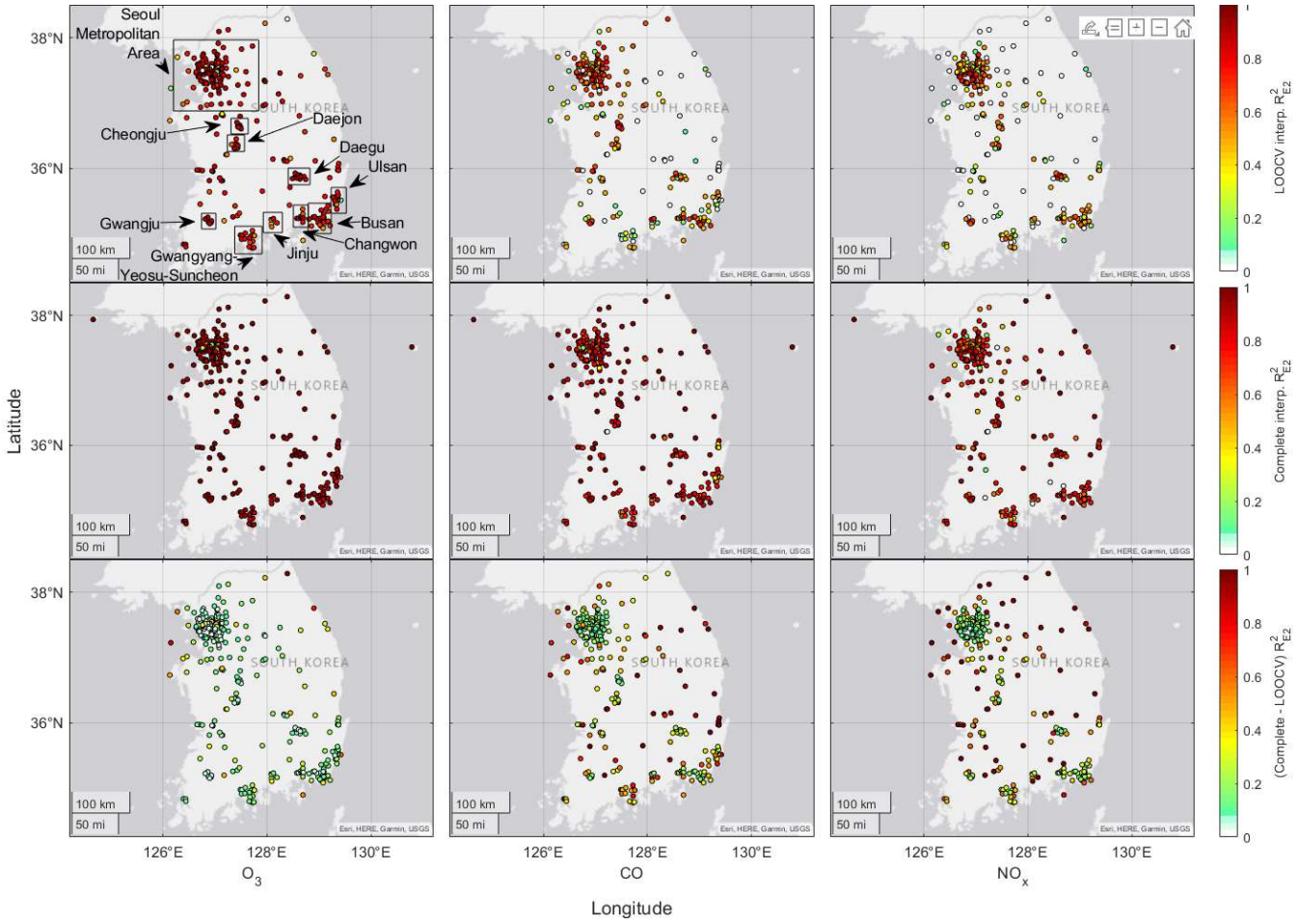

Figure 2.4: *The geographical distribution of NIER station prediction accuracies with the mean prediction bias removed from each station (R^2_{E2}, Eqs. (4) and (5)), shown for the three key species: O_3 (left), CO (middle), and NO_x (right).*

Top: R^2_{E2} scores for the LOOCV interpolations. Middle: R^2_{E2} scores for the complete interpolation, i.e. without omitting the data from predicted sites. Bottom: The difference between the complete– and LOOCV– interpolation R^2_{E2} scores. Negative R^2_{E2} values are truncated to zero. Approximate city bounds are shown via text and boxes in the top–left panel.

We have additionally compared the interpolation accuracy during the four meteorological phases presented by Peterson et al. (2019), *i.e.*, dynamic, anticyclone, low–level transport, and rex blocking, although we did not identify any obvious patterns across the phases (see Fig. C1 of Appendix C). An alternative test of meteorological influence is daytime (07:00 to 20:00 LT) *vs*. nighttime (21:00 to 06:00 LT) predictability, *i.e.*, prevailingly turbulent *vs*. stably stratified atmospheric surface conditions. Ozone and NO_x showed greater LOOCV predictability (R^2_{E2})

during daytime than nighttime by around +0.1 and +0.05 respectively, but not CO (see Fig. C2). More efficient turbulent mixing during daytime vs. nighttime likely smoothed some of the small–scale emission heterogeneity, resulting in more predictable fields.

3.3 Gridded air quality data

A major objective of this study was to obtain grid–cell averages (0.1°x0.1°, approx. 10 km x 10 km) for testing regional air quality models. Within each 0.1°x0.1° cell, we interpolate the key species to twenty–five points on a 0.02°x0.02° grid centred in the cell, and then average these values. The averages do not account for latitudinal differences in quadrangle areas, which are minor for South Korean latitudes. We apply the same treatment to the density of observations to produce the gridded Q values as seen in Fig. 1 (right–hand side).

3.4 Aircraft cell averages

We collect the measurements of O_3, CO, and NO_x from NASA DC–8 taken over land at radar altitudes below the PBL heights taken from the ERA5 data. The DC–8 measurements used here are 10 second merges corresponding to approximately 1 km flight segments $S \in \{1, 2, \ldots, 13942\}$. To compare the segments with the gridded site data, we average the contiguous segments through each grid cell to produce transect–averaged observations $Obs(T)$, where transects $T \in \{1, 2, \ldots, 2106\}$ contain around seven segments whose midpoints lie in the cell bounds. For the prediction set $Pre(T)$, we interpolate the traversed cells in time to match the mean aircraft time of flight during the respective transects. The number of transects through each cell is indicated by the gridded numbers in Fig. 1 (right–hand side).

4 Results

Table 2.1: *The generalized coefficients of determination R^2_{E1}, R^2_{E2}, and R^2_{E3} (Eq. (5)) for predictions vs. measurements at research stations (Olympic Park and Taehwa Forest) and along flight transects in the PBL.*

	Olympic Park			**Taehwa Forest**			**DC–8 (all transects)**			**DC–8 (Q > 10 transects)**		
Species	R^2_{E1}	R^2_{E2}	R^2_{E3}	R^2_{E1}	R^2_{E2}	R^2_{E3}	R^2_{E1}	R^2_{E2}	R^2_{E3}	R^2_{E1}	R^2_{E2}	R^2_{E3}
O_3	0.90	0.92	0.96	0.68	0.82	0.82	0.02	0.69	0.69	0.26	0.81	0.90
CO	0.73	0.75	0.76	–2.70	0.69	0.71	–2.20	0.28	0.41	–0.91	0.83	0.84
NO_x	0.67	0.68	0.68	–12.0	–3.60	0.00	–2.60	0.34	0.62	–0.84	0.51	0.73

Each flight transect is a median of contiguous 10 s observations through a grid cell (See Fig. 1 for sampling distribution and Fig. 5 for scatter plots), and the predictions are gridded values interpolated linearly in time to match the aircraft time of flight, then averaged. E1, E2, and E3 are time series of prediction errors defined in Eq. (4). NO_x measurements at Taehwa Forest are taken from Kim et al., 2022.

4.1 Research site prediction

Research stations provide case studies where the quality of measurements is carefully controlled, and so instrumental drift, noise, and biases are minimized. For each key species, we compare the NIER station data interpolated to the coordinates of the research stations, either at Olympic Park or Taehwa Forest, against the research station instruments (Fig. 5). Olympic Park and Taehwa Forest have effective sampling densities (Q) of 16 and 6 stations per 10 km respectively. Figure 5 shows accurate prediction of O_3 at both sites with predictably more scatter at Taehwa Forest where less information was available. We see a similar pattern for CO, but with a mean bias (predicted NIER interpolated value minus research instrument measurement) of +100 ppb at Taehwa Forest. NO_x is predicted reasonably well at Olympic Park except in the highest measured range (>100 ppb), but predictions appear random at Taehwa Forest. Table 1 indicates

excellent prediction accuracy at Olympic Park for all species (R^2_{E1}), and at Taehwa Forest for O_3. At Taehwa Forest, CO prediction improves when mean biases are removed (R^2_{E2}), but NO_x remains unpredictable. The linear regressions (R^2_{E3}) lead to very little improvement over mean bias correction (R^2_{E2}), implying that the temporal variability measured by the research stations was well captured. High R^2_{E1} scores suggest good co–calibration between the Olympic Park instruments and surrounding NIER instruments. We are unable to characterize the mean biases at Taehwa Forest.

As an isolated wilderness site, Taehwa Forest presents a unique problem for interpolating NO_x values based on NIER stations. The closest three NIER sites surround the forest station at a distance of around 10–15 km, and all are subject to NOx roadside emissions, thus our interpolation maps these high–NOx values into the relatively NOx–depleted forest.

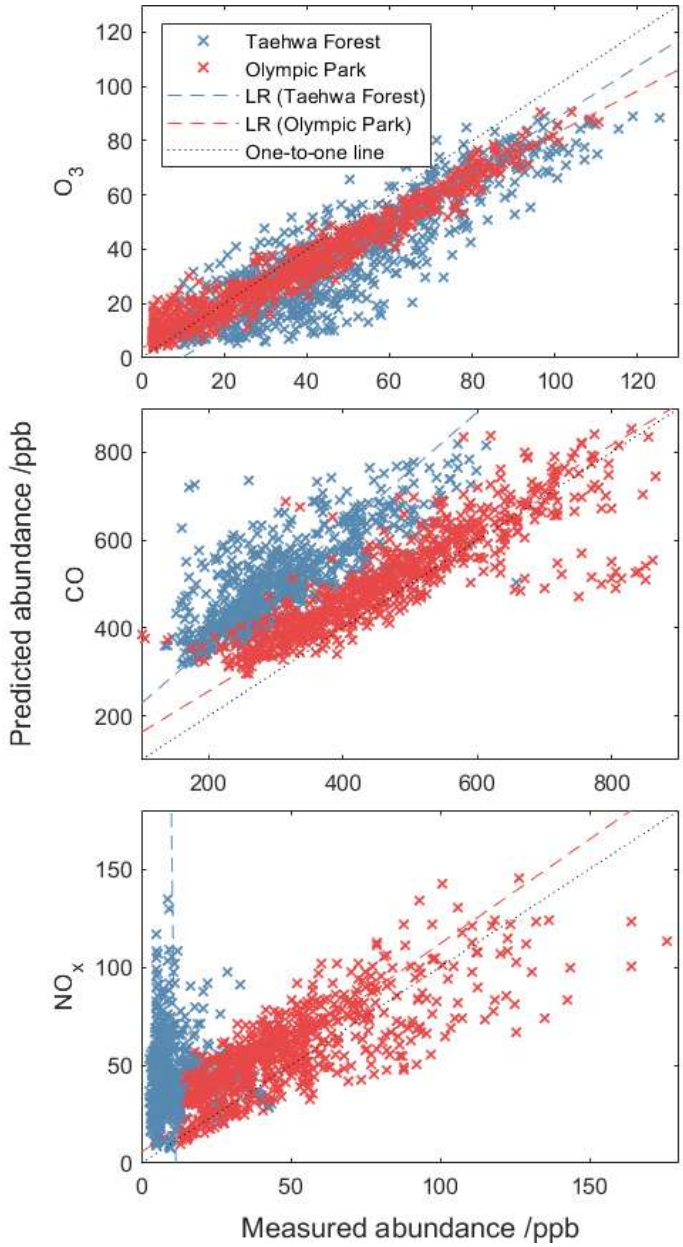

Figure 2.5: *Predicted vs. measured abundances of the three key species at Olympic Park (red) and Taehwa forest (blue) research stations.*

Predicted abundances are computed as point interpolations as per Equation (1). Dashed lines are linear regression (LR) models fitted by ordinary least squares.

4.2 DC–8 comparison

Figure 6 (top panel) shows that the gridded surface–site predictions of the DC–8 O_3 observations are consistently lower than observed but remain strongly correlated. CO predictions (Fig. 6, middle panel) show a consistent bias of around +100 ppb, but otherwise capture the variability of

the aircraft CO measurements reasonably well. NO_x predictions (Fig. 6, bottom panel) show a consistent positive bias along with randomness in the low measured range (<10 ppb). The gridded O_3 and CO predictions are highly accurate (R^2_{E2} = 80%) in grid cells with effective observation density (Q) exceeding ten, mainly sampled in the Seoul Metropolitan Area (Fig. 1, right–hand side). These findings show that with enough ground information, our gridded O_3 and CO datasets can predict upper PBL variability even in regions with intense small–scale emission heterogeneity. NO_x is exceptional, however, due to the rapid fall–off in abundance with altitude even within the PBL (Fig. A2 of Appendix A, see also Fig. 2 from Kim et al., 2021). We believe that O_3 titration in the Seoul Metropolitan Area leads to a slight underestimation in predicted variability as shown by a 10% increase in predictability using linear regression (R^2_{E3} = 90%, Table 1). We note however that the recurring flight patterns did not uniformly sample our grid domain and may have over– or under–sampled some regions. Obtaining vertically averaged concentrations rather than surface values remains a challenge given the substantial near–surface gradients inferred from Figs. 6 and A2, and suggests the need for vertically resolved chemical and dynamical modelling.

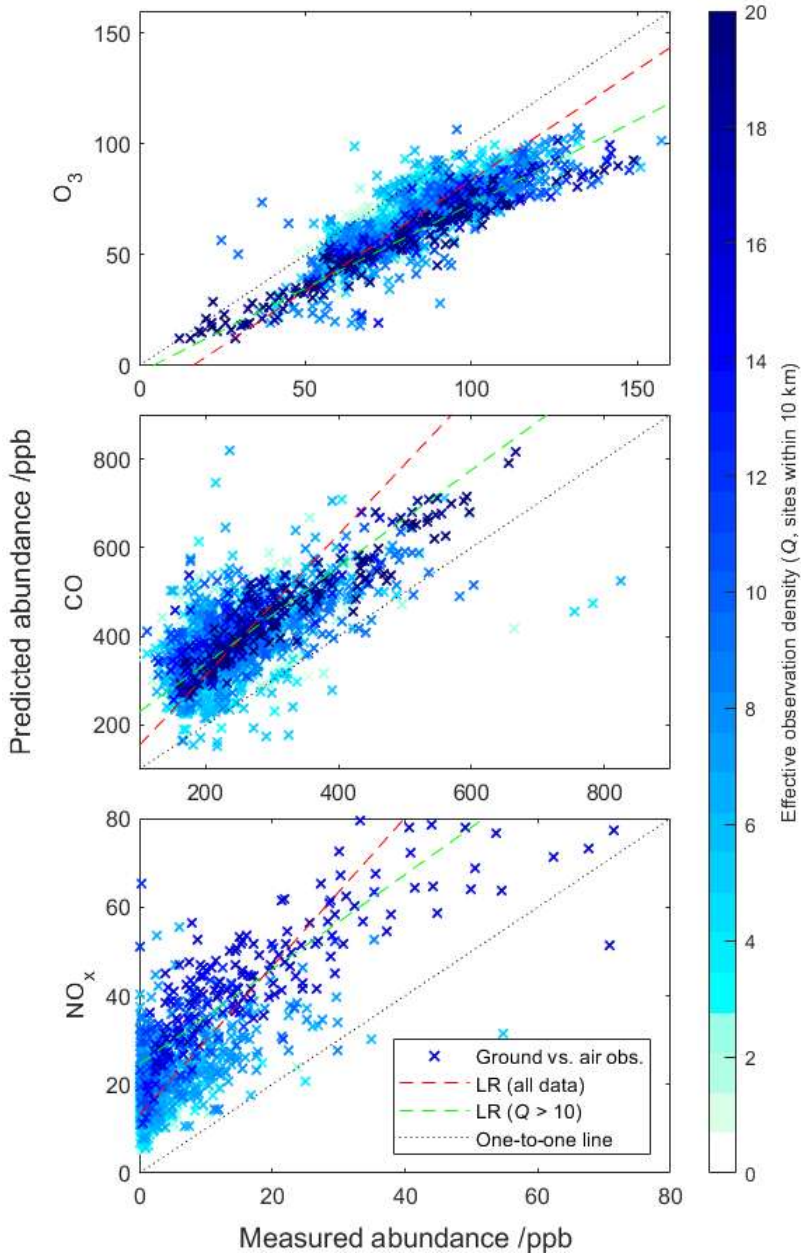

Figure 2.6: *Comparison of 10 s DC–8 observations in the PBL and gridded (0.1°x0.1°) hourly ground station data.*

Each data point represents the median of the contiguous aircraft transect through a grid cell (y–axis) and the median of the gridded ground station data interpolated linearly in time to match the aircraft time of flight (x–axis).

5 Conclusions

We create gridded (0.1°x0.1°) observational datasets from NIER ground station measurements of air quality over South Korea. Unlike the arithmetic mean gridding technique, this method

includes information from all nearby stations, including those outside the cell boundary, while mitigating sampling bias from site clustering. We identified significant mean absolute deviations between the IDW and arithmetic mean gridding techniques in *e.g.* the Seoul Metropolitan Area where IDW was most proved most accurate, prompting caution on the use of arithmetic mean gridding.

Our results suggest that the mean and variability of ground level O_3 was well captured over the whole of South Korea. For CO and NO_x, our LOOCV analysis revealed mean biases in certain NIER site predictions, but otherwise good prediction accuracy in most densely observed urban regions after the biases were subtracted. The well–predicted regions include the Seoul Metropolitan Area, Busan, Changwon, Daegu, and Cheongju, whereas prediction accuracy was poorer in the conjoined coastal cities of Gwangyang, Yeosu, and Suncheon, and in Ulsan; predictability in these regions would benefit from denser sampling. The aircraft comparisons confirm that the variability of O_3 and CO in the PBL are well captured from the surface stations; however, NO_x vertical gradients in the PBL confound attempts to predict the aircraft NO_x measurements.

Inverse Distance Weighting is susceptible to errors from over– or under–sampling of intense emission sources such as roadsides and industrial sectors. The characteristic concentrations of these regions may also be projected beyond the reach of the emission sources as seen in the high CO and NO_x biases at Taehwa Forest. These error sources are not unique to IDW. Nevertheless, improvements in NO_x predictability might be found with Land–Use regression and Machine Learning approaches as reviewed by Karroum *et al*. (2020), although these are outside the scope of the present paper. Such techniques can account for reactive NO_x decay away from sources, potentially mitigating errors from source–sampling bias and over–

projection. It would be interesting to compare the site predictabilities *vs*. sampling density for these alternate techniques, particularly in regions that were under–sampled according to LOOCV.

6 Appendices

Appendix A

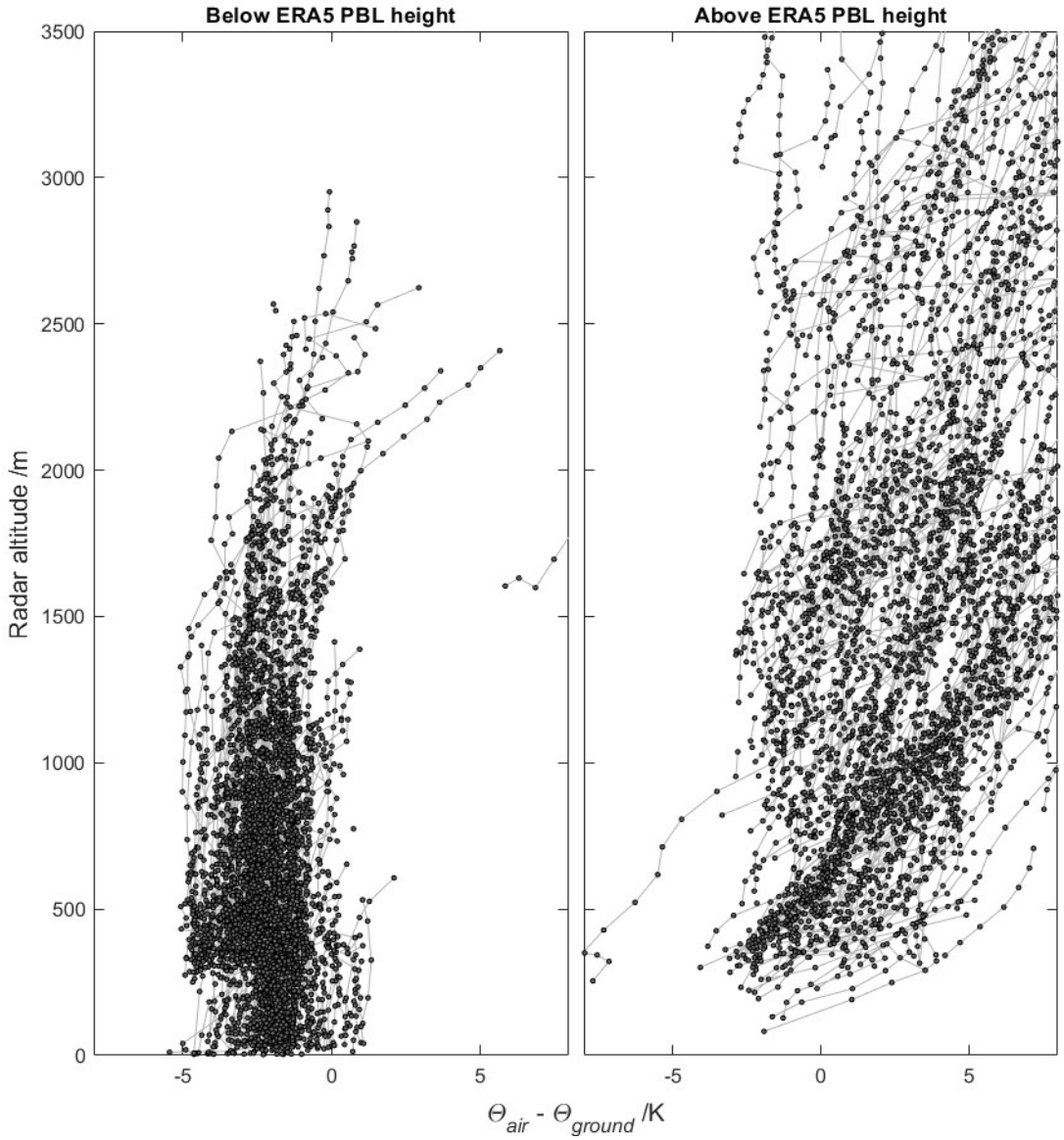

Figure 2.A1: *DC–8 10 s potential temperature (θ_{air}) measurements (dots) in a half degree radius of Taehwa Forest research station with gridded (0.25°x0.25°) surface potential temperature (θ_{ground}) subtracted, taken below (left) and above (right) the ERA5 designated PBL height.*

Lines connecting dots indicate contiguous transects, and all data was taken during ascent or descent (aircraft vertical speed > 1 m s^{-1}). θ_{ground} was calculated using the ERA5 2 metre temperature and surface pressure fields at native resolution (0.25°x0.25°, hourly), interpolated in time to match the aircraft time of flight.

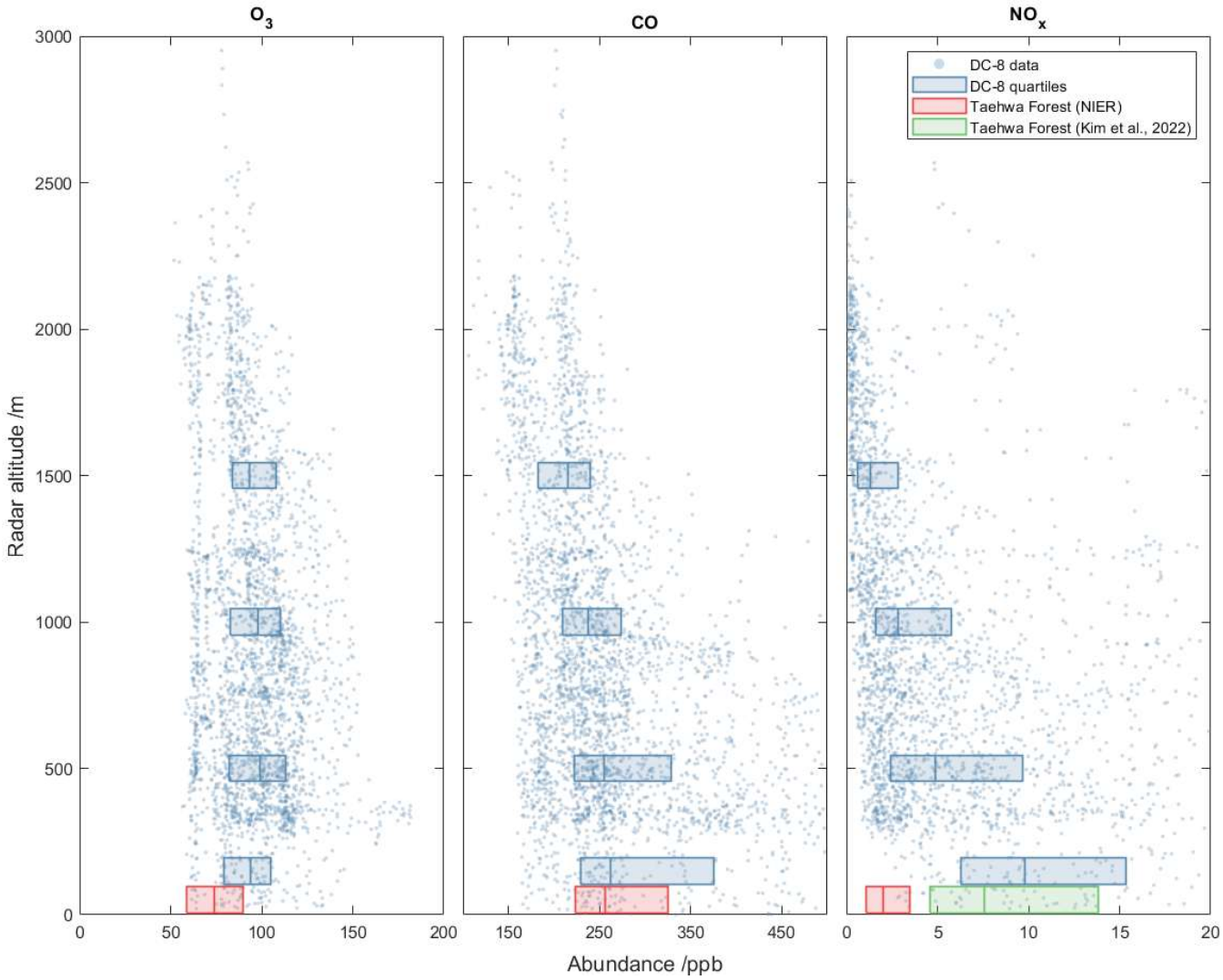

Figure 2.A2: *Vertical profiles of the DC–8 measured O_3 (left), CO (middle), and NO_x (right) in the ERA5 PBL within a half degree radius of Taehwa Forest research station.*

All data is sampled between the hours of 12:00 and 17:00 LT, and quartiles are shown for aircraft data (blue) partitioned into altitude bins (0–250, 250–750, 750–1250, and 1250–1750 m) and for the available ground research station measurements at Taehwa Forest (red) supplemented by Kim et al., 2022 (green).

Appendix B

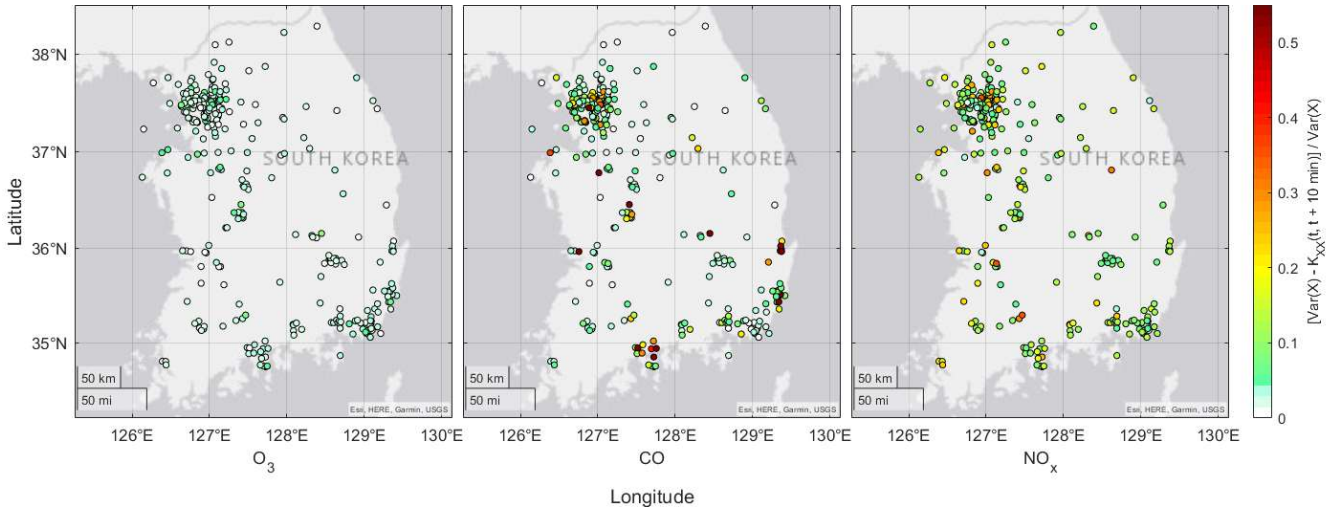

Figure 2.B1: *The sub–ten–minute temporal variability of the quality–controlled O_3 (left), CO (middle), and NO_x (right) site data at five–minute resolution.*

Sub–ten minute variability for individual sites was calculated as the site autocovariance subject to a ten–minute phase shift ($K_{XX}(t, t + 10\ min)$) subtracted from the total site variance (Var(X)), normalized by Var(X).

Appendix C

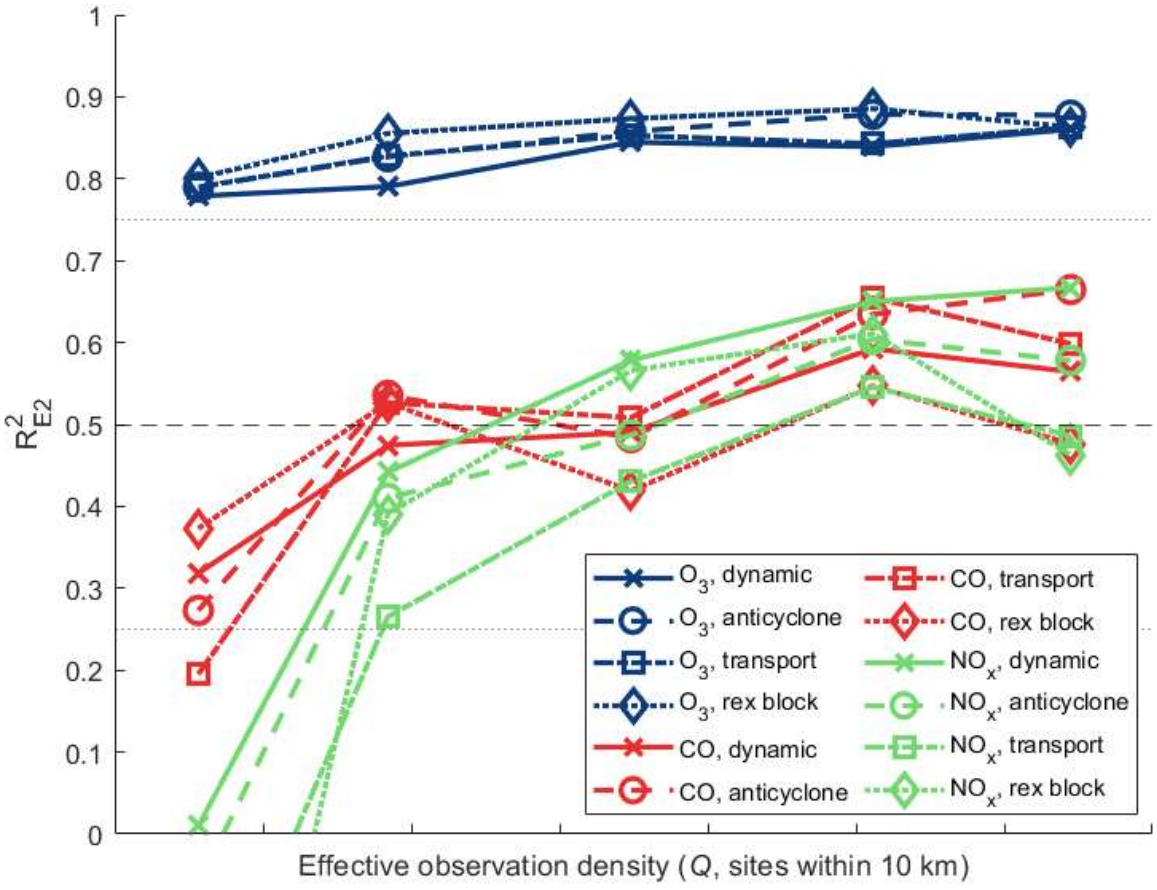

Figure 2.C1: *The median prediction accuracy (R^2_{E2}) of O_3 (blue), CO (red), and NO_x (green) within percentile bins (0–20%, 20–40%, 40–60%, 60–80%, and 80–100%) during the meteorological phases (dynamic, anticyclone, transport, and rex blocking) described by Peterson et al. (2021).*

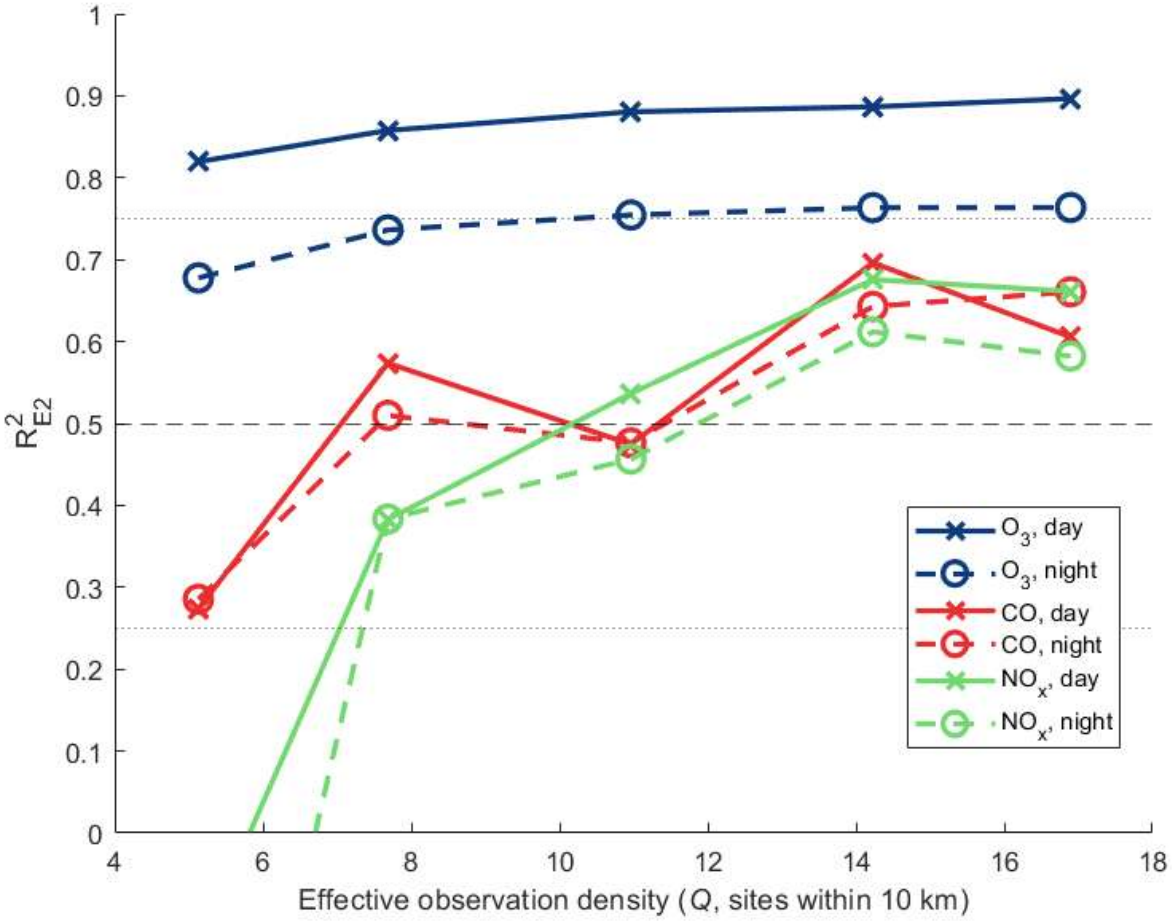

Figure 2.C2: *As in Fig. C1, but for daytime (07:00 to 20:00 LT incl.) and nighttime (21:00 to 06:00 LT incl.) data.*

Data Availability

Gridded data products and the datasets used in analysis are available from Wilson, 2024: https://doi.org/10.5061/dryad.sf7m0cgf5.

Author contribution

CW wrote the code to produce the datasets, codesigned and performed the analysis, drafted the manuscript, and responded to the reviews. MP designed the methodology, codesigned the analysis, reviewed and edited the manuscript.

Competing interests

The authors declare that they have no conflict of interest.

Acknowledgements

This study was funded by NASA (# 80NSSC21K1454) and the National Science Foundation (NSF, # AGS-2135749). We acknowledge NASA and NIER for providing the trace gas data used in this study and we are grateful to Kim Saewung for guidance on the KORUS–AQ data usage.

References

1. Brauer, M., Hoek, G., van Vliet, P., Meliefste, K., Fischer, P., Gehring, U., Heinrich, J., Cyrys, J., Bellander, T., Lewne, M., & Brunekreef, B.: Estimating Long–Term Average Particulate Air Pollution Concentrations: Application of Traffic Indicators and Geographic Information Systems. Epidemiology, 14 (2), 228–239, 10.1097/01.EDE.0000041910.49046.9B, 2003.
2. Crawford, J., Ahn, J., Al–Saadi, J., Chang, L., Emmons, L., Kim, J., Lee, G., Park, J., Park, R., Woo, J., Song, C., Hong, J., Hong, Y., Lefer, B., Lee, M., Lee, T., Kim, S., Min, K., Yum, S., Shin, H., Kim, Y., Choi, J., Park, J., Szykman, J., Long, R., Jordan, C., Simpson, I., Fried, A., Dibb, J., Cho, S., and Kim, Y.: The Korea–United States Air Quality (KORUS–AQ) field study. Elementa: Science of the Anthropocene, 9 (1): 00163. https://doi.org/10.1525/elementa.2020.00163, 2021.
3. Eck, T.F., Holben, B.N., Kim, J., Beyersdorf, A.J., Choi, M., Lee, S., Koo, J. H., Giles, D. M., Schafer, J. S., Sinyuk, Peterson, A. D. A., Reid, J. S., Arola, A., Slutsker, I., Smirnov, A., Sorokin, M., Kraft, J., Crawford, J. H., Anderson, B. E., Thornhill, K. L., Diskin, G., Kim, S. W., Park, S. J.: Influence of cloud, fog, and high relative humidity during pollution transport events in South Korea: Aerosol properties and PM2.5 variability, Atmos. Environ., 232, https://doi.org/10.1016/j.atmosenv.2020.117530, 2020.
4. Hochadel, M., Heinrich, J., Gehring, U., Morgenstern, V., Kuhlbusch, T., Link, E., Wichmann, H. E., Krämer, U.: Predicting long–term average concentrations of traffic–related air pollutants using GIS–based information, Atmos. Environ., 40, 542–553, https://doi.org/10.1016/j.atmosenv.2005.09.067, 2006.
5. Hersbach, H., Bell, B., Berrisford, P., Biavati, G., Horányi, A., Muñoz Sabater, J., Nicolas, J., Peubey, C., Radu, R., Rozum, I., Schepers, D., Simmons, A., Soci, C., Dee, D., Thépaut, J–N. (2023): ERA5 hourly data on single levels from 1940 to present. Copernicus Climate Change Service (C3S) Climate Data Store (CDS), https://doi.org/10.24381/cds.adbb2d47 (Accessed on 28–02–2024).
6. Jordan, C., Crawford, J. H., Beyersdorf, A. J., Eck, T. F., Halliday, H. S., Nault, B. A., Chang, L. S., Park, J. S., Park, R. J., Lee, G. W., Kim, H. J., Ahn, J. Y., Cho, S. J., Shin, H. J., Lee, J. H., Jung, J. S., Kim, D. S., Lee, M. H., Lee, T. H., Whitehill, A., Szykman, J., Schueneman, M. K., Campuzano–Jost, P., Jimenez, J. L., DiGangi, J. P., Diskin, G. S.,

Anderson, B. E., Moore, R. H., Ziemba, L. D., Fenn, M. A., Hair, J. W., Kuehn, R. E., Holz, R. E., Chen, G., Travis, K., Shook, M., Peterson, D. A., Lamb, K. D., Schwarz, J. P.: Investigation of factors controlling PM2.5 variability across the South Korean Peninsula during KORUS–AQ. Elementa: Science of the Anthropocene, 8, 28, https://doi.org/10.1525/elementa.424, 2020.

7. Karroum, K., Lin, Y.J., Chiang, Y.Y., Maissa, Y.B., El Haziti, M., Sokolov, A., Delbarre, H.: A Review of Air Quality Modeling. MAPAN, 35, 287–300, https://doi.org/10.1007/s12647-020-00371-8, 2020.
8. Kim, H., Park, R. J., Kim, S., Brune, W. H., Diskin, G. S., Fried, A., Hall, S. R., Weinheimer, A. J., Wennberg, P., Wisthaler, A., Blake, D. R., and Ullmann, K.: Observed versus simulated OH reactivity during KORUS–AQ campaign: Implications for emission inventory and chemical environment in East Asia. Elementa: Science of the Anthropocene, 10 (1), 00030, https://doi.org/10.1525/elementa.2022.00030, 2022.
9. Kim, S., Seco, R., Gu, D., Sanchez, D., Jeong, D., Guenther, A., Lee, Y., Mak, J., Su, L., Kim, D., Lee, Y., Ahn, J., Mcgee, T., Sullivan, J., Long, R., Brune, W., Thames, A., Wisthaler, A., Müller, M., Mikoviny, T., Weinheimer, A., Yang, M., Woo, J., Kim, S., Park, H.: The role of a suburban forest in controlling vertical trace gas and OH reactivity distributions – a case study for the Seoul metropolitan area, Faraday Discuss., 226, 537–550, https://doi.org/10.1039/D0FD00081G, 2021.
10. Lennartson, E., Wang J., Gu J., L. C. Garcia, Ge C., Gao M., Choi M., Saide Peralta, G. Carmichael, Kim J., and Janz S.: Diurnal variation of aerosol optical depth and PM2.5 in South Korea: a synthesis from AERONET, satellite (GOCI), KORUS–AQ observation, and the WRF–Chem model, Atmos. Chem. Phys., 18, 15125–15144, https://doi.org/10.5194/acp-18-15125-2018, 2018.
11. Matheron, G.: Principles of geostatistics, Econ. Geol., 58 (8), 1246–1266, https://doi.org/10.2113/gsecongeo.58.8.1246, 1963.
12. Murphy, A, H.: Skill scores based on the mean square error and their relationships to the correlation coefficient, Mon. Wea. Rev., 116, 2417–2424, https://doi.org/10.1175/1520-0493(1988)116<2417:SSBOTM>2.0.CO;2, 1988.
13. Oak, Y. J., Park, R. J., Schroeder, J. R., Crawford, J. H., Blake, D. R., Weinheimer, A. J., Woo, J., Kim, S., Yeo, H., Fried, A., Wisthaler, A., and Brune, W. H.: Evaluation of simulated O_3 production efficiency during the KORUS–AQ campaign: Implications for anthropogenic NOx emissions in Korea, Elementa: Science of the Anthropocene, 7, 56, https://doi.org/10.1525/elementa.394, 2019.
14. Park, R. J., Oak, Y. J., Emmons, L. K., Kim, C. H., Pfister, G. G., Carmichael, G. R., Saide, P. E., Cho, S., Kim, S., Woo, J., Crawford, J. H., Gaubert, B., Lee, H., Park, S., Jo, Y., Gao, M., Tang, B., Stanier, C. O., Shin, S., Park, H., Bae, C., and Kim, E: Multi–model intercomparisons of air quality simulations for the KORUS–AQ campaign. Elementa: Science of the Anthropocene, 9 (1), 00139, https://doi.org/10.1525/elementa.2021.00139, 2021.
15. Peterson, D. A., Hyer, E., Han, S., Crawford J., Park, R. J., Holz, R., Kuehn, R. E., Eloranta, E., Knote, C. J., Jordan, C. E., and Lefer, B.: Meteorology influencing springtime air quality, pollution transport, and visibility in Korea, air quality, pollution transport, and visibility in Korea. Elem Sci, 7, 57, https://doi.org/10.1525/elementa.395, 2019.

16. Sachse, G. W., Collins, J. E. Jr., Hill, G. F., Wade, L. O., Burney, L. G., and Ritter, J. A.: Airborne tunable diode laser sensor for high–precision concentration and flux measurements of carbon monoxide and methane. In Measurement of atmospheric gases 1433: 157–166. International Society for Optics and Photonics, https://doi.org/10.1117/12.46162, 1991.
17. Schnell, J. L., Holmes, C. D., Jangam, A., and Prather, M. J.: Skill in forecasting extreme ozone pollution episodes with a global atmospheric chemistry model, Atmos. Chem. Phys., 14, 7721–7739, https://doi.org/10.5194/acp-14-7721-2014, 2014.
18. Schroeder, J. R., Crawford, J. H., Ahn, J. Y., Chang, L. S., Fried, A. Walega, J. Weinheimer, A., Montzka, D. D., Hall, S. R., Ullmann, K., Wisthaler, A., Mikoviny, T., Chen, G., Blake, D. R., Blake, N. J., Hughes, S. C., Meinardi, S., Diskin, G., Digangi, J. P., Choi, Y. H., Pusede, S. E., Huey, G. L., Tanner, D. J., Kim, M., Wennberg, P.: Observation–based modeling of ozone chemistry in the Seoul metropolitan area during the Korea–United States Air Quality Study (KORUS–AQ). Elementa: Science of the Anthropocene, 8, 3, https://doi.org/10.1525/elementa.400, 2020.
19. Shepard, S.: A two-dimensional interpolation function for irregularly-spaced data, in: Proceedings of the 1968 23rd ACM national conference (ACM '68), Association for Computing Machinery, New York, NY, USA, 517–524, https://doi.org/10.1145/800186.810616, 1968
20. Susaya, J., Kim, K., Shon, Z., and Brown, R.: Demonstration of long–term increases in tropospheric O_3 levels: Causes and potential impacts, Chemosphere, 92, 1520–1528, https://doi.org/10.1016/j.chemosphere.2013.04.017, 2013.
21. Travis, K. R., Crawford, J. H., Chen, G., Jordan, C. E., Nault, B., Kim, H., Jimenez, J. L. Jost, C., Dibb, J., Woo, J. H., Kim, Y., Zhai, S., Wang, X., McDuffie, E., Luo, G., Yu, F., Kim, S., Simpson, I. J., Blake, D. R., Chang, L., Kim, M. J.: Limitations in representation of physical processes prevent successful simulation of PM2.5 during KORUS–AQ, Atmos. Chem. Phys., https://doi.org/10.5194/acp-22-7933-2022, 2022.
22. Weinheimer, A. J., Walega, J. G., Ridley, B. A., Gary, B. L., Blake, D. R., Blake, N. J., Rowland, F. S., Sachse, G. W., Anderson, B. E., and Collins, J. E.: Meridional distributions of NOx, NOy, and other species in the lower stratosphere and upper troposphere during AASE II., Geophys. Res. Lett., 21 (23), 2583–2586, https://doi.org/10.1029/94GL01897, 1994.
23. Wilson, C.: KORUS-AQ gridded O3, NOx, and CO observations created using ground station data, Dryad [data set], https://doi.org/10.5061/dryad.sf7m0cgf5, 2024.

Chapter 3: Life–Cycle Impacts of South Korean Air Pollution on Tropospheric Ozone and Methane: Sensitivity to Dispersion TimeLife–

Calum Patrick Wilson1, Michael John Prather1

[1]Department of Earth System Science, University of California, Irvine, Irvine CA, 92697, USA

Correspondence to: Calum P. Wilson (calumw@uci.edu)

Abstract

We calculate the global change in the production of tropospheric ozone (O_3) and loss of methane (CH_4) caused by 45 days of summertime South Korean anthropogenic emissions during the Korea-US Air Quality (KORUS-AQ) mission. Our modelling system consists of three stages: the boundary layer-residual layer (BL-RL) stage processes the emissions, photochemistry, deposition, aerosol reactivity, and transport over terrestrial South Korea at 0.1°x0.1° with hourly resolution. The plume (PL) stage continues to integrate the chemistry of air masses from the BL-RL stage as they are transported offshore, simulating offshore pollution plumes observed by aircraft. After three days of chemical aging in non-diluting plumes, the pollution remnants are dispersed (DP stage) into the background atmosphere and integrated until the pollution disappears. Net O_3 production is diagnosed in each stage using the integrated ozone change and our calculated perturbation lifetimes. In total, these 45 days of South Korean emissions create an excess CH_4 sink of 4.3 Gmol and a net O_3 source of 31.2 Gmol. A simplistic scaling of these values to annual global anthropogenic emissions suggests around 10% of CH_4 loss and 30% of net O_3 production is attributable to anthropogenic air pollution, but our Korean summertime case exaggerates these proportions. Reducing plume aging time to 2 days increases these terms by about 10%, and immediate dispersion (no plume aging) more than doubles them. Our model

supports the typical result that rapid dispersion of pollution, *e.g.* through coarse resolution, overestimates its impact on tropospheric O_3 and CH_4.

1 Introduction

The degree of future climate change depends on the trajectory of tropospheric ozone (O_3) and methane (CH_4), which are potent greenhouse gases (GHGs). The primary cause of increasing CH_4 abundance over the industrial era is through direct emissions from agriculture and fossil fuel use (see review by Saunois et al., 2025). Secondarily, through the emission of short-lived air pollutants like carbon monoxide (CO), we have altered the dominant atmospheric sink of CH_4, that is, reaction with the hydroxyl radical (OH, e.g., Isaksen and Hov, 1986). Ozone has no primary emissions; its abundance depends mostly on the balance between atmospheric photochemical production and loss. Anthropogenic emissions, especially nitrogen oxides (NO_x = $NO + NO_2$), volatile organic carbon compounds (VOCs), and CO, drive excess production and increasing abundances of O_3 (Lin *et al*., 1988). Tropospheric O_3 observations from remote sites, aircraft, ozonesondes, and satellites (Gaudel *et al*., 2018; Ziemke *et al*., 2019) suggest an increase in global tropospheric O_3 background levels from the 1990s to the 2010s with a pronounced positive trend over East Asia, where O_3 precursor emissions have intensified. Observed trends in the OH-CH_4 loss rate are ambiguous but most models suggest an increase from 1980 to 2014 of order 10% that is linked to rising NO_x emissions, especially in the lower latitudes (Stevenson *et al*., 2020) caused by rapid industrialisation in East Asia over the last few decades.

Previous chemistry-transport model studies of East Asian air pollution, such as Wild *et al*. (2004), found that "*ozone formation in the boundary layer and free troposphere outside the region of precursor emissions dominates total gross production from these sources in*

springtime, and that it makes a big contribution to the long range transport of ozone, which is greatest in this season." These studies, and subsequent global modelling studies of O_3 production from air pollution (e.g., Griffiths *et al*., 2021), have relied on the concept of odd-oxygen for separating production and loss terms, but this approach gives false lifetimes and incorrectly diagnoses production rates and their sensitivities, as recently demonstrated by Prather and Zhu (2024). These global models would have correctly calculated the perturbation to O_3 but would have incorrectly diagnosed the production and loss budgets. Here, we design a three-stage modelling system that explicitly calculates perturbation lifetimes of O_3 and can thus diagnose the net production of O_3, and loss of CH_4, that is directly caused by pollutants. The first *boundary layer-residual layer* (BL-RL) modelling stage tracks the initial chemistry and transport of pollution in the BL and overlying RL over South Korea. The second *isolated plume integration* (PL) stage follows air masses that escape from the terrestrial BL-RL domain as pollution plumes in the free troposphere (FT). The third *dispersed pollution* (DP) stage simulates the final chemical decay of pollution after dispersion of the plumes into the background atmosphere. The O_3 and CH_4 budget terms are extracted from the three modelling stages. We can separately calculate the O_3 budgets from pollution plumes as regularly seen by aircraft downwind of pollution sources (Bourgeois *et al*., 2020 and 2021; Cho *et al*., 2021; Guo *et al*., 2023; Hsu *et al*., 2004; Jacob *et al*., 2003), a noted problem in Wild et al. (2004).

The test case here uses an intensive set of air pollution data and analysis from the Korea-United States Air Quality (KORUS-AQ) mission, which focused on pollution in South Korea during May-June 2016. KORUS-AQ has generated an extensive body of research on what controls the boundary layer air pollution, particularly O_3, over South Korea (Crawford *et al*., 2021; Eck *et al*., 2020; Lee *et al*., 2022; Miyazaki et al., 2019; Park *et al*., 2021; Peterson et al.,

2019; Schroeder et al.; 2020). We use KORUS-AQ data with our new modelling approach to quantify the global impact of this pollution on GHG budgets. The data and tools needed for our modelling system are described in Sect. 2, then the overall model and its sequence of calculations, in Sect. 3. In Sect. 4, we sum the full life-cycle impacts of the Korean emissions on the global GHG budgets and report on the GHG perturbations to tropospheric O_3 and CH_4 caused by 5 weeks of early summer Korean pollution, with the conclusion in Sect. 5.

2 Modelling components and datasets

For the three modelling stages (BL-RL, PL, and DP; see Table 1), we put together (1) emissions data, (2) atmospheric composition observations for both background and polluted regions, (3) the photochemical mechanism and box model, and (4) meteorological data for South Korea over the KORUS period. These are described in the four respective subsections below.

Table 3.1: *Brief description of modelling stages.*

Modelling stage	**Description**
Boundary layer-residual layer (BL-RL)	Emissions, chemistry, horizontal transport, and 3-layer vertical exchange on a 60x60 (0.1°x0.1°) grid domain over South Korea with 1092 terrestrial cells. Air masses transported offshore are collected on 177 PL ghost cells surrounding the coast and combined over 4-hour intervals.
Isolated plume (PL)	Chemical evolution of isolated pollution plumes that depart from the BL-RL terrestrial domain via the PL ghost cells. After three days, all remaining pollution and by-products in the plume are dispersed into the free troposphere.
Dispersed pollution (DP)	Chemical evolution of the dispersed, post-plume pollution and their by-products remaining at the end of the PL stage. Both primary emittants and by-product species are integrated at low concentrations to ensure a linear chemistry regime and easy separation of impacts by species in the background troposphere. Pollutants are mixed across four levels (2, 4, 6, and 8 km) every 30 days over a 120-day integration with the impact of any remaining pollution estimated by extrapolation.

2.1 Emission inventories

Three inventories drive emissions of 35 species in our model: KORUS v5 (anthropogenic; Woo *et al*., 2020), GFED5 (biomass burning Chen *et al*., 2023), and MEGAN v2.10 (biogenic VOCs; Sindelarova *et al*., 2014; Guenther *et al*., 2012). These inventory choices are consistent with the multi-model KORUS-AQ study conducted by Park *et al.* (2021). The KORUS v5 emissions are provided on the same 0.1°x0.1° (latitude by longitude) grid of our boundary layer (BL) modelling stage with grid-cell edges at every tenth-degree. The GFED5 (0.25°x0.25°) and MEGAN v2.10 (0.5°x0.5°) grid-cell edges both coincide with KORUS v5 at degrees and half-degrees. Each of our 0.1°x0.1° model grid-cells is mapped onto the emissions grid and collects emissions in proportion to the area of each of the emission cells it spans. All emission cells are

fully covered by our BL stage cells except at the coastline, where the coarser MEGAN inventories are partially cut off. KORUS v5 and GFED5 emissions are fully included however.

2.1.1 KORUS v5 urban and industrial inventories

The KORUS v5 emissions include the explicit species: NO, NO_2, CO (see Fig. 1), ethene, formaldehyde, isoprene, acetaldehyde, methylglyoxal, benzaldehyde, acetone, methyl ethyl ketone (MEK), diacetyl, cresols, phenol, methacrolein (MACR), methyl vinyl ketone (MVK). The inventories also include SAPRC lumped species, which we represent with select surrogate species (see Carter, 2010 for SAPRC-07 documentation). We estimate molar emissions for individual species within SAPRC lumped emission categories using measured abundance ratios from NASA DC-8 airborne BL observations supplemented by emission ratio estimates in the Los Angeles basin (see de Gouw *et al*., 2017). Specifically, RCHO emissions go into propanaldehyde; ALK1, into ethane; ALK2, into propane; ALK3, into *n*-butane; ALK4, into (3/4) *n*-pentane + (1/4) *n*-hexane; ALK5, into *n*-heptane; ARO1, into (2/3) toluene + (1/3) benzene; ARO2, into (2/3) *m*-xylene + (1/3) 1-2-4-trimethylbenzene; OLE1, into propene; OLE2, into butadiene. The KORUS v5 emission inventories used in our BL-RL stage are monthly means, but the sources have variability over diurnal- and weekly- cycles, driving a nonlinear response to boundary-layer air chemistry. We therefore apply a unique temporal profile (*i.e.*, a diurnal and week-day activity scale factor; see Crippa *et al*., 2020) for each BL-RL grid cell based on the different sectoral emissions in each cell (see supplementary Fig. S1 and Table S1).

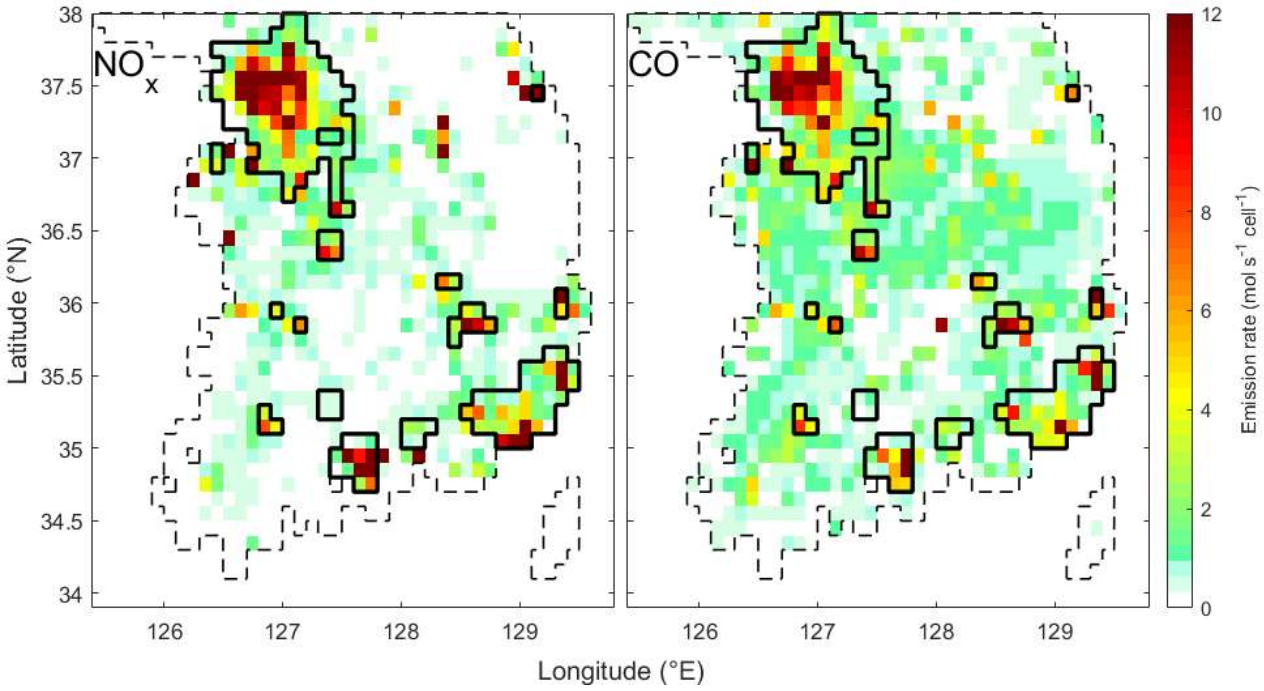

Figure 3.1: *The May 2016 NO_x and CO anthropogenic emission rates from the KORUS v5 inventory (Woo et al., 2020) shown as coloured cells (Same units apply to NO_x and CO).*

Bold lines enclose "urban" grid-cells in our model-observation comparison that were effectively monitored by five or more NIER ground stations within a ten-kilometre locus during the KORUS-AQ period (see Wilson and Prather, 2025 for ground station distribution). Dashed lines enclose the BL-RL terrestrial domain.

2.1.2 GFED5 biomass burning inventories

We used daily-resolved May and June 2016 biomass burning inventories from GFED5 (0.25°x0.25°, g m^{-2} day^{-1}; see Chen *et al*., 2023), assuming temporally uniform emissions. We include GFED5 emissions of NO, CO, ethane, propane, ethene, propene, isoprene, MEK, benzene, toluene, xylenes (as *m*-xylene), methanol, ethanol, formaldehyde, acetaldehyde, propanaldehyde, methyl glyoxal, formic acid, and glycoaldehyde. We consider the GFED5 inventories as part of the anthropogenic perturbation alongside KORUS v5, assuming the emissions are predominantly from agricultural waste burning.

2.1.3 MEGAN v2.10 biogenic inventories

We use monthly mean MEGAN v2.10 biogenic emission inventories with constant temporal profiles generated for May and June 2010 (0.5°x0.5°, kg m^{-2} s^{-1}; see Guenther *et al*., 2012). We use the following inventories: CO, ethane, propane, ethene, propene, isoprene, toluene, ethanol, formaldehyde, acetaldehyde, acetone, and acetic acid. As in the GFED5 inventories, offshore emissions are assumed to be negligible and excluded from the BL-RL stage.

2.2 In situ observations

Observations are used to define the clean-air background chemical composition in our modelling system. The BL-RL stage (Sect. 3.1) uses airborne KORUS-AQ measurements (KORUS-AQ Science Team, 2019) to prescribe a single background composition as a boundary condition for free tropospheric air entrained into the terrestrial BL and RL. Note that our use of a single average KORUS-AQ background composition does not resolve variations in transboundary O_3 and CO pollution entering the Korean peninsula as observed by Miyazaki *et al*. (2019). In the final stage of our modelling sequence (DP stage), we disperse plumes into a vertically-binned remote background environment obtained from the Atmospheric Tomography Mission (ATom) (Sect. 3.3). Our primary model-observation metrics compare the BL concentrations in our 0.1°x0.1° grid cells with a grid-cell averaged values of O_3, CO, and NO_x as observed at the surface NIER sites. See Wilson and Prather (2025) for the methodology of deriving grid-cell averaged data from a set of sites.

2.2.1 KORUS-AQ airborne observations

NASA DC-8 sampled the air above South Korea and the Yellow Sea during 20 days between May 01 and June 11, 2016. Flight paths were coordinated to follow Seoul pollution and other plumes (*e.g.,* from the Daesan industrial complex), and thus distributions of pollutants are

positively skewed as a result. All species mole fractions show a clear peak probability at low percentiles, which we use to define "background" air. We calculate the modal concentrations using the Half-Sample Mode of all South Korean flight data and use them to define the BL-RL background composition. These values are not sensitive to the inclusion or exclusion of data sampled within the ERA5-defined boundary layer (Hersbach *et al.,* 2023).

We also use KORUS-AQ observations of photolysis frequencies (J-values) and aerosol surface area densities in our chemistry modelling and describe these data and their usage in Sects. 2.3.2 and 2.3.3.

2.2.2 ATom airborne observations

The ATom missions deployed the DC-8 to sample the air over the remote ocean basins and profile the reactivity in the troposphere (Thompson *et al*., 2022). We define the DP background compositions using 10 s merged ATom-4 data (27 April, 29 April, and 21 May 2018) from the modelling data stream (Prather *et al*., 2023) sampled to represent summer Pacific conditions. We take the medians of data partitioned into 2-km-wide altitude bins, centred on 2 km, 4 km, 6 km, and 8 km, using only data flagged as primary and secondary observations; the medians were used to spin-up the DP background air over 365 days (constant summer conditions) in the respective altitude bins (see Table 2 for spun-up concentrations).

Table 3.2: *Background air compositions used in the modelling system.*

	KORUS-AQ	**ATom steady-state**			
Species	**FT**	**2 km**	**4 km**	**6 km**	**8 km**
Column fraction	N/A	35%	27%	21%	17%
Temperature	From ERA5	284	273	260	250
Pressure (hPa)	From ERA5	797	625	484	373
RH (%)	From ERA5	72	46	41	20
CH_4 (ppb)	1930	1910	1890	1880	1870
CO (ppb)	112	115	105	98.5	95.8
O_3 (ppb)	71.5	48.3	56.3	62.6	62.9
NO_x (ppt)	76.3	36.3	31.2	32.1	40.3
PAN (ppt)	249	16.4	48.8	195	236.0
HNO_3 (ppt)	24.9	224	119	79.3	56.6
H_2O_2 (ppt)	233	590	629	417	247
HCHO (ppt)	229	364	218	128	79.6
ethane (ppt)	1550	1320	1200	1070	932
propane (ppt)	155	71.5	57.6	41.8	65.8
n-butane (ppt)	20.0	6.0	4.7	5.0	7.0
Acetone (ppt)	585	448	455	440	498
Acetaldehyde (ppt)	407	15.9	11.5	7.9	6.0
Benzene (ppt)	16.8	22.5	13.5	12.2	15.5
Toluene (ppt)	0.0	0.3	0.2	0.3	0.4

The KORUS-AQ FT (free troposphere) composition provides background air to the BL-RL stage and is derived from the Half-Sample Mode of South Korean DC-8 flights. The ATom data are steady-state background compositions used in our DP stage (Sect. 3.3). ATom flight data were sampled on 27 and 29 April, and 21 May 2018 between 30-50°N and 200-235°E, the median 10 s values over 2-km-wide altitude bins centred on 2 km, 4 km, 6 km, and 8 km are used here. Some very low-abundance VOCs (e.g., C_2H_4, isoprene, n-C5-7 alkanes) are initialised in the BL-RL stage but not tabulated here.

2.2.3 NIER surface pollution maps

Surface observations of O_3, CO, and NO_x were recorded by South Korea's National Institute of Environmental Research (NIER) network of 300+ ground stations from 2016/05/02 to 2016/06/11. These measurements have been spatially interpolated via inverse distance weighting (discussed in Wilson and Prather, 2025) and gridded to match our BL-RL stage resolution (available at Wilson, 2025).

2.3 Photochemical box model

In all stages of our modelling system we integrate the photochemical evolution of air masses containing South Korean air pollution. For this, we implement the Framework for 0-D Atmospheric Modelling (F0AM v3.1; Wolfe *et al*., 2016) using explicit chemical mechanisms described in Sect. 2.3.1. F0AM is initialised with the mole-fractions of all the chemical species, with constant meteorological parameters (temperature, pressure, and relative humidity), and with *J*-values that we derive from KORUS-AQ observations. Meteorological parameters (pressure and temperature) are used to compute the rate coefficients. During the BL-RL stage, the F0AM chemistry and meteorology is reinitialised hourly in the BL and RL of each grid cell before emissions and transport. During the PL and DP stages, the F0AM model is run over longer periods in a diel cycling mode, updating the *J*-values every half-hour based on the computed solar zenith angle at a standard point near Seoul (37.5°N, 127°E).

2.3.1 Chemical mechanism

From our set of 35 emitted species, we generate a chemical system of 1610 chemical species and 5000 reactions using the Master Chemical Mechanism (MCM v3.3.1; Bloss *et al*., 2005; Jenkin *et al*., 1997; Jenkin *et al*., 2003; Jenkin *et al*., 2015; Saunders *et al*., 2003). Most of these species are secondary VOCs branching from the decomposition pathways of the primary species.

We found that incomplete reaction mechanisms led to some spurious results in our dispersed pollution modelling. Notably, residual benzene pollution catalysed ozone depletion through secondary products (*2*-hydroxyphenoxy radical, *2*-phenol peroxide, and phenol hydroperoxide) that had an extremely slow termination path. We solved this problem by introducing a first-order loss with a lifetime of 5 days for organic hydroperoxides and hydroxylated species based on the wet deposition timescale for gases with large Henry's Law constants (Bi and Isaacman-VanWertz, 2022). This loss was also included for HNO_3 to avoid unrealistic accumulation in the DP stage.

2.3.2 Photolysis frequencies

We use KORUS-AQ observations of J-values under all-sky conditions to model photolysis in our chemical box model (see Hall *et al*., 2018 for instrumental details). We computed the mean J-values centred in 5° solar zenith angle (SZA) bins (15° to 60° bin edges), sampling observations below 1.5 km for the BL-RL stage, and above 1.5 km for the PL and DP stages. To simulate the diurnal cycle of J-values, F0AM uses the MCM parameterisation: $J = J_{MCM} cos(SZA)^m exp(n/cos(SZA))$, where J_{MCM}, m and n are reaction-specific fitting parameters originally obtained from clear sky radiation modelling (Jenkin et al., 1997; Saunders et al., 2003). Here, we use our SZA-binned KORUS-AQ observations to derive more realistic all-sky *J*-values: $J_{KORUS} = k\, J_{MCM}$, providing F0AM with the correction factors k. We did not attempt to correct the J_{MCM} values that were not observed by DC-8 as these tend to be far less important, low abundance species. See Table 3 for the list of J_{KORUS} and J_{MCM} scale factors, and Fig. 2 for a sample of observed vs. fitted (J_{KORUS}) *J*-values as a function of SZA.

MCM v3.3.1 lacks a photolysis mechanism for peroxyacetyl nitrate (PAN), which is important for PAN loss only in the DP stage in the upper troposphere. We added J-PAN as being

proportional to J-O_3→O(^{1}D) with scale factor 0.014 based on the KORUS J-values and empirical PAN photolysis frequencies (Talukdar *et al*., 1995).

Table 3.3: *The photolysis reactions recalibrated in our modelling system.*

MCM ID	Reaction	J_{MCM} (s^{-1})	J_{KORUS} <1.5 km (s^{-1})	J_{KORUS} >1.5 km (s^{-1})
J1	J-O_3→O(^{1}D)	6.07E-05	5.66E-05	8.35E-05
J3	J-H_2O_2	1.04E-05	1.01E-05	1.46E-05
J4	J-NO_2	1.17E-02	1.21E-02	1.66E-02
J5	J-NO_3→O_2	2.49E-02	2.48E-02	2.86E-02
J6	J-NO_3→O	1.75E-01	2.11E-01	2.43E-01
J7	J-HONO	2.64E-03	2.00E-03	2.84E-03
J8	J-HNO_3	9.31E-07	8.66E-07	1.24E-06
J11	J-HCHO→HCO	4.64E-05	4.83E-05	7.57E-05
J12	J-HCHO→CO	6.85E-05	7.06E-05	1.11E-04
J13	J-CH_3CHO	7.34E-06	8.18E-06	1.79E-05
J14	J-C_2H_5CHO	2.88E-05	2.62E-05	5.09E-05
J21	J-CH_3COCH_3	7.99E-07	5.36E-07	8.94E-07
J22	J-MEK	5.80E-06	7.42E-06	1.48E-05
J31	J-CHOCHO→2CO	6.85E-05	1.74E-05	2.72E-05
J32	J-CHOCHO→HCHO	1.03E-05	3.18E-05	4.89E-05
J33	J-CHOCHO→2HCO	3.80E-05	1.11E-04	1.55E-04
J34	J-CH_3COCHO	1.54E-04	1.60E-04	2.43E-04
J35	J-$CH_3COCOCH_3$	3.33E-04	3.63E-04	4.71E-04
J41	J-CH_3OOH	7.65E-06	7.32E-06	1.11E-05
J51	J-CH_3ONO_2	1.59E-06	1.24E-06	1.71E-06
J52	J-$CH_3CH_2ONO_2$	1.91E-06	2.11E-06	2.85E-06

J_{MCM} values are the clear-sky J-value coefficients used in MCM (Saunders et al, 2003). J_{KORUS} are the all-sky coefficients used in our modelling system, fitted using KORUS-AQ J-value observations. MCM also includes photolysis reactions of n- and i-propylnitrate, t-butylnitrate, 2-oxopropyl nitrate, n-butyraldehyde, i-butyraldehyde, (Z)-4-hydroperoxy-2-methyl-2-butenal, MACR, and MVK, which were not reported in KORUS-AQ data.

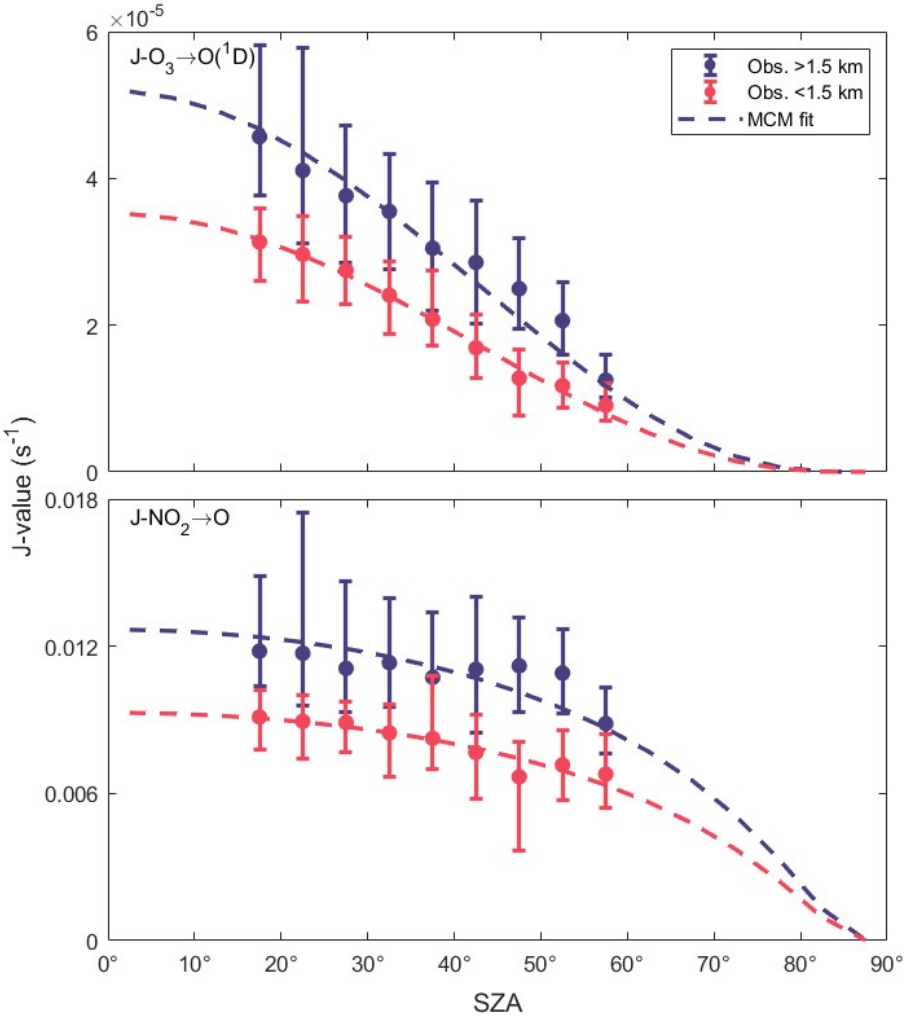

Figure 3.2: *Observed and fitted all-sky J-O_3—>$O(^1D)$ and J-NO_2 photolysis frequencies.*

Dots show the mean J-values in 5° SZA bins and whiskers show the root mean square deviations of the upper- and lower- residuals. Dotted lines show the MCM-parameterised J-values scaled to $\boldsymbol{J_{KORUS}}$ *values. Data were sampled above (blue) and below (orange) 1.5 km altitude.*

2.3.3 Aerosol reactivity

Hydrolysis of N_2O_5, NO_2, and NO_3 on aerosol surfaces is an important sink for NO_x in a polluted environment, effectively converting NO_x to HNO_3, which is irreversible in the BL-RL and PL stages. Aerosol-HO_2 reactions also reduce HO_x (OH + HO_2) and subsequently ROOH radicals. The first-order rate coefficient for aerosol reactivity with molecule X is given by $(1/4)\rho_A v_X \gamma_X$ (Yan *et al*., 2019), where ρ_A is aerosol surface area density, v_X is the mean thermal velocity of X, and γ_X is the surface reaction probability. We use Lamarque *et al*. (2012) aerosol reactivities

($\gamma_{N2O5} = 0.1$; $\gamma_{NO2} = 0.0001$; $\gamma_{NO3} = 0.001$; $\gamma_{HO2} = 0.2$), which are taken to be independent of aerosol composition. Aerosol surface area densities were inferred from KORUS-AQ Laser Aerosol Spectroscopy (LAS) in situ 10 s measurements of size-resolved particle number density (Nault *et al*., 2018). We average the surface area densities over the entire KORUS-AQ period for altitude ranges of 0.0-1.5 km (BL-RL stage), 2±1 km (PL and DP stages), 4±1 km, 6±1 km, and 8±1 km (DP stage). Thermal velocities for the four species were computed using the mean ERA5 meteorology for the BL-RL stage and ATom mean temperature profiles for PL and DP stages (see Table 2). Final aerosol reactivity values used in the different modelling stages are shown in Fig. 3.

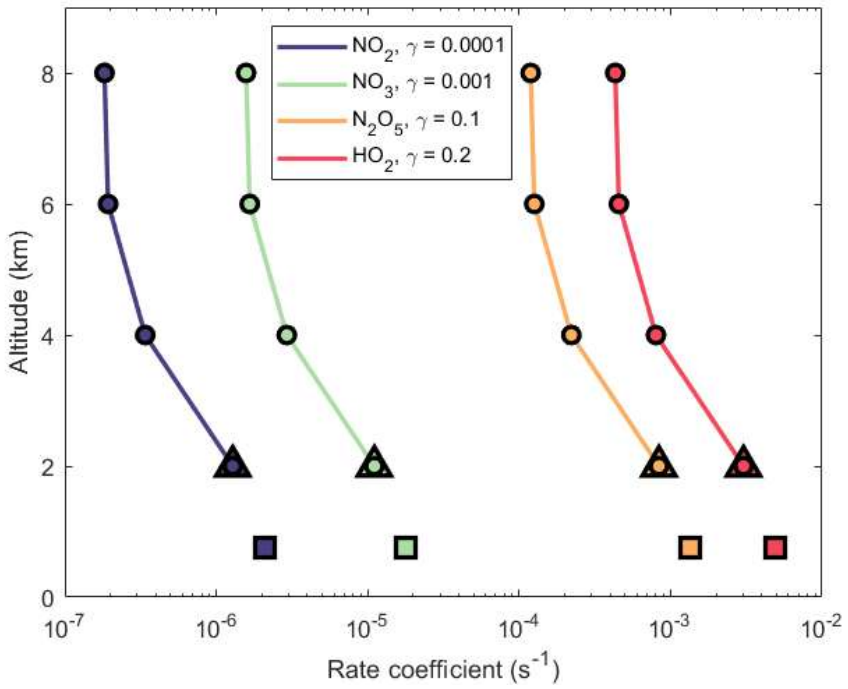

Figure 3.3: *Aerosol reactivity rate coefficients used in our model stages.*

These first-order loss coefficients for NO2, NO3, N2O5, and HO2 are computed from mean aerosol surface area concentrations and temperatures profiled by DC-8 during the KORUS-AQ mission and used for the BL-RL (squares; 0.0-1.5 km altitude), PL (triangles; 2±1 km), and DP (circles; 2±1, 4±1, 6±1, and 8±1 km) stages (see Table 2). Aerosol surface areas are from KORUS-AQ LAS data (Nault et al., 2018).

2.3.4 Surface deposition

Surface deposition is a sink of O_3 and NO_2 in our hourly BL chemical integrations. The BL-RL stage uses a simple dry deposition velocity (v_d, cm s^{-1}) for O_3 and NO_2 in each grid cell based on a fixed land surface classification over the KORUS period. The deposition first-order loss rate (s^{-1}) in the BL is calculated hourly as v_d divided by BL height (cm). To map the land cover over the BL-RL grid domain, we use 32 land cover classifiers as defined by the Land Cover Classification System (LCCS, 2017). From the LCCS 1/360°x1/360° pixels, we calculate the fractional coverage of each classifier in our 0.1°x0.1° model cells. We group the 32 classifiers into 8 super-classifications used by Jia *et al.* (2016) (see Table 4 for our super-classifications and their constituent LCCS classifiers). We combine our classification fractional areas to calculate average v_d values for O_3 and NO_2 as shown in Fig. 4.

Table 3.4: *Average dry deposition velocities (v_d) for land surface categories.*

Super-classifications	**LCCS classifiers**	**NO_2 v_d (cm s^{-1})**	**O_3 v_d (cm s^{-1})**
Cropland	*cropland (5)*	0.07	0.43
Grassland	*grassland*	0.11	0.27
Evergreen	*evergreen (4)*	0.28	0.47
Mixed forest	*tree_mixed*	0.13	0.51
Deciduous	*deciduous (6)*	0.13	0.4
Tree-shrub	*shrubland (3)* *mosaic (3)*	0.2	0.34
Urban	*urban* *lichens_and_moss* *bare_areas (3)* *sparse (4)*	0.03	0.03
Water	*water (3)* *flooded* *ice*	0.01	0.03

Values shown are based on data from field campaigns covering different terrain classifications (Zhang et al., 2009; Adon et al., 2013; Zhang et al., 2002; Simpson et al., 2001; Brook et al., 1999). Data represent diel averages over the campaign periods. For super classifications with the LCCS classifiers, see text.

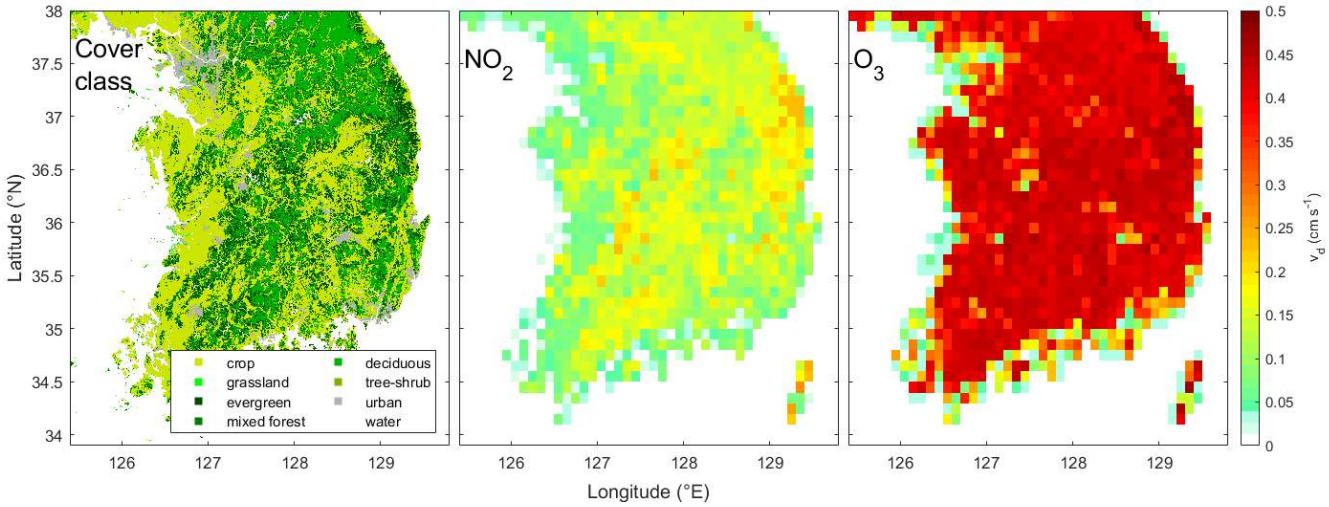

Figure 3.4: *Land cover classes and dry deposition maps.*

Land cover classes show our super classifications based on the LCCS classifiers plotted at the native 1/360°x1/360° resolution (left). Dry deposition (v_d) rates for NO_2 (middle) and O_3 (right) at model resolution (0.1°x0.1°) are derived from the area-weighted super-classifications and average deposition velocities in Table 4.

2.4 ERA5 meteorology

Our BL-RL stage uses hourly, 0.25°x0.25° ERA5 Reanalysis 2D fields for boundary layer height and surface pressure (Hersbach *et al.,* 2023) plus 3D fields for temperature, specific humidity, u, and v wind (Hersbach *et al*., 2017). The ERA5 data are point-values defined at grid centres (*e.g.* 37.50°N, 127.00°E at Seoul) and at hybrid (η) vertical level centers. ERA5 pressure is indexed on vertical level edges. Our BL and RL columns are discretized and vertically aligned with these edge-level coordinates at the start and end of every hourly timestep in the model, and the 3D fields are averaged separately in the BL and RL columns to produce 2D mean column values for winds, temperature, and humidity. We only use the lower atmospheric ERA5 data, from k = 99 (~4.5 km altitude) to k = 137 (surface; see supplemental Table S2).

The BL always consists of at least one ERA5 layer above the surface, and the RL – if it exists – consists of at least one layer atop the BL column. The BL and RL columns each have a single chemical mixture with a mean pressure and temperature averaged over their constituent

ERA5 layers. To obtain these fields at model resolution (0.1°x0.1°), we interpolate the grid-centred ERA5 data to our model grid-cell centres via bicubic convolution and assume these data points represent the area mean. The ERA5 nocturnal BL height falls to a mean minimum height of 175 m over the Korean peninsula, and locally as low as 24 m, leading to unrealistically concentrated emissions. We mitigate this problem by prescribing a minimum BL height of 200 m in our model.

2.4.1 Vertical discretisation (BL and RL)

Our BL-RL stage uses mass-weighted (δp) column averages for temperature, specific humidity, and horizontal wind fields. To average these variables for the BL and RL, we align the BL and RL edges in our model to nearest ERA5 vertical edge levels in each gridded interpolated ERA5 atmospheric column over the terrestrial domain. Each model time step starts and finishes with a discretised BL+RL column, where the BL consists of an integral number of ERA5 levels based on mass, and the RL, if it exists at the time, consists of an integral number of ERA5 levels atop the BL. When the ERA5 BL height (m) changes with time, we adjust the top of the BL to the closest ERA5 edge level (in metres). If the BL column expands to envelop higher levels, it collects all the pollution in the entrained RL levels; if it envelops levels above the RL, it collects FT air. If the BL contracts, it leaves behind discrete layers of residual pollution that are mixed with the RL column. This step represents the effective vertical transport in the model.

When the ERA5 surface pressure field changes each hour, the ERA5 edge-level pressures shift, resulting in misaligned initial and final pressure levels. This effect is hardly noticed because the horizontal transport of BL and RL levels separately results in BL and RL mass that do not align with the new edge levels. Every hourly timestep, after horizontal and vertical transport, we realign the BL-RL and RL-FT (or BL-FT) interfaces with the standard ERA5 levels

(*rediscretisation*) and remap the air mass from the intermediate BL+RL+FT columns to the new partition (*remapping*). The BL and RL masses adjust during horizontal transport. If the new BL mass (determined by the new BL height and ERA5 level edges) exceeds the transported BL+RL burdens, then the RL is fully entrained and some FT air is remapped to the BL. If the transported BL+RL mass exceeds the new BL mass, then some air is remapped into the RL. If any RL mass remains after vertical transport, the RL-FT interface is rediscretised by adding the ERA5 levels upward from the new BL-RL interface to the first level that fully encapsulates the RL mass. Some background FT air is remapped to the RL during this process. While we keep track of the BL and RL air mass during horizontal transport and vertical remapping, the critical elements being transported are the moles of primary and secondary pollutants. When we add FT air to the BL or RL, we likewise keep track of the pollutants from this relatively clean air. During this process, no pollutants are mixed into the FT: the accumulated pollutants, including those emitted into the BL and entrained from the FT, can only leave the South Korean peninsula horizontally as polluted plumes to be tracked in the PL stage.

We calculate the temperature and specific humidity of the BL and RL in each grid-cell as mass-weighted averages. Horizontal wind velocities in the BL and RL are also -mass-weighted at ERA5 grid centres, but we compute column-averaged winds over the same set of levels over the entire peninsula to avoid spatial discontinuities. For each timestep, BL winds are vertically averaged from the surface to the median top-of-BL level, and RL winds, from the median top-of-BL level to the median top-of-RL level.

3 Modelling system

The hybrid modelling system is quasi-three-dimensional, accounting for the geographic variations in BL pollution over South Korea. The modelling system follows the chemical

evolution of boundary layer pollution as it travels across South Korea (BL-RL stage), continues to chemically age the air masses leaving the peninsula as isolated pollution plumes (PL stage) and finally as dispersed pollution remnants (DP stage) under realistic, but idealized, atmospheric conditions typical of the region. The BL-RL stage is the most complex, using hourly emissions and meteorology to model the chemical evolution of pollution in the planetary boundary layer as it moves across the South Korean peninsula (see Table 5). We do not explicitly consider the convective transport of BL pollution directly into the FT. Large convective systems lift and disperse BL pollution in reality; however, we follow the horizontal pollution transport evolution across the peninsula and offshore into the PL stage.

The PL stage chemically ages the pollution when BL or RL air masses are first swept offshore. This pollution is collected over 4-hour intervals in BL-RL ghost cells surrounding South Korea, then released as isolated pollution plumes to evolve undiluted for 3 days at 2 km altitude. When these plumes disperse, the remaining primary and secondary pollutants (including O_3) are passed to the dispersed pollutant (DP) stage. Here, we assume that pollutants are dilute enough that the chemical response is first-order with respect to the number of moles of dispersing pollutant, and can be calculated separately for each species based on the observed background composition of the mid-latitude Pacific troposphere. Each pollutant's impact is independent of the other pollutants. The DP stage mixes the remaining pollutants from the PL stage uniformly across the 1-9 km altitude range and calculates the O_3 and CH_4 budget terms across four altitude ranges (2±1, 4±1, 6±1, and 8±1 km) to. Every 30 days the pollutants are remixed vertically. After 120 days the chemically active pollutants are mostly gone and a simple extrapolation from the last 30 days can be used to estimate any remaining O_3 and CH_4 reactivity.

The sequence of modelling operations is summarised in Table 5, and details of the calculations are described below.

Table 3. 5: *A summary of the modelling operations acting on South Korean air pollution.*

Processes	Timestep	Description
Boundary layer-residual layer (BL-RL) stage (3.1)		
Chemical integration (3.1.1)	1 hr	Update the solar time (*J*-values) and integrate the chemistry (including dry deposition and aerosol loss) in BL and RL columns. Update the BL and RL chemical concentrations, keep track of the moles of primary and secondary pollutants, and diagnose the reactivity of O_3 and CH_4.
Emissions (3.1.2)	1 hr	Deposit an hour of emissions into the BL of each grid cell.
Horizontal transport (3.1.3)	10 min	Follow the horizontal transport of BL and RL masses in six 10-min substeps with remapping onto the standard grid cells at each substep. For the ghost cells, accumulate transported air mass for 4 hours before releasing as a pollution plume (PL).
Vertical remapping (3.1.4)	1 hr	For standard cells, remap the BL and RL mass onto new standard ERA5 levels, partitioning the BL based on the new BL height.
Isolated pollution plume (PL) stage (3.2)		
Initialisation	4 hr	Collect pollution leaving the peninsula in BL-RL offshore ghost-cells during horizontal transport. Release the accumulated air and pollutant mass accumulated over 4 hour intervals from each ghost cell as an individual pollution plume.
Daily integration	1 day	Integrate 24-hour diel chemistry of each plume. Update solar zenith angle at 30 minute resolution. Keep track of the daily O_3 and CH_4 reactivities as well as the evolution of primary and secondary pollutant mass. End integration after 3 days.
Dispersed pollution (DP) stage (3.3)		
Disperse remnants	30 days	Follow the final destruction of the primary and secondary pollutants released from the PL stage. Mix a unit, linear perturbation of each major remnant species over 4 layers in the background atmosphere and integrate the O_3 and CH_4 reactivities in the same manner as the PL stage, but in four altitude bins.
	30 days	Mix the remaining pollutants into the 4 standard layers every 30 days and continue the 30-day integration until 120 days have elapsed.
	120 days	Tabulate the final, linearised O_3 and CH_4 perturbations for the remnant species, summed over the four atmosphere layers and 30-day periods. Extrapolate the O_3 and CH_4 perturbations from any remaining secondary CO based on the tabulated CO results. Combine the linearised O_3 and CH_4 perturbations with the 3-day plume remnants.

The discrete processes for the three modelling stages are outlined and briefly described. The timesteps indicate the frequency at which operations are performed.

3.1 Boundary layer-residual layer (BL-RL) stage

The BL-RL stage is set on a latitude-longitude grid of 60x60, 0.1°x0.1° geographical cells centred on South Korea. The BL-RL domain comprises 1092 terrestrial grid-cells where emissions and chemistry are processed, and 177 ghost-cells on the model domain circumference that collect air transported out of the BL-RL domain. When diagnosed, the BL and RL always consist of a discrete number of contiguous ERA5 layers. The BL always contains the layers from 0-200 m above surface, while RL may be completely absent if fully entrained by the BL, or fully ventilated by horizontal transport. The chemical concentrations in the BL and RL are calculated from the tracked number of moles of pollutants, and the molar dry air column burdens, which are proportional to the sum of the δp levels (see supplemental Table S2) and grid-cell quadrangle areas.

Within the model domain, the BL and RL columns in each cell have a unique mix of pollutants, with a single pressure, temperature and chemical composition. The BL collects, transports, and chemically evolves fresh emissions while depositing O_3 and NO_2 to the surface. The RL collects, transports, and chemically evolves air detrained from the BL when the BL height drops. All air outside the terrestrial cells and in layers above the BL+RL has FT background composition, and this air can enter the BL columns when the BL height rises above the RL layer, or when offshore air is horizontally transported into the terrestrial grid cells.

3.1.1 Photochemistry

The first modelling step in the BL-RL stage is the F0AM integration of hourly chemistry for each BL and RL column. F0AM integrates the chemistry in each column using the pollutant mixing ratios, MCM v3.3.1 rate coefficients, first-order deposition rates (dry, aerosol, and scavenging), mean column meteorology (temperature, pressure, relative humidity), SZAs

computed from grid-cell coordinates and model UTC time, and KORUS-AQ all-sky *J*-values (see Sects. 2.3-2.4). Temperature and pressure are used to calculate the reaction rates and convert mixing ratios to number densities. Budget data such as chemical tendencies and individual chemical rates are integrated at the sub-hourly F0AM ODE solver resolution and diagnosed every hour.

3.1.2 Emissions

Each hourly timestep, after the chemical integration, we inject an hour of emissions into each grid cell given the species-wise emission rates (mol s^{-1}) of the KORUS v5, GFED5, and MEGAN v2.10 inventories (see Sects. 2.1.1-2.1.3). For the KORUS v5 inventories, we multiply the mean emission rate (resolved monthly) by a diurnal activity scale factor (resolved hourly) and a day-of-week activity scale factor (weekday, Saturday, or Sunday). These scale factors are unique to each grid cell and derived from the individual emission sector activities in the cell (see Sect. 2.1.1).

For cells with intense emission sources, the operator splitting poses a challenge. If we release an hour of emissions into each grid-cell before the chemistry operator, then the hour-long chemistry calculation begins with a mass of unrealistically concentrated, undispersed air pollution rather than a ventilated stream of emissions processed continuously. With our current operator sequence, the emissions are transported partly to neighbouring cells before the chemical generation of secondary pollutants. The obvious remedy is to cut the overall operator time-steps to *e.g.* 30 min or even 10 min. Unfortunately, restarting the chemistry integration every 10 minutes is computationally prohibitive for us. However, we can test the errors caused by our operator sequencing by cutting the overall time step to 1/2 hr and 1/4 hr for a 3-day test case.

From 1 hr to 1/4 hr timestepping, we found a +1.3% and +0.9% error in total CH_4 and O_3 reactivity; and from 1/2 hr to 1/4 hr, the errors decrease but change sign, indicating convergence.

3.1.3 BL and RL horizontal transport.

Horizontal advection moves the BL and RL across the peninsular grid, brings in FT background air from offshore, and sends pollution plumes from the model domain to the offshore PL ghost cells. Each hour, we calculate two sets of grid-resolved 2D (u, v) wind fields, one for the BL and one for the RL. We transport each on separate planes following the BL and RL (u, v) trajectories to their new locations. These trajectories are fixed over the 1-hour step and are generally not straight lines. We move each BL or RL cell in a sequence of six 10-minute sub-steps, where each sub-step splits the original (source) cell into four new (receptor) grid cells as depicted in Fig. 5. The four parts of the BL/RL cells are reassembled onto the standard grid cell, and the process is repeated for the remaining 5 sub-steps. Cell fractions transported offshore are collected as pollution plumes for the PL stage. The choice of 10-minute advection timesteps enables intense emissions to horizontally ventilate quasi-continuously along curved trajectories over the hour.

To compute the trajectory paths for each terrestrial BL cell, we adopt a fixed effective BL height for the one-hour time step for all South Korea based on the median top-of-BL height for terrestrial cells (see Sect. 2.4.1). Using this set of fixed ERA5 levels, we calculate a pressure-weighted set of (u, v) fields at the centroids of the 60x60 model cells with bicubic interpolation. The u and v components are converted to angular velocities in per-second degree arcs that remain fixed over the 1-hour time step. We then transport the BL cell to new centroid positions along the arcs via 10-minute Euler-forward-stepping linear trajectories. These 10-minute trajectories are linear and non-deformational and thus allow for easy partitioning into four cells at their destination as shown in Fig. 5. The series of 10-minute sub-stepping trajectories allows

realistic curved and deformational motion of the BL cells (i.e., convergence or divergence). Then we partition the source BL air mass (and pollutants therein) into four receptor cell BLs in proportion to the source-receptor area overlaps. This is repeated 6 times over the hour. The RL cells are transported likewise, but using the RL-weighted (u, v) fields, where the pressure-weighting of the winds ranges from the median South Korean top-of-BL level-edge to the median top-of–RL level edge.

The interpolated BL and RL (u, v) winds will almost certainly include convergence or divergence and thus receptor cells will collect more or less than 100% of their area fractions. This discrepancy, along with the discrepancies in source- and receptor- BL column masses, leads to a change in BL+RL dry-air column masses after each 10-minute step. BL and RL air mass and source cell pollution that is transported outside the terrestrial domain is accumulated in the ghost-cell closest to the transported centroid coordinates. We track BL and RL outflows to ghost cells separately, but do not vertically remap or discretise them in the ghost cell. Their chemical evolution in the PL stage is treated separately and identically. Inshore flow to terrestrial cells provides FT air to the BL in proportion to the source-receptor area-overlap and receptor BL column mass. We assume RL pollution does not mix with FT air, so we ignore offshore transport into the terrestrial RL.

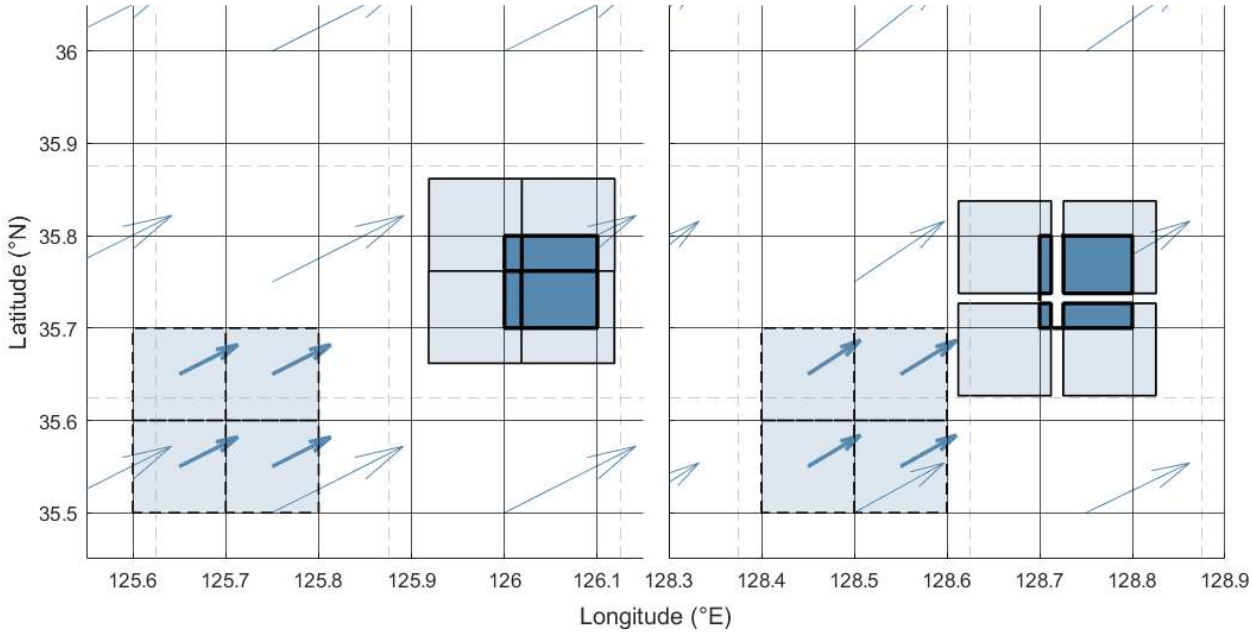

Figure 3.5: *A schematic of the BL-RL stage horizontal transport.*

Left: the receptor BL column (dark-blue square) receives air mass from four source BL columns (dashed light-blue squares) transported north-eastward in a straight-line path without divergence over a 10-minute step. The new receptor BL comprises a fraction of each source BL column in proportion to the rectangular overlap after transport (dark-blue rectangular areas). Right: As described above, but in a divergent wind field. The four adjacent light-blue cells separate, and the white cross-shaped area in the receptor cell is vacuous. Wind vectors (arrows) are sampled centrally in the ERA5 grid (dashed grid), vertically averaged in the BL, and interpolated to the model grid cell centroids (bold arrows) to determine the source cell trajectories.

3.1.4 Vertical remapping of the BL-RL

With each 1-hour timestep, we have new ERA5 fields for surface pressure and BL height. As described in Sect. 2.4, the new BL height in meters is used to select the new upper BL edge-level in hPa that most closely matches it. If the BL top after horizontal transport lies above the new one (i.e., a falling BL) then the polluted air mass between the new and old BL is added to and mixed with the overlying RL, creating a new RL if none initially existed. If the new BL top lies above the new one (i.e., a rising BL) then the new BL takes in the mass from the RL. If the available RL mass is insufficient then the BL entrains mass and chemical pollutants (including O_3) from the FT. The BL-RL-FT exchange during the vertical remapping step depends on BL height dynamics (*i.e.*, the change in BL height over the last hour), but is also convoluted by

horizontal transport (*i.e.*, convergence or divergence in BL and RL trajectories). The BL and RL columns transported into a grid-cell at the end of the time step will not align with the BL in the receptor grid-cell and model levels and must be remapped as illustrated in Fig. 6. In Fig. 6.a, the new BL air mass (right column) exceeds the BL+RL masses (left column), and thus it entrains all pollutants in the BL and RL plus those in the FT needed to make up the total air mass (thick black bars). In Fig. 6.b, the new BL mass sits in the middle of the transported RL, and thus some of the transported RL goes into the new BL, and the remainder, into the new RL. The new RL is rounded up to the next level by adding FT mass (and FT pollutants) into the RL. In Fig. 6.c, the new BL mass is less than the transported BL mass, and the excess is placed into a new RL.

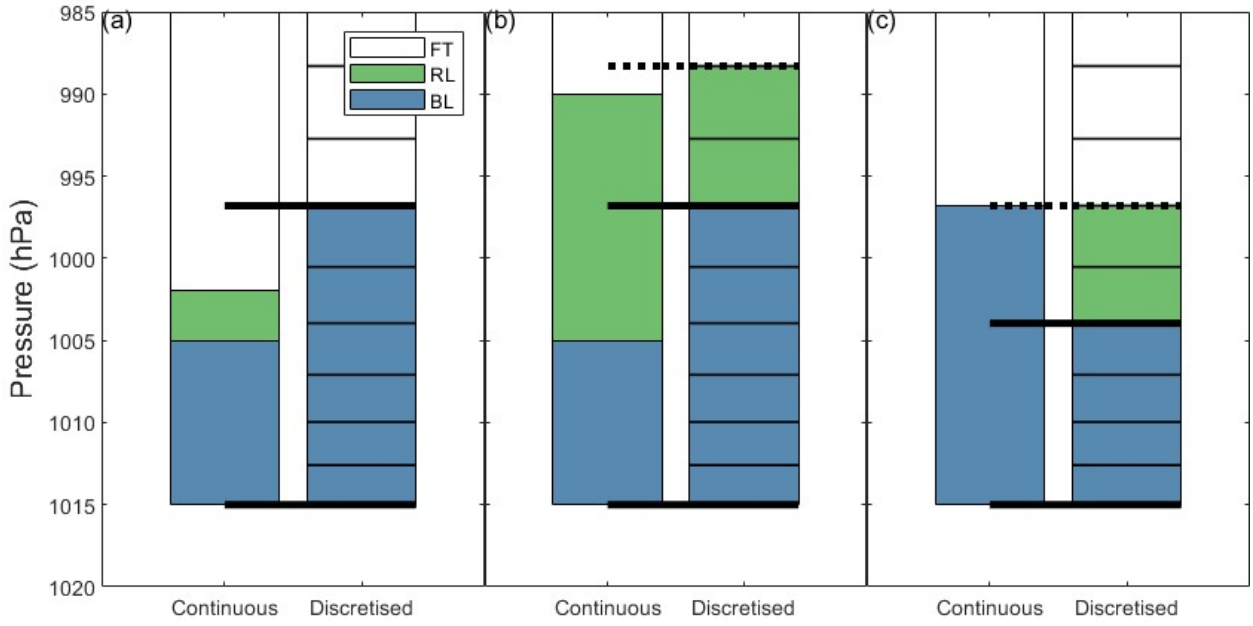

Figure 3.6: *Schematic of the BL-RL stage vertical remapping.*

The four panels show the re-gridding of a BL (blue) and RL (green) air masses that have been left in a new cell after the horizontal transport step. The new cell is marked with the pressure edge levels based on the new surface pressure and a BL mass (blue) based on the new BL height; see text. Three examples here are: (a) incoming BL+RL mass is less than new BL mass, so BL+RL+FT is pulled into the new BL and the RL disappears; (b) BL+RL mass exceeds new BL mass, so some RL is absorbed into the new BL and a new, smaller RL is created with some FT air incorporated; and (c) incoming BL mass exceeds the new BL and so an RL is created.

3.1.5 Surface observations

We compare our BL results for O_3, CO, and NO_x with grid-cell averaged observations derived from the NIER network (Sect. 2.2.2) using the methodology of Wilson and Prather (2025). In supplement S3 we show model-observation statistics and plots, sampled in "urban" grid-cells that were effectively observed by five or more NIER sites. The time series is decomposed into four meteorological phases described by Peterson *et al.* (2019), named as *dynamic* (01-16 May), *anticyclone* (17-22 May), *transport* (25-31 May), and r*ex-block* (01-07 June). Our model performance and diurnal cycles for O_3, CO, and NO_x were consistent with a separate study that used the WRF-Chem v4.4 chemistry-transport model (CTM) driven by the same KORUS v5 inventory (see supplemental Table S3 and Figs. S2-6; see Fig. 2 from Kim *et al*., 2024). Modelled O_3 correlated well with observations (R = 0.6-0.8), NO_x, less so (R = 0.5), and CO was uncorrelated (R = 0.3). The mean biases of model daytime O_3 ranged from -1 ppb (anticyclone and transport phases) to +21 ppb (dynamic and rex-block phases); model NO_x bias ranged from -7 ppb to -17 ppb, and model CO had extreme biases of -120 to -240 ppb. Ozone overestimates occurred during meteorological phases with high transboundary influence (Miyazaki *et al.*, 2019), and this factor was not reflected in our model boundary conditions. Nitrogen oxide measurements from the NIER network are known to have an "NO_2 artifact" that introduces a +4 ppb bias in our data (Jung *et al*., 2017), accounting for some of the bias in our model. Our model CO bias is similar to that reported by Kim *et al*. (2024). Compared with DC-8 profiling in the BL, NIER CO data was notably biased by around +100 ppb (Wilson and Prather, 2025), and we believe this identifies a bias problem with the NIER CO data.

3.2 Pollution plume (PL) stage

We assume that pollution leaving South Korea in the RL or BL masses is maintained as an undiluted pollution plume for several days, as often seen in aircraft observations (Crawford *et al*., 2004; Heald *et al*., 2004; Liang *et al*., 2007). Following Prather and Jaffe (1990), we assume that sharp concentration gradients along plume edges are maintained by windshear, largely conserving plume mass and concentrations until its final dissolution. Our model allows for the plume to last for up to three days before it is ultimately sheared and shredded, losing its integrity and dispersing the remaining pollution, highly diluted, into the background atmosphere.

We separately collect the BL and RL air and pollution masses that are transported beyond the terrestrial grid into the 177 ghost cells that line the coast. We collect and release the BL and RL masses from each ghost cell every six hours starting at midnight local time. Considering the 45-day KORUS period and the 2 spindown days to clear pollution at the end, there are a maximum of 47 x 6 x 177 = 49,914 plumes in the BL and RL each, but because not all ghost cells collect pollution every 4 hours, the numbers are 32,954 and 30,632 respectively. Each plume is integrated at a fixed temperature, pressure, and relative humidity (284 K, 797 hPa, and 72%) based on the ATom climatology at 2 km altitude (Table 2). The same F0AM chemical model used in the BL-RL stage is used to integrate a sequence of three 24-hour periods for each plume, starting at the hour of its release. *J*-values were rescaled using KORUS-AQ all-sky scale factors above the clouds (see Sect. 2.3.2) and updated every half-hour. The pollution content and accumulated reactivities of O_3 and CH_4 were stored daily for each plume.

A key uncertainty in the PL stage arises from the largely unknown dynamical timescales of plume dilution; these timescales are important because the total O_3 and CH_4 reactivities increase with dilution. Our base case asserts a 3-day dynamical lifetime for all plumes, but with

our daily diagnostics for each plume we can re-evaluate our cumulative GHG budgets assuming 2 days, 1 day, or 0 days of plume aging. We find that aging pollution beyond 3 days only marginally affects the budget terms, and we discuss the impact of shorter aging times in Sect. 4. Fig. 7 shows the evolution of plume nitrogen and VOC species that contribute significantly to DP stage reactivity.

To provide a reference value for the reactivities in the BL-RL and PL stages, we repeat the PL integrations for control plumes initialized from a control BL-RL run with no anthropogenic emissions (KORUSv5 and GFED5). Subtracting the control run budgets from the standard run budgets yields the budget perturbations induced by South Korean emissions.

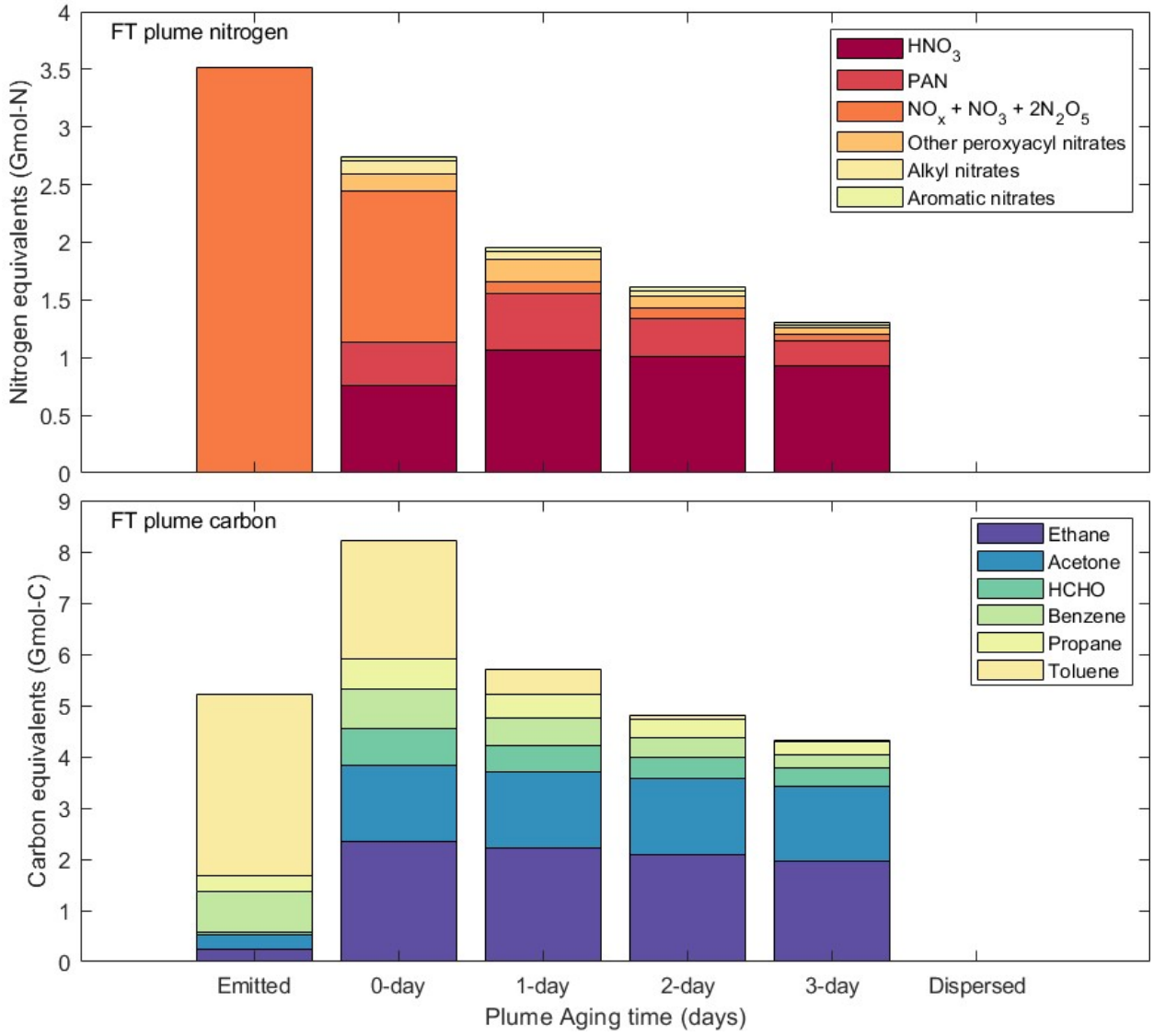

Figure 3.7: *Total NOy-nitrogen (Gmol-N, top) and VOC-carbon (Gmol-C, bottom) pollution content emitted in the BL-RL stage and aged in the PL stage.*

"Emitted" designates initial anthropogenic emissions, and "0-day" aging shows the pollution exiting the BL-RL stage, which includes biogenic emissions and background air. Only species with high impact on the O_3 and CH_4 budgets in the DP stage are shown. Loss of total nitrogen occurs through nitrate aerosol formation and gas-phase HNO_3 scavenging. Loss of total carbon occurs through formation of non-plotted secondary VOCs, carbon monoxide, and carbon dioxide. Most ethane in the plume is from background air (i.e., not emitted) which does not impact the budgets.

3.2.1 Airborne observations

The DC-8 aircraft sampled South Korean pollution on 20 days in May and June 2016, vertically profiling the Seoul Metropolitan Area on most flight days and chasing offshore pollution plumes

based on tracer-transport forecasting. We expect the composition of freshly exported plumes from the BL-RL stage to resemble *in situ* observations in the South Korean BL. In our comparison, we sum observed reactive N species into NO_y-nitrogen in moles of N, specifically NO, NO_2, PAN, and PPN. We do not include other nitrates such as NO_3 and N_2O_5 as they were not individually observed, but measured in combination with HNO_3 and particulate nitrate. Likewise, we sum all VOCs measured at high frequency (1 Hz) into VOC-carbon in moles of C. VOC-carbon includes ethane, benzene, toluene, isoprene, methacrolein, acetaldehyde, acetone, methyl ethyl ketone, methyl vinyl ketone, and formaldehyde, but not CH_4, CO, or CO_2 (KORUS-AQ Science Team, 2019).

Fig. 8 shows the 2D histograms of NO_y-nitrogen and VOC-carbon in our model plumes aged 0 and 1 day, and in the observations sampled above and below the BL height, as resolved hourly at 0.25° x 0.25° in the ERA5 data. See supplemental Fig. S7 for a map of DC-8 sampling. The dominant plume compositions in the 0-day-aged plumes and BL observations centre on 1.0-3.0 ppb NO_y-nitrogen and 15-25 ppb VOC-carbon, with around +5 ppb more VOC-carbon in the observations. Such a pattern was also observed in transects through Seoul pollution transported west over the Yellow Sea on 22 May. Observations with >10 ppb NO_y-nitrogen were frequent in the densely sampled Seoul Metropolitan Area and also in fresh urban and industrial plumes off the west (22 May and 05 June) and southeast coast (07, 11, 20, and 30 May); modelled plumes with this range of compositions were also found. After 1-day aging, the modelled plumes had a range of NO_y-nitrogen concentrations resembling FT observations, but with greatly diminished abundances of short-lived aldehydes and alkenes. From this comparison, pollution plumes sampled in the FT, primarily offshore from South Korea, were probably aged less than a day.

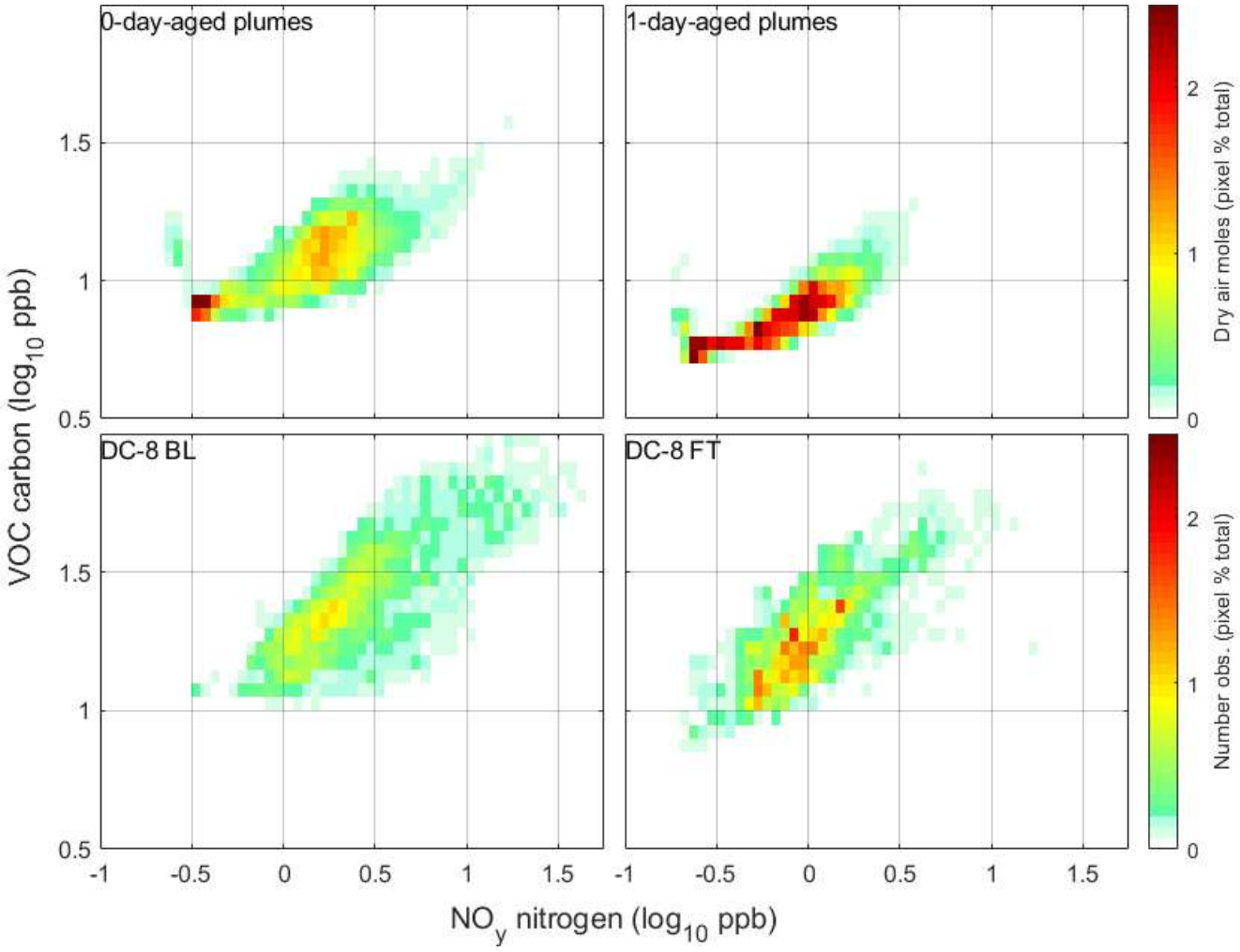

Figure 3.8: *2D distribution of VOC-carbon vs. NO_y-nitrogen in modelled plumes and DC-8 observations. Shown are modelled plumes aged 0-days (top-left) and 1-day (top-right), and DC-8 observations of the BL (bottom right) and FT (top right). Probability densities (colour bar) are normalised total moles (top) and number of observations (bottom) resolved as pixels of 0.05 $\log_{10}$ ppb width. Geographic sampling of DC-8 data is shown in supplemental Fig. S7.*

3.3 Dispersed pollution (DP) stage

We model the DP stage as a linearly separable chemistry problem. Specifically, we assume that the dispersion of a pollution plume results in a perturbation to the atmospheric chemistry that is sufficiently dilute so that the interaction of two pollutants (*i.e.*, the second-order terms) is negligible. The impact of any pollutant is thus in the linear regime and can be scaled from the

integration of a small perturbation. We create a look-up table relating moles of O_3 and CH_4 produced or lost per moles of pollutant X dispersed.

The chemical response of the atmosphere to an added pollutant depends on chemical composition, pressure, temperature, *J*-values, aerosols, *etc*. Since we do not model transport in the PL stage, we do not know where the plumes disperse, nor where the remnants are transported afterwards. We choose to disperse the pollutants across four tropospheric layers whose composition is derived from ATom-4 measurements (27 April, 29 April, and 21 May 2018) sampled between 2±1, 4±1, 6±1, and 8±1 km altitude over the northern midlatitude Pacific (see Table 2). At each of the four altitudes we integrate the reactivity of the atmosphere with the addition of 0.1 ppb of pollutant and then subtract a control run made without the added pollutant.

Unfortunately, as the pollutant decays, the background atmosphere also evolves, resulting in a chemical mixture after 30 days that differs greatly from the initial ATom free troposphere. The observed free tropospheric composition is maintained by several non-local processes that are not included in our box model (e.g., lightning NO_x, convective mixing of surface pollution, washout scavenging, injection of stratospheric O_3). Thus, in our F0AM box model we introduce artificial sources or sinks to maintain a stable composition (see Table 6). These artificial terms are derived for the major free-troposphere species at each level with an iterative sequence. First, we fixed the concentrations of the controlled species (NO_x, O_3, CO, H_2O_2, ethane, propane, *n*-butane, benzene, toluene, acetone) and integrate the full chemistry for 30 days, allowing the numerous short-lived secondary species to achieve some balance. For controlled species with daily net losses, we add an artificial source to match the loss. For those with excess production, we estimate a first-order loss to balance it. Applying these artificial source/sink terms, we run a 365-day constant-summertime spin-up with primary species evolving. We rescale the source/sink

terms by the ratio of the initial-to-final concentrations. This process is iterated, with some Aitken acceleration for O_3, until the end-of-year concentrations differ by less than 1% from the initial ATom values (Table 2). This provides a stable chemical composition upon which to integrate the impact of decaying pollutants.

The DP stage F0AM calculations are integrated as for the PL stage (*i.e.*, constant meteorology, 30 min SZA timestepping, fixed CH_4 and water vapour, and KORUS-AQ all-sky *J*-values sampled above 1.5 km) for the four altitude bins in Table 2. For each pollutant, we follow the decay of a small enhancement (+0.1 ppb) on the four altitude levels for 30 days. We then collect the remaining moles of pollutant and secondary products (e.g., CO from VOCs) from the four levels, mix them and redistribute again across the four levels (Table 2). This 30-day timescale for mixing is consistent with the vertical age gradients of 3-4 days per km found in 3D models (Prather 2025, Fig. 9). We repeat this sequence (age 30 days and then mix across levels) three times for 120 days total, effectively oxidizing almost all of the original and secondary pollutants. The vertical mixing is needed to allow the total pollution to decay because the chemical loss of several species is extremely slow if left in the upper troposphere.

For each perturbation by pollutant X, we calculate this 120-day sequence and compare with a reference run made without added pollution. For CH_4 loss (total in ppb), we sum the $OH+CH_4$ reaction rate for pollution minus control runs. With CH_4 fixed in our model, this directly gives us the pollution-driven net loss. For O_3, the diagnosis of net production is more difficult because the chemistry both produces and destroys O_3 on a time scale of weeks. The use of odd-oxygen production rates to represent O_3 production is fundamentally flawed because these rates depend on the O_3 abundance (see, Guo et al., 2023; Prather & Zhu, 2024). Thus, we use the integral of the O_3 perturbation (ppb days) at each altitude over the 120-day DP

integration and divide by the O_3 perturbation lifetime (days) for that altitude. Provided that the O_3 perturbation has fully decayed, this quotient is exactly the net O_3 produced (ppb). For proof, see Prather (2007). The O_3 perturbation lifetime given in Table 6 at each altitude is a well-determined, well-defined value since it is derived from a pulsed O_3 addition and integrated for 120 days (without vertical mixing). With vertical mixing every 30 days, our derivation of net O_3 production is only approximate because we do not follow the perturbation from beginning to end under a single chemistry. For the most part, the O_3 perturbation from pollutant X occurs at the beginning of the 30 days and decays by the end. We do not tabulate the O_3 perturbation caused by an O_3 pollutant since that would be double counting, but we do calculate the CH_4 perturbation caused by O_3.

The O_3 perturbation lifetime at 2 km altitude (5.8 days) is used to calculate the PL stage net production by accounting for the limited decay over 1-3 days. For the DP stage we can simply divide the integrated perturbation (ppb-days) by lifetime (days) to obtain net production (ppb). We rescale these net reactivities by the amount of primary pollutant X used in the calculation to derive dCH_4/dX and dO_3/dX in mol mol^{-1}. The total impact of all pollution released to the DP stage (see Fig. 7) is given in Table 7. We find that PAN and peroxypropionyl nitrate (PPN) produce similar dCH_4/dX and dO_3/dX reactivity values to NO_2 and NO, and hence we apply the reactivities of NO_2 to all peroxyacyl, alkyl, and aromatic nitrates that we did not calculate explicitly.

Table 3.6: *Dispersed plume model parameters and resulting O_3 lifetime*

Species	**Source, molec cm^{-3} s^{-1} (Sink, s^{-1})**			
	2 km	**4 km**	**6 km**	**8 km**
NO	19500	8190	5810	3780
NO_2	0	0	0	0
CO	808000	421000	251000	143000
Ethane	14200	6440	2970	1300
Propane	3690	1570	634	533
n-Butane	711	297	183	139
n-Pentane	0	0	0	0
Acetone	2770	2320	1790	1340
Benzene	1410	473	255	184
Toluene	117	36	37	29
O_3	586000	212000	43500	(8.35E-08)
H_2O_2	(2.60E-05)	(6.84E-06)	(3.96E-06)	(8.20E-07)
O_3 perturbation lifetime (days)	5.8	10.8	17.9	24.2

Sources (molec cm^{-3} s^{-1}) and sinks (s^{-1}) represent the atmospheric processes that maintain a quasi-steady-state for each species for the ATom background atmosphere adopted here. The O_3 lifetimes are derived from the decay of a unit O_3 perturbation at each altitude. Methyl hydroperoxide, which was not constrained in the DP stage, equilibrated at 0.42, 0.30, 0.16, and 0.06 ppb in the altitude bins from 2 to 8 km compared with 0.71, 0.55, 0.40, and 0.23 ppb observed in ATom, consistent with the long-standing view that convection of BL CH_3OOH (not included here) provides a major FT source (Prather and Jacob, 1997).

Table 3.7: *CH_4 and O_3 budget perturbations in the DP stage from the more important individual pollutants.*

Pollutant	**Emissions (Gmol)**	**Dispersed (Gmol)**	**ΔCH_4 (Gmol)**	**ΔO_3 (Gmol)**
CO	7.3	7.0	+2.8	+1.6
O_3	N/A	14.4	-1.8	0
PAN	N/A	0.17	-1.9	+5.1
NO_x	3.5	0.04	-0.4	+1.2
Other peroxyacyl nitrates	N/A	0.05	-0.5	+1.4
Alkyl nitrates	N/A	0.02	-0.2	+0.6
Aromatic nitrates	N/A	0.02	-0.2	+0.6
Benzene	0.1	0.04	-0.0	+0.2
Toluene	0.3	-0.01	-0.1	-0.1

"Emissions" includes 45 days of anthropogenic South Korean emissions (KORUS v5 + GFED5). "Dispersed" values are the pollution remnants after BL-RL processing and 3 days of aging in the PL stage. ΔCH_4 and ΔO_3 are the budget perturbations caused by individual pollutants in the DP stage, and are proportional to the moles of dispersing pollutants. "Dispersed" negative toluene is caused by chemical loss of toluene in entrained FT air that exceeds emissions.

4 Ozone and methane budgets

We calculate the impact of South Korean pollution on O_3 and CH_4 by differencing a full emission run and a reference control run without KORUS v5 anthropogenic and GFED5 biomass burning emissions. Our assessment is for the 45 days of emissions (02 May to 15 June 2016) covering the KORUS-AQ mission in South Korea. We follow 2 spin-down days (16-17 June 2016) without industrial or biomass burning emissions to account for the 45 days of pollution leaving the peninsula. We calculate the budget terms (Gmol) for O_3 and CH_4 directly from all BL, RL, and PL air masses, and then add on DP stage by scaling the dO_3/dX and dCH_4/dX factors by the amount of each pollutant X (Gmol) released into the free troposphere.

Following the O_3 budget requires careful accounting. The change in O_3 during the BL-RL stage relative to the control occurs on the order of one day and is almost a direct measure of the net production (loss). Over that time, the net production will decay. The average residence time for dry air in the BL-RL stage is 8 hr (mean South Korean BL+RL mass per daily offshore export), but for chemically-produced O_3, it is 12 hr. Based on Table 6, we select 4.5 days as the BL-RL O_3 perturbation lifetime at 1 km altitude, and thus, net production of O_3 occurring uniformly across 12 hr will decay on average by over 5.4% by the end of the day. We multiply the BL-RL O_3 perturbation that is put into the PL stage by the reciprocal decay (1.06) to estimate net BL-RL production. The BL-RL stage often produces large net losses from cells with high NO_x emissions, and we assume these perturbations also decay with the 4.5-day timescale. Our method of extracting net BL-RL O_3 production is only approximate because the O_3 perturbation lifetime is likely variable depending on chemical regimes, and the time spent by pollution in the BL-RL stage can vary from hours up to 2 days.

Deriving the net O_3 production from the PL stage is more straightforward. There are three successive 24-hour days of plume chemistry integration, occurring under the same atmospheric conditions (2 km) but under different chemical conditions. We do not attempt to derive the O_3 lifetime for each PL case, but make the approximation that it is the same as the free troposphere in the 2 km DP case (5.8 days). At the start of each PL day, we have an O_3 perturbation that is carried forward from the previous day: for day 0 it is the O_3 perturbation from the BL-RL masses that collected in the plume; for days 1-to-3 it is the perturbation at the end of the previous day relative to the control. We assume that this external O_3 perturbation decays with a 5.8-day lifetime (i.e., 16% day^{-1}). The net internal O_3 perturbation at the end of the day caused by the PL chemistry is then the O_3 at the end of the day minus the decayed residual of the external

perturbation from the beginning of the day relative to the control run. Because of decay over the 24-hour plume integration, the net internal perturbation is increased by 9% to get the net production. This complex sequence allows us to account for the effective net O_3 production over the PL stage without double counting. When we integrate the impact of an O_3 perturbation passed on to the DP stage, the integral of CH_4 reactivity is straightforward and must be included, but the integral of the O_3 perturbation itself cannot be included since its net production was already accounted for in the previous stages.

The total CH_4 and O_3 reactivities attributed to the 45 days of emissions are -4.3 Gmol and +31.3 Gmol, respectively, for 3-day plume lifetime (see Table 8). For both species, 85% of the reactivity occurs during the 45-day emission period, and the remaining 15% occurs over the following 2 months (see Fig. 9 for reactivity timeline). Table 8 shows the budget terms during the individual model stages, the ozone enhancements that resulted from production, and the ozone production efficiencies (OPE = molar production of O_3 per molar loss of NO_x). Methane and O_3 reactivity occurs mostly in the PL and DP stages, wherein the total budgets are highly responsive to aging time in the plumes (PL stage). Our standard diagnostics are for 3-day plumes, and reducing this lifetime results in much larger reactivities. Varying the plume aging time from 3 days to 2 days results in the addition of -0.5 Gmol-CH_4 and +1.9 Gmol-O_3 to the budgets. Varying from 2-to-1 days results in -1.0 Gmol-CH_4, and +2.7 Gmol-O_3, and from 1-to-0 days, -8.3 Gmol-CH_4 and +20.5 Gmol-O_3. The range of reactivities from instant dilution to infinite aging is 11 Gmol-CH_4 and 31 Gmol-O_3 assuming geometric convergence with a common ratio of 1/2. Hence, the change in reactivities from 3-to-2 days aging in plumes accounts for just 5% of the possible range of reactivities, with 10% from 2-to-1 days, and 75% from 1-to-0 days. The true timescales of pollution plume dilution are presently unknown but

likely on the order of a few days. Global models commonly dilute pollution plumes too rapidly (Zhuang *et al*., 2018), and could vastly overestimate the O_3 and CH_4 budget contributions from anthropogenic pollution as a result.

The OPEs in our model stages are diagnosed from the tabulated O_3 production and the loss of reactive nitrogen (NO_x, NO_3, $2N_2O_5$, HO_2NO_2, HONO, PAN and other peroxyacyl nitrates, alkyl nitrates, and aromatic nitrates) (not shown). The BL-RL and PL stage OPEs are consistent with Oak *et al*. (2019) urban South Korean BL OPEs and box modelled DC-8 OPEs that were diagnosed from instantaneous NO_2 formation, odd-oxygen loss, and NO_2-OH oxidation rates. Since half of our NO_x-loss comes from nocturnal N_2O_5 aerosol reactivity, our OPEs are halved compared with Oak *et al*. (2019). The DP stage OPE diagnosed from pure NO_x dispersion follows the classic non-linear response to NO_x levels (Liu *et al*., 1987) and is close to the OPE from aviation NO_x (31 mol mol^{-1}; Prather and Zhu, 2024).

Table 3.8: *Total CH_4 and O_3 budget perturbations and OPE over 45 days of South Korean air pollution.*

Model stage	**CH_4 reactivity (Gmol)**	**O_3 reactivity (Gmol)**	**O_3 perturbation (Gmol days)**	**OPE (Gmol $Gmol^{-1}$)**
BL-RL	-0.3	+4.0	1.8	2.3
3-day PL	-1.7	+16.3	33.9	11.2
DP (3-day PL)	-2.3	+10.9	284	27.8
Total (3-day PL)	-4.3	+31.2	320	8.9
Total (2-day PL)	-4.8	+33.1	351	-
Total (1-day PL)	-5.8	+35.8	389	-
Total (0-day PL)	-14.1	+59.0	687	-
Total (emissions directly to DP)	-30.1	+103.2	1250	-

CH_4 and O_3 reactivities are net productions (negative = loss) summed over the individual modelling stages, and as totals for all stages given varying plume aging times. O_3 perturbations are the integrated enhancements of O_3 (Gmol) summed during the stages, and as model totals. Ozone production efficiency (OPE) is computed as the net O_3 production (i.e., "O_3 reactivity") per NO_y-nitrogen loss (mol mol^{-1}) over several stages, or in total. The DP stage OPE excludes secondary NO_y perturbations from dispersing VOCs.

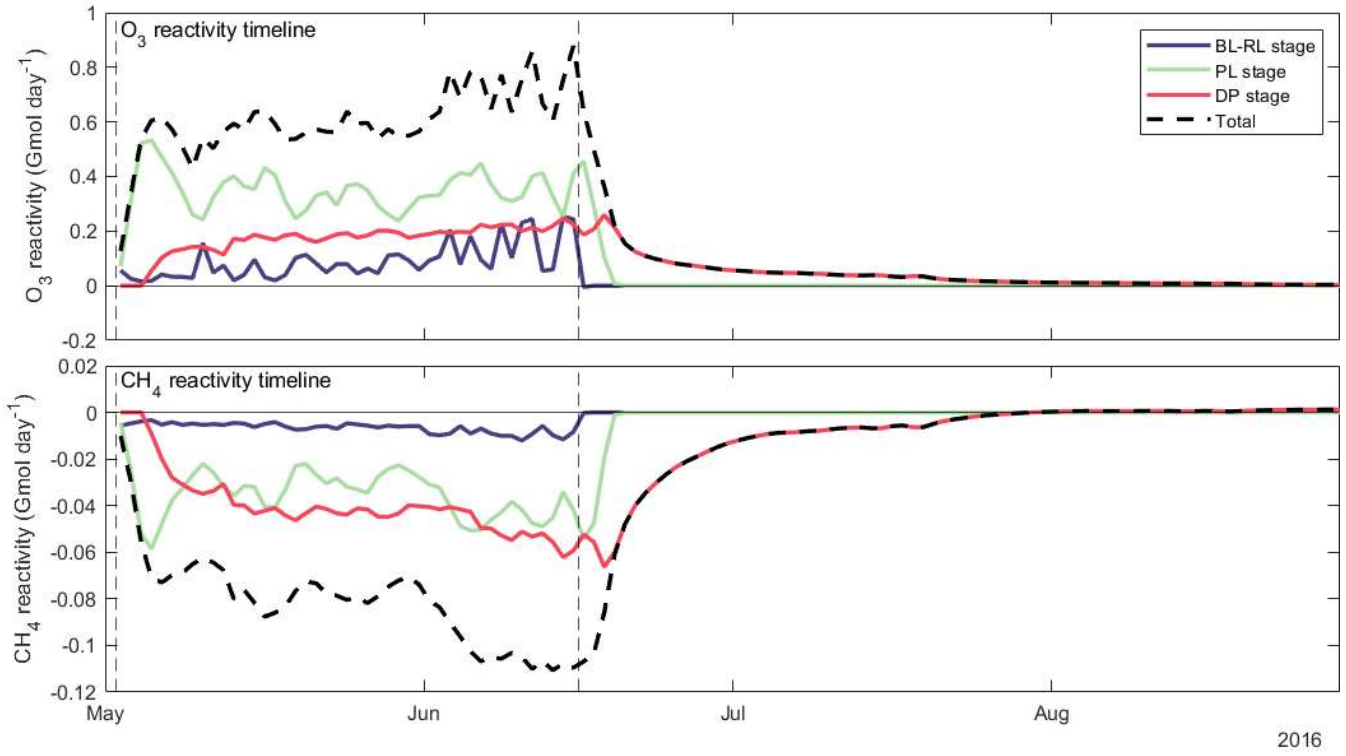

Figure 3.9: *The timeline of O_3 and CH_4 reactivity from 45 days of emissions.*

The 45-day emission period is enclosed by dashed lines and is followed by a two-day spin-down period. Ozone and CH4 reactivities (Gmol day-1) are shown at daily resolution for the BL-RL stage (blue), PL stage (red), and DP stage (green) and integrate to the model stage budgets in Table 9. The BL-RL reactivities are plotted as daily sums over the model domain for CH4 and over the initial exported plume enhancements for O_3. The PL reactivities are plotted as daily O_3 and CH_4 reactivities in the plumes during aging, synchronised to the timeline according to the plume release times. The DP reactivities are dispersed pollution O_3 and CH_4 changes synchronised to the dispersion of each plume. Daily total reactivities (dashed black line) are the sums of the coloured lines. The spinup of pollution is clear in the first 5 days, and the increasing trends in total reactivities over the next 40 days is driven by the accumulation of DP stage reactivity (green line), and partly by the shift in meteorological conditions in the last 10 days where a longer BL-RL residence time resulted in larger BL-RL reactivities.

5 Conclusion

Our modelling system calculates the tropospheric OH-loss of CH_4 and the net production of O_3 from South Korean air pollution during the May-June 2016 KORUS-AQ period. Methane loss is diagnosed from CH_4+OH rate in all three modelling stages, from boundary layer to plumes to the ultimate dispersion in the free troposphere. Ozone production is inferred through the integrated O_3 perturbation (*i.e.*, mole-days) and our calculation of the O_3 perturbation lifetimes (*i.e.*, days). This use of a perturbation lifetime to derive the effective "emission" of O_3 is necessary because

the typical modelling approach of using the odd-oxygen rates (e.g., Griffiths et al., 2021) fails to account for the feedbacks of O_3 on the production of odd-oxygen as discussed in Prather and Zhu (2024).

The total perturbations to CH_4 and O_3 caused by 45 days of South Korean air pollution are -4.3 Gmol and +31.3 Gmol respectively. The global annual tropospheric CH_4 loss for this period is about 35,200 Gmol (Saunois *et al*., 2025), and hence the 45-day global loss is 4,300 Gmol. The tropospheric O_3 budget is more complex than the CH_4 budget, but if we take a simple estimate from the models reporting odd-oxygen rates in Griffiths et al. (2021), we have a mean tropospheric burden of 7020 Gmol (337 Tg-O_3) and a production time of 27 days. Thus, the global reactivity for the 45-day KORUS period is -4,300 Gmol CH_4 and +11,700 Gmol O_3. We estimate the South Korean NO_x emissions to be of order 1% of global anthropogenic emissions (Hoesly et al., 2018), and scaling this gives 10% of total CH_4 loss and 27% of total O_3 production attributable to anthropogenic pollution. Our scaling estimates are simplistic and biased high because the reactivity of pollution depends greatly on latitude and season. The KORUS-AQ campaign was during a period of greatest photochemical activity. Unfortunately, we do not have the data sets and capability to repeat this study with the full annual cycle of Korean pollution.

The O_3 and CH_4 reactivities are highly sensitive to the aging of pollution in plumes. If the plumes disperse to the free troposphere immediately (0-day PL in Table 9), the total reactivities approximately double our standard estimates for 3-day aging. Typically, global models fail to preserve interior plume concentrations beyond a few days at best due to numerical diffusion (Zhuang *et al.*, 2018). The inability to maintain pollution in large-scale plumes is probably one of the larger sources of error in CTMs, and the community would benefit from observational

studies on pollution plume dynamics to establish the typical timescales of mixing into the free troposphere. Atmospheric chemistry MIPs could incorporate our results by performing a regional air quality CTM study, e.g. for South Korea, and comparing the resulting CH_4-OH loss and O_3 mass perturbations. Diagnosing O_3 production from the mass perturbations, as done in this work using lifetimes, remains a challenge.

Code and Data availability

All KORUS-AQ data used in this paper are available via https://doi.org/10.5067/Suborbital/KORUSAQ/DATA01 (KORUS-AQ Science Team, 2019). Model code and datasets for analysis are available via Wilson, 2025.

Author contributions

CPW co-designed the modelling system, wrote the model code, performed the analysis, and co-wrote the manuscript. MJP strategised the modelling study, co-designed the modelling system, and co-wrote the manuscript.

Competing interests

The contact author has declared that neither of the authors has any competing interests.

Acknowledgements

We acknowledge the European Centre for Medium-Range Weather Forecasts for providing the meteorology used in our study, and NASA, for providing the trace gas data.

Financial support

This research has been supported by the National Aeronautics and Space Administration (grant no. 80NSSC21K1454) and the National Science Foundation (grant no. AGS-2135749).

References

1. Bi, C. and Isaacman-VanWertz, G.: Estimated timescales for wet deposition of organic compounds as a function of Henry's law constants, Environmental Science: Atmospheres, 2, 1526–1533, https://doi.org/10.1039/D2EA00091A, 2022.
2. Bloss, C., Wagner, V., Jenkin, M. E., Volkamer, R., Bloss, W. J., Lee, J. D., Heard, D. E., Wirtz, K., Martin-Reviejo, M., Rea, G., Wenger, J. C., and Pilling, M. J.: Development of a detailed chemical mechanism (MCMv3.1) for the atmospheric oxidation of aromatic hydrocarbons, Atmospheric Chemistry and Physics, 5, 641–664, https://doi.org/10.5194/acp-5-641-2005, 2005.
3. Bourgeois, I., Peischl, J., Thompson, C. R., Aikin, K. C., Campos, T., Clark, H., Commane, R., Daube, B., Diskin, G. W., Elkins, J. W., Gao, R.-S., Gaudel, A., Hintsa, E. J., Johnson, B. J., Kivi, R., McKain, K., Moore, F. L., Parrish, D. D., Querel, R., Ray, E., Sánchez, R., Sweeney, C., Tarasick, D. W., Thompson, A. M., Thouret, V., Witte, J. C., Wofsy, S. C., and Ryerson, T. B.: Global-scale distribution of ozone in the remote troposphere from the ATom and HIPPO airborne field missions, Atmospheric Chemistry and Physics, 20, 10611–10635, https://doi.org/10.5194/acp-20-10611-2020, 2020.
4. Bourgeois, I., Peischl, J., Neuman, J. A., Brown, S. S., Thompson, C. R., Aikin, K. C., Allen, H. M., Angot, H., Apel, E. C., Baublitz, C. B., Brewer, J. F., Campuzano-Jost, P., Commane, R., Crounse, J. D., Daube, B. C., DiGangi, J. P., Diskin, G. S., Emmons, L. K., Fiore, A. M., Gkatzelis, G. I., Hills, A., Hornbrook, R. S., Huey, L. G., Jimenez, J. L., Kim, M., Lacey, F., McKain, K., Murray, L. T., Nault, B. A., Parrish, D. D., Ray, E., Sweeney, C., Tanner, D., Wofsy, S. C., and Ryerson, T. B.: Large contribution of biomass burning emissions to ozone throughout the global remote troposphere, Proceedings of the National Academy of Sciences, 118, e2109628118, https://doi.org/10.1073/pnas.2109628118, 2021.
5. Brook, J. R., Zhang, L., Li, Y., and Johnson, D.: Description and evaluation of a model of deposition velocities for routine estimates of dry deposition over North America. Part II: review of past measurements and model results, Atmospheric Environment, 33, 5053–5070, https://doi.org/10.1016/S1352-2310(99)00251-4, 1999.
6. Carter, W. P. L.: Development of the SAPRC-07 chemical mechanism, Atmospheric Environment, 44, 5324–5335, https://doi.org/10.1016/j.atmosenv.2010.01.026, 2010.
7. Chen, Y., Hall, J., van Wees, D., Andela, N., Hantson, S., Giglio, L., van der Werf, G. R., Morton, D. C., and Randerson, J. T.: Multi-decadal trends and variability in burned area from the fifth version of the Global Fire Emissions Database (GFED5), Earth System Science Data, 15, 5227–5259, https://doi.org/10.5194/essd-15-5227-2023, 2023.
8. Cho, C., Clair, J. M. St., Liao, J., Wolfe, G. M., Jeong, S., Kang, D. il, Choi, J., Shin, M.-H., Park, J., Park, J.-H., Fried, A., Weinheimer, A., Blake, D. R., Diskin, G. S., Ullmann, K., Hall, S. R., Brune, W. H., Hanisco, T. F., and Min, K.-E.: Evolution of formaldehyde (HCHO) in a plume originating from a petrochemical industry and its volatile organic compounds (VOCs) emission rate estimation, Elementa: Science of the Anthropocene, 9, 00015, https://doi.org/10.1525/elementa.2021.00015, 2021.
9. Crawford, J. H., Heald, C. L., Fuelberg, H. E., Morse, D. M., Sachse, G. W., Emmons, L. K., Gille, J. C., Edward, D. P., Deeter, M. N., Chen, G., Olson, J. R., Connors, V. S., Kittaka, C., and Hamlin, A. J.: Relationship between Measurements of Pollution in the Troposphere (MOPITT) and in situ observations of CO based on a large-scale feature

sampled during TRACE-P, Journal of Geophysical Research: Atmospheres, 109, https://doi.org/10.1029/2003JD004308, 2004.
10. Crawford, J. H., Ahn, J.-Y., Al-Saadi, J., Chang, L., Emmons, L. K., Kim, J., Lee, G., Park, J.-H., Park, R. J., Woo, J. H., Song, C.-K., Hong, J.-H., Hong, Y.-D., Lefer, B. L., Lee, M., Lee, T., Kim, S., Min, K.-E., Yum, S. S., Shin, H. J., Kim, Y.-W., Choi, J.-S., Park, J.-S., Szykman, J. J., Long, R. W., Jordan, C. E., Simpson, I. J., Fried, A., Dibb, J. E., Cho, S., and Kim, Y. P.: The Korea–United States Air Quality (KORUS-AQ) field study, Elementa: Science of the Anthropocene, 9, 00163, https://doi.org/10.1525/elementa.2020.00163, 2021.
11. Crippa, M., Solazzo, E., Huang, G., Guizzardi, D., Koffi, E., Muntean, M., Schieberle, C., Friedrich, R., and Janssens-Maenhout, G.: High resolution temporal profiles in the Emissions Database for Global Atmospheric Research, Sci Data, 7, 121, https://doi.org/10.1038/s41597-020-0462-2, 2020.
12. de Gouw, J. A., Gilman, J. B., Kim, S.-W., Lerner, B. M., Isaacman-VanWertz, G., McDonald, B. C., Warneke, C., Kuster, W. C., Lefer, B. L., Griffith, S. M., Dusanter, S., Stevens, P. S., and Stutz, J.: Chemistry of Volatile Organic Compounds in the Los Angeles basin: Nighttime Removal of Alkenes and Determination of Emission Ratios, Journal of Geophysical Research: Atmospheres, 122, 11,843-11,861, https://doi.org/10.1002/2017JD027459, 2017.
13. Eck, T. F., Holben, B. N., Kim, J., Beyersdorf, A. J., Choi, M., Lee, S., Koo, J.-H., Giles, D. M., Schafer, J. S., Sinyuk, A., Peterson, D. A., Reid, J. S., Arola, A., Slutsker, I., Smirnov, A., Sorokin, M., Kraft, J., Crawford, J. H., Anderson, B. E., Thornhill, K. L., Diskin, G., Kim, S.-W., and Park, S.: Influence of cloud, fog, and high relative humidity during pollution transport events in South Korea: Aerosol properties and PM2.5 variability, Atmospheric Environment, 232, 117530, https://doi.org/10.1016/j.atmosenv.2020.117530, 2020.
14. Gaudel, A., Cooper, O. R., Ancellet, G., Barret, B., Boynard, A., Burrows, J. P., Clerbaux, C., Coheur, P.-F., Cuesta, J., Cuevas, E., Doniki, S., Dufour, G., Ebojie, F., Foret, G., Garcia, O., Granados-Muñoz, M. J., Hannigan, J. W., Hase, F., Hassler, B., Huang, G., Hurtmans, D., Jaffe, D., Jones, N., Kalabokas, P., Kerridge, B., Kulawik, S., Latter, B., Leblanc, T., Le Flochmoën, E., Lin, W., Liu, J., Liu, X., Mahieu, E., McClure-Begley, A., Neu, J. L., Osman, M., Palm, M., Petetin, H., Petropavlovskikh, I., Querel, R., Rahpoe, N., Rozanov, A., Schultz, M. G., Schwab, J., Siddans, R., Smale, D., Steinbacher, M., Tanimoto, H., Tarasick, D. W., Thouret, V., Thompson, A. M., Trickl, T., Weatherhead, E., Wespes, C., Worden, H. M., Vigouroux, C., Xu, X., Zeng, G., and Ziemke, J.: Tropospheric Ozone Assessment Report: Present-day distribution and trends of tropospheric ozone relevant to climate and global atmospheric chemistry model evaluation, Elementa: Science of the Anthropocene, 6, 39, https://doi.org/10.1525/elementa.291, 2018.
15. Griffiths, P. T., Murray, L. T., Zeng, G., Shin, Y. M., Abraham, N. L., Archibald, A. T., Deushi, M., Emmons, L. K., Galbally, I. E., Hassler, B., Horowitz, L. W., Keeble, J., Liu, J., Moeini, O., Naik, V., O'Connor, F. M., Oshima, N., Tarasick, D., Tilmes, S., Turnock, S. T., Wild, O., Young, P. J., and Zanis, P.: Tropospheric ozone in CMIP6 simulations, Atmospheric Chemistry and Physics, 21, 4187–4218, https://doi.org/10.5194/acp-21-4187-2021, 2021.

16. Guenther, A. B., Jiang, X., Heald, C. L., Sakulyanontvittaya, T., Duhl, T., Emmons, L. K., and Wang, X.: The Model of Emissions of Gases and Aerosols from Nature version 2.1 (MEGAN2.1): an extended and updated framework for modeling biogenic emissions, Geoscientific Model Development, 5, 1471–1492, https://doi.org/10.5194/gmd-5-1471-2012, 2012.
17. Guo, H., Flynn, C. M., Prather, M. J., Strode, S. A., Steenrod, S. D., Emmons, L., Lacey, F., Lamarque, J.-F., Fiore, A. M., Correa, G., Murray, L. T., Wolfe, G. M., St. Clair, J. M., Kim, M., Crounse, J., Diskin, G., DiGangi, J., Daube, B. C., Commane, R., McKain, K., Peischl, J., Ryerson, T. B., Thompson, C., Hanisco, T. F., Blake, D., Blake, N. J., Apel, E. C., Hornbrook, R. S., Elkins, J. W., Hintsa, E. J., Moore, F. L., and Wofsy, S. C.: Heterogeneity and chemical reactivity of the remote troposphere defined by aircraft measurements – corrected, Atmospheric Chemistry and Physics, 23, 99–117, https://doi.org/10.5194/acp-23-99-2023, 2023.
18. Hall, S. R., Ullmann, K., Prather, M. J., Flynn, C. M., Murray, L. T., Fiore, A. M., Correa, G., Strode, S. A., Steenrod, S. D., Lamarque, J.-F., Guth, J., Josse, B., Flemming, J., Huijnen, V., Abraham, N. L., and Archibald, A. T.: Cloud impacts on photochemistry: building a climatology of photolysis rates from the Atmospheric Tomography mission, Atmospheric Chemistry and Physics, 18, 16809–16828, https://doi.org/10.5194/acp-18-16809-2018, 2018.
19. Heald, C. L., Jacob, D. J., Jones, D. B. A., Palmer, P. I., Logan, J. A., Streets, D. G., Sachse, G. W., Gille, J. C., Hoffman, R. N., and Nehrkorn, T.: Comparative inverse analysis of satellite (MOPITT) and aircraft (TRACE-P) observations to estimate Asian sources of carbon monoxide, Journal of Geophysical Research: Atmospheres, 109, https://doi.org/10.1029/2004JD005185, 2004.
20. Hersbach, H., Bell, B., Berrisford, P., Hirahara, S., Horányi, A., Muñoz-Sabater, J., Nicolas, J., Peubey, C., Radu, R., Schepers, D., Simmons, A., Soci, C., Abdalla, S., Abellan, X., Balsamo, G., Bechtold, P., Biavati, G., Bidlot, J., Bonavita, M., De Chiara, G., Dahlgren, P., Dee, D., Diamantakis, M., Dragani, R., Flemming, J., Forbes, R., Fuentes, M., Geer, A., Haimberger, L., Healy, S., Hogan, R.J., Hólm, E., Janisková, M., Keeley, S., Laloyaux, P., Lopez, P., Lupu, C., Radnoti, G., de Rosnay, P., Rozum, I., Vamborg, F., Villaume, S., Thépaut, J-N.: Complete ERA5 from 1940: Fifth generation of ECMWF atmospheric reanalyses of the global climate. Copernicus Climate Change Service (C3S) Data Store (CDS) [data set], https://doi.org/10.24381/cds.143582cf, 2017.
21. Hersbach, H., Bell, B., Berrisford, P., Biavati, G., Horányi, A., Muñoz Sabater, J., Nicolas, J., Peubey, C., Radu, R., Rozum, I., Schepers, D., Simmons, A., Soci, C., Dee, D., Thépaut, J-N.: ERA5 hourly data on single levels from 1940 to present. Copernicus Climate Change Service (C3S) Climate Data Store (CDS) [data set], https://doi.org/10.24381/cds.adbb2d47, 2023.
22. Hsu, J., Prather, M. J., Wild, O., Sundet, J. K., Isaksen, I. S. A., Browell, E. V., Avery, M. A., and Sachse, G. W.: Are the TRACE-P measurements representative of the western Pacific during March 2001?, Journal of Geophysical Research: Atmospheres, 109, https://doi.org/10.1029/2003JD004002, 2004.
23. Isaksen, I. S. A. and Hov, Ø.: Calculation of trends in the tropospheric concentration of O3, OH, CO, CH4 and NOx | Tellus B: Chemical and Physical Meteorology, https://doi.org/10.3402/tellusb.v39i3.15347, 2022.

24. Jacob, D. J., Crawford, J. H., Kleb, M. M., Connors, V. S., Bendura, R. J., Raper, J. L., Sachse, G. W., Gille, J. C., Emmons, L., and Heald, C. L.: Transport and Chemical Evolution over the Pacific (TRACE-P) aircraft mission: Design, execution, and first results, Journal of Geophysical Research: Atmospheres, 108, https://doi.org/10.1029/2002JD003276, 2003.
25. Jenkin, M. E., Saunders, S. M., and Pilling, M. J.: The tropospheric degradation of volatile organic compounds: a protocol for mechanism development, Atmospheric Environment, 31, 81–104, https://doi.org/10.1016/S1352-2310(96)00105-7, 1997.
26. Jenkin, M. E., Saunders, S. M., Wagner, V., and Pilling, M. J.: Protocol for the development of the Master Chemical Mechanism, MCM v3 (Part B): tropospheric degradation of aromatic volatile organic compounds, Atmospheric Chemistry and Physics, 3, 181–193, https://doi.org/10.5194/acp-3-181-2003, 2003.
27. Jenkin, M. E., Young, J. C., and Rickard, A. R.: The MCM v3.3.1 degradation scheme for isoprene, Atmospheric Chemistry and Physics, 15, 11433–11459, https://doi.org/10.5194/acp-15-11433-2015, 2015.
28. Jia, Y., Yu, G., Gao, Y., He, N., Wang, Q., Jiao, C., and Zuo, Y.: Global inorganic nitrogen dry deposition inferred from ground- and space-based measurements, Sci Rep, 6, 19810, https://doi.org/10.1038/srep19810, 2016.
29. Jung, J., Lee, J., Kim, B., and Oh, S.: Seasonal variations in the NO2 artifact from chemiluminescence measurements with a molybdenum converter at a suburban site in Korea (downwind of the Asian continental outflow) during 2015–2016, Atmospheric Environment, 165, 290–300, https://doi.org/10.1016/j.atmosenv.2017.07.010, 2017.
30. Kim, K.-M., Kim, S.-W., Seo, S., Blake, D. R., Cho, S., Crawford, J. H., Emmons, L. K., Fried, A., Herman, J. R., Hong, J., Jung, J., Pfister, G. G., Weinheimer, A. J., Woo, J.-H., and Zhang, Q.: Sensitivity of the WRF-Chem v4.4 simulations of ozone and formaldehyde and their precursors to multiple bottom-up emission inventories over East Asia during the KORUS-AQ 2016 field campaign, Geoscientific Model Development, 17, 1931–1955, https://doi.org/10.5194/gmd-17-1931-2024, 2024.
31. KORUS-AQ Science Team: KORUS-AQ NASA DC-8 airborne 10 s merged data revision 6 - ICARTT Files, NASA Langley Atmospheric Science Data Center DAAC [data set], https://doi.org/10.5067/Suborbital/KORUSAQ/DATA01, 2019.
32. Lamarque, J.-F., Emmons, L. K., Hess, P. G., Kinnison, D. E., Tilmes, S., Vitt, F., Heald, C. L., Holland, E. A., Lauritzen, P. H., Neu, J., Orlando, J. J., Rasch, P. J., and Tyndall, G. K.: CAM-chem: description and evaluation of interactive atmospheric chemistry in the Community Earth System Model, Geoscientific Model Development, 5, 369–411, https://doi.org/10.5194/gmd-5-369-2012, 2012.
33. Lee, Y. R., Huey, L. G., Tanner, D. J., Takeuchi, M., Qu, H., Liu, X., Ng, N. L., Crawford, J. H., Fried, A., Richter, D., Simpson, I. J., Blake, D. R., Blake, N. J., Meinardi, S., Kim, S., Diskin, G. S., Digangi, J. P., Choi, Y., Pusede, S. E., Wennberg, P. O., Kim, M. J., Crounse, J. D., Teng, A. P., Cohen, R. C., Romer, P. S., Brune, W., Wisthaler, A., Mikoviny, T., Jimenez, J. L., Campuzano-Jost, P., Nault, B. A., Weinheimer, A., Hall, S. R., and Ullmann, K.: An investigation of petrochemical emissions during KORUS-AQ: Ozone production, reactive nitrogen evolution, and aerosol production, Elementa: Science of the Anthropocene, 10, 00079, https://doi.org/10.1525/elementa.2022.00079, 2022.

34. Liang, Q., Jaeglé, L., Hudman, R. C., Turquety, S., Jacob, D. J., Avery, M. A., Browell, E. V., Sachse, G. W., Blake, D. R., Brune, W., Ren, X., Cohen, R. C., Dibb, J. E., Fried, A., Fuelberg, H., Porter, M., Heikes, B. G., Huey, G., Singh, H. B., and Wennberg, P. O.: Summertime influence of Asian pollution in the free troposphere over North America, Journal of Geophysical Research: Atmospheres, 112, https://doi.org/10.1029/2006JD007919, 2007.
35. Lin, X., Trainer, M., and Liu, S. C.: On the nonlinearity of the tropospheric ozone production, Journal of Geophysical Research: Atmospheres, 93, 15879–15888, https://doi.org/10.1029/JD093iD12p15879, 1988.
36. Miyazaki, K., Sekiya, T., Fu, D., Bowman, K. W., Kulawik, S. S., Sudo, K., Walker, T., Kanaya, Y., Takigawa, M., Ogochi, K., Eskes, H., Boersma, K. F., Thompson, A. M., Gaubert, B., Barre, J., and Emmons, L. K.: Balance of Emission and Dynamical Controls on Ozone During the Korea-United States Air Quality Campaign From Multiconstituent Satellite Data Assimilation, Journal of Geophysical Research: Atmospheres, 124, 387–413, https://doi.org/10.1029/2018JD028912, 2019.
37. Nault, B. A., Campuzano-Jost, P., Day, D. A., Schroder, J. C., Anderson, B., Beyersdorf, A. J., Blake, D. R., Brune, W. H., Choi, Y., Corr, C. A., de Gouw, J. A., Dibb, J., DiGangi, J. P., Diskin, G. S., Fried, A., Huey, L. G., Kim, M. J., Knote, C. J., Lamb, K. D., Lee, T., Park, T., Pusede, S. E., Scheuer, E., Thornhill, K. L., Woo, J.-H., and Jimenez, J. L.: Secondary organic aerosol production from local emissions dominates the organic aerosol budget over Seoul, South Korea, during KORUS-AQ, Atmospheric Chemistry and Physics, 18, 17769–17800, https://doi.org/10.5194/acp-18-17769-2018, 2018.
38. Park, R. J., Oak, Y. J., Emmons, L. K., Kim, C.-H., Pfister, G. G., Carmichael, G. R., Saide, P. E., Cho, S.-Y., Kim, S., Woo, J.-H., Crawford, J. H., Gaubert, B., Lee, H.-J., Park, S.-Y., Jo, Y.-J., Gao, M., Tang, B., Stanier, C. O., Shin, S. S., Park, H. Y., Bae, C., and Kim, E.: Multi-model intercomparisons of air quality simulations for the KORUS-AQ campaign, Elementa: Science of the Anthropocene, 9, 00139, https://doi.org/10.1525/elementa.2021.00139, 2021.
39. Peterson, D. A., Hyer, E. J., Han, S.-O., Crawford, J. H., Park, R. J., Holz, R., Kuehn, R. E., Eloranta, E., Knote, C., Jordan, C. E., and Lefer, B. L.: Meteorology influencing springtime air quality, pollution transport, and visibility in Korea, Elementa: Science of the Anthropocene, 7, 57, https://doi.org/10.1525/elementa.395, 2019.
40. Prather, M. J.: Lifetimes and time scales in atmospheric chemistry, Philosophical Transactions of the Royal Society A: Mathematical, Physical and Engineering Sciences, 365, 1705–1726, https://doi.org/10.1098/rsta.2007.2040, 2007.
41. Prather, M. J.: Calibrating the Tropospheric Air and Ozone Mass, AGU Advances, 6, e2025AV001651, https://doi.org/10.1029/2025AV001651, 2025.
42. Prather, M. J. and Jacob, D. J.: A persistent imbalance in HOx and NOx photochemistry of the upper troposphere driven by deep tropical convection, Geophysical Research Letters, 24, 3189–3192, https://doi.org/10.1029/97GL03027, 1997.
43. Prather, M. J. and Zhu, X.: Lifetimes and timescales of tropospheric ozone, Elementa: Science of the Anthropocene, 12, 00112, https://doi.org/10.1525/elementa.2023.00112, 2024.

44. Prather, M. J., Guo, H., and Zhu, X.: Deconstruction of tropospheric chemical reactivity using aircraft measurements: the Atmospheric Tomography Mission (ATom) data, Earth System Science Data, 15, 3299–3349, https://doi.org/10.5194/essd-15-3299-2023, 2023.
45. Saunders, S. M., Jenkin, M. E., Derwent, R. G., and Pilling, M. J.: Protocol for the development of the Master Chemical Mechanism, MCM v3 (Part A): tropospheric degradation of non-aromatic volatile organic compounds, Atmospheric Chemistry and Physics, 3, 161–180, https://doi.org/10.5194/acp-3-161-2003, 2003.
46. Saunois, M., Martinez, A., Poulter, B., Zhang, Z., Raymond, P. A., Regnier, P., Canadell, J. G., Jackson, R. B., Patra, P. K., Bousquet, P., Ciais, P., Dlugokencky, E. J., Lan, X., Allen, G. H., Bastviken, D., Beerling, D. J., Belikov, D. A., Blake, D. R., Castaldi, S., Crippa, M., Deemer, B. R., Dennison, F., Etiope, G., Gedney, N., Höglund-Isaksson, L., Holgerson, M. A., Hopcroft, P. O., Hugelius, G., Ito, A., Jain, A. K., Janardanan, R., Johnson, M. S., Kleinen, T., Krummel, P. B., Lauerwald, R., Li, T., Liu, X., McDonald, K. C., Melton, J. R., Mühle, J., Müller, J., Murguia-Flores, F., Niwa, Y., Noce, S., Pan, S., Parker, R. J., Peng, C., Ramonet, M., Riley, W. J., Rocher-Ros, G., Rosentreter, J. A., Sasakawa, M., Segers, A., Smith, S. J., Stanley, E. H., Thanwerdas, J., Tian, H., Tsuruta, A., Tubiello, F. N., Weber, T. S., van der Werf, G. R., Worthy, D. E. J., Xi, Y., Yoshida, Y., Zhang, W., Zheng, B., Zhu, Q., Zhu, Q., and Zhuang, Q.: Global Methane Budget 2000–2020, Earth System Science Data, 17, 1873–1958, https://doi.org/10.5194/essd-17-1873-2025, 2025.
47. Schroeder, J. R., Crawford, J. H., Ahn, J.-Y., Chang, L., Fried, A., Walega, J., Weinheimer, A., Montzka, D. D., Hall, S. R., Ullmann, K., Wisthaler, A., Mikoviny, T., Chen, G., Blake, D. R., Blake, N. J., Hughes, S. C., Meinardi, S., Diskin, G., Digangi, J. P., Choi, Y., Pusede, S. E., Huey, G. L., Tanner, D. J., Kim, M., and Wennberg, P.: Observation-based modeling of ozone chemistry in the Seoul metropolitan area during the Korea-United States Air Quality Study (KORUS-AQ), Elementa: Science of the Anthropocene, 8, 3, https://doi.org/10.1525/elementa.400, 2020.
48. Simpson, D., Tuovinen, J.-P., Emberson, L., and Ashmore, M. R.: Characteristics of an Ozone Deposition Module, Water, Air, & Soil Pollution: Focus, 1, 253–262, https://doi.org/10.1023/A:1013127826769, 2001.
49. Sindelarova, K., Granier, C., Bouarar, I., Guenther, A., Tilmes, S., Stavrakou, T., Müller, J.-F., Kuhn, U., Stefani, P., and Knorr, W.: Global data set of biogenic VOC emissions calculated by the MEGAN model over the last 30 years, Atmospheric Chemistry and Physics, 14, 9317–9341, https://doi.org/10.5194/acp-14-9317-2014, 2014.
50. Stevenson, D. S., Zhao, A., Naik, V., O'Connor, F. M., Tilmes, S., Zeng, G., Murray, L. T., Collins, W. J., Griffiths, P. T., Shim, S., Horowitz, L. W., Sentman, L. T., and Emmons, L.: Trends in global tropospheric hydroxyl radical and methane lifetime since 1850 from AerChemMIP, Atmospheric Chemistry and Physics, 20, 12905–12920, https://doi.org/10.5194/acp-20-12905-2020, 2020.
51. Talukdar, R. K., Burkholder, J. B., Schmoltner, A.-M., Roberts, J. M., Wilson, R. R., and Ravishankara, A. R.: Investigation of the loss processes for peroxyacetyl nitrate in the atmosphere: UV photolysis and reaction with OH, Journal of Geophysical Research: Atmospheres, 100, 14163–14173, https://doi.org/10.1029/95JD00545, 1995.
52. Thompson, C. R., Wofsy, S. C., Prather, M. J., Newman, P. A., Hanisco, T. F., Ryerson, T. B., Fahey, D. W., Apel, E. C., Brock, C. A., Brune, W. H., Froyd, K., Katich, J. M., Nicely, J. M., Peischl, J., Ray, E., Veres, P. R., Wang, S., Allen, H. M., Asher, E., Bian,

H., Blake, D., Bourgeois, I., Budney, J., Bui, T. P., Butler, A., Campuzano-Jost, P., Chang, C., Chin, M., Commane, R., Correa, G., Crounse, J. D., Daube, B., Dibb, J. E., DiGangi, J. P., Diskin, G. S., Dollner, M., Elkins, J. W., Fiore, A. M., Flynn, C. M., Guo, H., Hall, S. R., Hannun, R. A., Hills, A., Hintsa, E. J., Hodzic, A., Hornbrook, R. S., Huey, L. G., Jimenez, J. L., Keeling, R. F., Kim, M. J., Kupc, A., Lacey, F., Lait, L. R., Lamarque, J.-F., Liu, J., McKain, K., Meinardi, S., Miller, D. O., Montzka, S. A., Moore, F. L., Morgan, E. J., Murphy, D. M., Murray, L. T., Nault, B. A., Neuman, J. A., Nguyen, L., Gonzalez, Y., Rollins, A., Rosenlof, K., Sargent, M., Schill, G., Schwarz, J. P., Clair, J. M. S., Steenrod, S. D., Stephens, B. B., Strahan, S. E., Strode, S. A., Sweeney, C., Thames, A. B., Ullmann, K., Wagner, N., Weber, R., Weinzierl, B., Wennberg, P. O., Williamson, C. J., Wolfe, G. M., and Zeng, L.: The NASA Atmospheric Tomography (ATom) Mission: Imaging the Chemistry of the Global Atmosphere, https://doi.org/10.1175/BAMS-D-20-0315.1, 2022.

53. Wild, O., Prather, M. J., Akimoto, H., Sundet, J. K., Isaksen, I. S. A., Crawford, J. H., Davis, D. D., Avery, M. A., Kondo, Y., Sachse, G. W., and Sandholm, S. T.: Chemical transport model ozone simulations for spring 2001 over the western Pacific: Regional ozone production and its global impacts, Journal of Geophysical Research: Atmospheres, 109, https://doi.org/10.1029/2003JD004041, 2004.
54. Wilson, C. P. and Prather, M. J.: Gridded surface O3, NOx, and CO abundances for model metrics from the South Korean ground station network, Atmospheric Measurement Techniques, 18, 1757–1769, https://doi.org/10.5194/amt-18-1757-2025, 2025.
55. Wilson, C.: Modelling system for computing the tropospheric O3 and CH4 perturbations from South Korean Emissions (KORUS-AQ period), Dryad [code], https://doi.org/10.5061/dryad.f4qrfj78x, 2025.
56. Wolfe, G. M., Marvin, M. R., Roberts, S. J., Travis, K. R., and Liao, J.: The Framework for 0-D Atmospheric Modeling (F0AM) v3.1, Geosci. Model Dev., 9, 3309–3319, https://doi.org/10.5194/gmd-9-3309-2016, 2016.
57. Woo, J.-H., Kim, Y., Kim, H.-K., Choi, K.-C., Eum, J.-H., Lee, J.-B., Lim, J.-H., Kim, J., and Seong, M.: Development of the CREATE Inventory in Support of Integrated Climate and Air Quality Modeling for Asia, Sustainability, 12, 7930, https://doi.org/10.3390/su12197930, 2020.
58. Yan, C., Tham, Y. J., Zha, Q., Wang, X., Xue, L., Dai, J., Wang, Z., and Wang, T.: Fast heterogeneous loss of N2O5 leads to significant nighttime NOx removal and nitrate aerosol formation at a coastal background environment of southern China, Science of The Total Environment, 677, 637–647, https://doi.org/10.1016/j.scitotenv.2019.04.389, 2019.
59. Zhang, L., Brook, J. R., and Vet, R.: On ozone dry deposition—with emphasis on non-stomatal uptake and wet canopies, Atmospheric Environment, 36, 4787–4799, https://doi.org/10.1016/S1352-2310(02)00567-8, 2002.
60. Zhang, L., Vet, R., O'Brien, J. M., Mihele, C., Liang, Z., and Wiebe, A.: Dry deposition of individual nitrogen species at eight Canadian rural sites, Journal of Geophysical Research: Atmospheres, 114, https://doi.org/10.1029/2008JD010640, 2009.
61. Zhuang, J., Jacob, D. J., and Eastham, S. D.: The importance of vertical resolution in the free troposphere for modeling intercontinental plumes, Atmospheric Chemistry and Physics, 18, 6039–6055, https://doi.org/10.5194/acp-18-6039-2018, 2018.

62. Ziemke, J. R., Oman, L. D., Strode, S. A., Douglass, A. R., Olsen, M. A., McPeters, R. D., Bhartia, P. K., Froidevaux, L., Labow, G. J., Witte, J. C., Thompson, A. M., Haffner, D. P., Kramarova, N. A., Frith, S. M., Huang, L.-K., Jaross, G. R., Seftor, C. J., Deland, M. T., and Taylor, S. L.: Trends in global tropospheric ozone inferred from a composite record of TOMS/OMI/MLS/OMPS satellite measurements and the MERRA-2 GMI simulation, Atmospheric Chemistry and Physics, 19, 3257–3269, https://doi.org/10.5194/acp-19-3257-2019, 2019.

Chapter 4: Impact of urban-industrial air pollution on chemically reactive greenhouse gases is highly sensitive to organic nitrate formation

Calum P. Wilson[1] and Michael J. Prather[1]

[1]Department of Earth System Science, University of California, Irvine, Irvine, 92697, United States of America

Correspondence to: Calum P. Wilson (calumw@uci.edu)

Abstract.

We compute net tropospheric ozone production (P-O_3) and methane oxidation (L-CH_4) caused by 45 days of South Korean emissions using a chemistry-transport model (CTM) and a hybrid modelling system (HMS). The CTM has global 1° x 1° resolution; the HMS has detailed chemical mechanisms and a refined regional grid (0.1° x 0.1°), but simplified, staged transport. The emissions cause +22.1 Gmol P-O_3 and +2.0 Gmol L-CH_4 in the CTM *vs*. +31.2 Gmol P-O_3 and +4.3 Gmol L-CH_4 in the HMS. Differences are attributed to lower volatile organic compound (VOC) reactivity in the CTM, thus decreased organic nitrate export to the free troposphere. Time-integrated O_3 mass perturbations (δO_3) are similar in both models and constitute a globally-averaged +0.03 DU summertime O_3 enhancement. Due to contrasting L-CH_4, the net steady-state effective radiative forcing sustained by the emissions is +0.49 mW m^{-2} in the CTM and -0.25 mW m^{-2} in the HMS.

1 Introduction

Tropospheric ozone (O_3) and methane (CH_4) are short-lived greenhouse gases whose atmospheric abundances have risen since the preindustrial era (Szopa *et al*., 2023). Methane growth has been driven primarily by fossil fuel and agricultural emissions (Saunois *et al*., 2025), likely offset by growth in the main CH_4 sink, the hydroxyl radical (OH) (Isaksen and Hov, 1986; Stevenson *et al*., 2020). Ozone is both produced and destroyed through atmospheric chemistry.

Ozone growth since the 1980s is attributed to intensified precursor emissions including nitrogen oxides (NO_x), carbon monoxide (CO), and volatile organic compounds (VOCs), which are driven by industrialisation, most recently across Asia (Gaudel *et al*., 2018; Ziemke *et al*., 2019). In this work, we investigate the global CH_4 and O_3 perturbations caused by anthropogenic air pollution from South Korea using a global chemistry-transport model (CTM), and compare the results with those from a regional, hybrid modelling system (HMS; Wilson and Prather, 2026) with refined horizontal resolution and highly detailed chemical mechanisms.

Greenhouse gas budgets for O_3 and CH_4 are sensitive to the distribution of polluted air in the free troposphere (Guo *et al*., 2023). Chemistry-transport models are effective tools for computing CH_4 and O_3 budgets in response to pollution because they seamlessly integrate the transport and chemistry of the emissions. However, the computational cost of global-scale modelling requires model compromises such as simplified chemical mechanisms and coarsened spatial resolution. Our work with the HMS addressed these issues via a regional study limited to South Korea with refined boundary-layer horizontal resolution and a nearly complete set of chemical reactions. Pollution plumes transported beyond the model domain were treated in a subsequent box modelling stage, after which residual pollutants were linearly dispersed. This approach captured the budget terms over the full lifespan of the emissions, but introduced discontinuities between the modelling stages and did not simulate plume trajectories beyond South Korea.

We use a standard UC Irvine CTM simulation (Prather, 2024; Prather and Zhu, 2024; Prather, 2025) with an added 45-day South Korean emission perturbation at the 10% level of anthropogenic emissions used in the HMS work. We accumulate the total loss of CH_4 (L-CH_4, Gmol) from those added emissions as well as the integrated O_3 perturbation (Gmol days). Deriving total net production of O_3 (P-O_3, Gmol) from the O_3 perturbation (Gmol days) requires

knowledge of the O_3 lifetime (days), which varies from 6 to 26 days based on altitude and season (Prather and Zhu, 2024). We calculate these lifetimes for the Pacific troposphere by simulating the decay of artificial O_3 releases from four vertically stacked boxes downwind of South Korea in May.

We discuss the modelling parameters and O_3 lifetime determination in Section 2, derive the budgets and radiative forcings in Section 3, and present our findings in Section 4.

2 Methodology

2.1 Chemistry-transport modelling

The control CTM run uses the same meteorology, chemical mechanisms, and emission inventories as described in Prather (2025). The run consists of a 92-day study period 01 May to 01 August (midnight UTC) using the available meteorology for year 2000 and fully spun up initial conditions for 01 May 2000. The control inventories include the MEGAN-MACC biogenic emissions (Sindelarova *et al*., 2014; Guenther *et al*., 2012) and CMIP6 emissions for anthropogenic, biofuel, and biomass burning (Hoesly *et al.*, 2018) for the following species: carbon monoxide (CO), nitric oxide (NO), ethane (C_2H_6), 'alkane' (propane and higher alkanes), 'alkene' (ethene and higher alkenes), formaldehyde (HCHO), acetaldehyde (CH_3CHO), acetone (CH_3COCH_3), and isoprene (C_5H_8). Lightning NO emissions are also included. The CTM tropospheric chemical mechanism includes 24 species and 86 reactions in addition to dry deposition and washout.

The emission run includes the KORUS v5 anthropogenic (Woo *et al.*, 2020) and GFED5 biomass burning (Chen *et al.*, 2023) inventories used in the HMS. These emissions are converted from SAPRC format (Carter, 2010) to CTM species (see Table 1). Lumped SAPRC species are each assigned a single molecular weight based on the most abundant component (see Wilson and

Prather, 2026) and converted from mol s^{-1} to kg m^{-2} s^{-1} units. Aromatic species (ARO1 and ARO2) are not included in the CTM chemistry, but here we add these into the 'Alkene' emission category as they generally oxidise to form alkenyl products. The 45-day "KORUS-AQ" emission period follows the timeframe of the Korea-US Air Quality mission from 01 May to 14 June (midnight UTC) and is followed by a spin-down period for the remaining 47 days simulated in the control run. After day 92, we have reached about 97% of the total chemical impact of the emission period and can easily extrapolate the residual chemical perturbations driven by long-lived CO chemistry.

Table 4.1: *The mapping of KORUS v5 and GFED5 emission inventories (01 May - 15 June) to UCI CTM species.*

UCI CTM surrogate species	**SAPRC emitted species (MCM surrogates)**	**CTM cumulative emissions (kt)**
NO	NO	92
NO_2	NO_2	19
CO	CO	205
Isoprene	Isoprene	0.5
MVKMACR	Methyl vinyl ketone Methacrolein Total	0.0 0.0 0.5
Formaldehyde	Formaldehyde	1.1
Acetaldehyde	Acetaldehyde Glyoxal Methylglyoxal Benzaldehyde Diacetyl RCHO (Propanaldehyde) Total	0.6 0.2 0.1 0.0 0.0 0.3 1.2
Ethane	ALK1 (Ethane)	3.7
Alkane	ALK2 (Propane) ALK3 (Butanes) ALK4 (3/4 Pentanes + 1/4 Hexanes) ALK5 (Heptanes) Acetone Methyl ethyl ketone Total	4.8 3.3 10.5 15.1 0.4 0.6 34.7
Alkene	Ethene OLE1 (Propene) OLE2 (1,3-Butadiene) ARO1 (1/3 Benzene + 2/3 Toluene) ARO2 (2/3 Xylenes + 1/3 Trimethylbenzenes) Total	8.3 4.1 5.5 34.4 18.3 70.6

KORUS v5 emissions (Woo et al., 2020) were converted from mol s^{-1} emissions to kg m^{-2} s^{-1} emissions. Moles are converted to mass using the molecular weights of the emitted species, and emissions are re-gridded to 0.5°x0.5° in CMIP6 format for the CTM. Lumped SAPRC species are represented in the HMS by MCM surrogates (parenthesised), whose molecular masses are used in the CTM unit conversion. Emissions from oceanic grid cells in the 0.1°x0.1° HMS model are not included in the Wilson and Prather (2026) calculations, nor the CTM calculations here.

2.2 Hybrid modelling system

The goal of the HMS is to simulate the full life cycle of the KORUS-AQ air pollution emissions, with best available chemical mechanisms from MCM v3.3.1 (Bloss et al., 2005; Jenkin et al., 1997; Jenkin et al., 2003; Jenkin et al., 2015; Saunders et al., 2003) while tracking the resulting CH_4 and O_3 budget perturbations. The HMS consists of three separate stages that emulate the chemical evolution of pollution instead of the continuous chemistry and 3D transport afforded by the CTM. As described in Wilson and Prather (2026), "the boundary layer-residual layer (BL-RL) stage processes the emissions, photochemistry, deposition, aerosol reactivity, and transport over terrestrial South Korea at 0.1°×0.1° with hourly resolution. The plume (PL) stage continues to integrate the chemistry of air masses from the BL-RL stage as they are transported offshore, simulating offshore pollution plumes observed by aircraft. After three days of chemical aging in non-diluting plumes, the pollution remnants are dispersed (DP stage) into the background atmosphere and integrated until the pollution disappears." Ozone lifetimes in the HMS are computed for a four-layer (2, 4, 6, and 8 km), statically maintained background atmosphere composition constrained by observations from the Atmospheric Tomography mission (ATom).

2.3 Structural model differences

Structural differences between the two models inevitably bias the budgets with respect to one another. For example, the CTM mixes emissions into 10,000 km^2 grid cells *vs*. 100 km^2 in HMS, thereby missing the extreme non-linear chemistry near source regions. Emitting NO_x pollution over larger areas reduces NO_x saturation and O_3 titration (Zakoura and Pandis, 2018; Li *et al.*, 2023) and increases the NO_x-efficiency of P-O_3 and L-CH_4 (Charlton-Perez *et al.*, 2009; Wild *et al*., 2004). The CTM continuously dilutes pollution plumes through resolved divergent flow and other unresolved mixing. In contrast, pollution plumes in the HMS remain isolated in the free

troposphere for 0-3 days before they are instantly mixed into the background. The varying atmospheric conditions that drive chemistry downwind of the boundary layer (*i.e.* temperature, pressure, water vapor, J-values) are not resolved in the HMS.

The chemistry in the UCI CTM lacks aromatic mechanisms and does not accurately represent higher-mass VOCs and their diverse oxidised intermediates. The only fast-reacting VOC in the CTM is the alkene species (C_2H_4), used as a surrogate for all alkene and aromatic emissions. Thus, the CTM underrepresents VOC-OH reactivity and O_3 production, thereby sustaining NO_x-saturated conditions at lower NO_x abundance. Another consequence of reduced VOC reactivity is much lower production of organic nitrates (Fischer *et al*., 2014), represented in the CTM only by peroxyacetyl nitrate (PAN). The HMS includes 94 additional peroxyacyl nitrate species, 340 alkyl nitrates, and 57 aromatic nitrates. Organic nitrates sequester NO_x and deliver it to the remote troposphere where it is more effective at increasing P-O_3 and L-CH_4 (Singh, 1987; Hudman *et al*., 2004; Fischer *et al.*, 2010).

We compare probability distributions of vertical profiles (lower, median, and upper quartiles) from the control CTM run with *in situ* observations from the 10 s merge DC-8 KORUS-AQ data (KORUS-AQ Science Team, 2019) alongside the HMS boundary layer data (Fig. 1). At each CTM level, quantiles are extracted from 45 daily average values over the 6 CTM grid cells that lie predominantly over South Korea (126.5°E-129.8°E and 34.8°N-38.1°N). The HMS boundary-layer data comprises 45x24 instantaneous hourly data points for 1092 terrestrial grid-cells. The quantiles extracted from this data are mass-weighted to account for fluctuations in boundary-layer height. Aircraft quantiles are computed from all South Korean data (55,696 flight segments) within separate vertical bins matching the CTM edge-level pressures. The models and observations show good agreement on NO_x and O_3. Ozone disagreement near the surface is

explained by daytime-only sampling by the aircraft, positively biasing the observations below 2 km (see Fig. 6 from Crawford *et al*., 2021). Both models underestimate CO, HCHO, CH_3CHO, and PAN, as did other modelling studies (*e.g.*, supplement from Oak *et al.*, 2019; Table 4 from Kim *et al.*, 2024). Model underestimates are more pronounced in the CTM, where HCHO, CH_3CHO, and PAN in the lowest 2 km are lower than observations by a factor of 2. This is indicative of underestimated VOC reactivity, which reduces PAN abundance due to feedbacks on O_3 and NO_2 (Fischer et al., 2014). Differences between HMS and CTM also reflect the HMS choice of clean-air background that excludes the influence of transboundary air pollution on South Korea (Miyazaki *et al.*, 2019; Kim *et al.*, 2024).

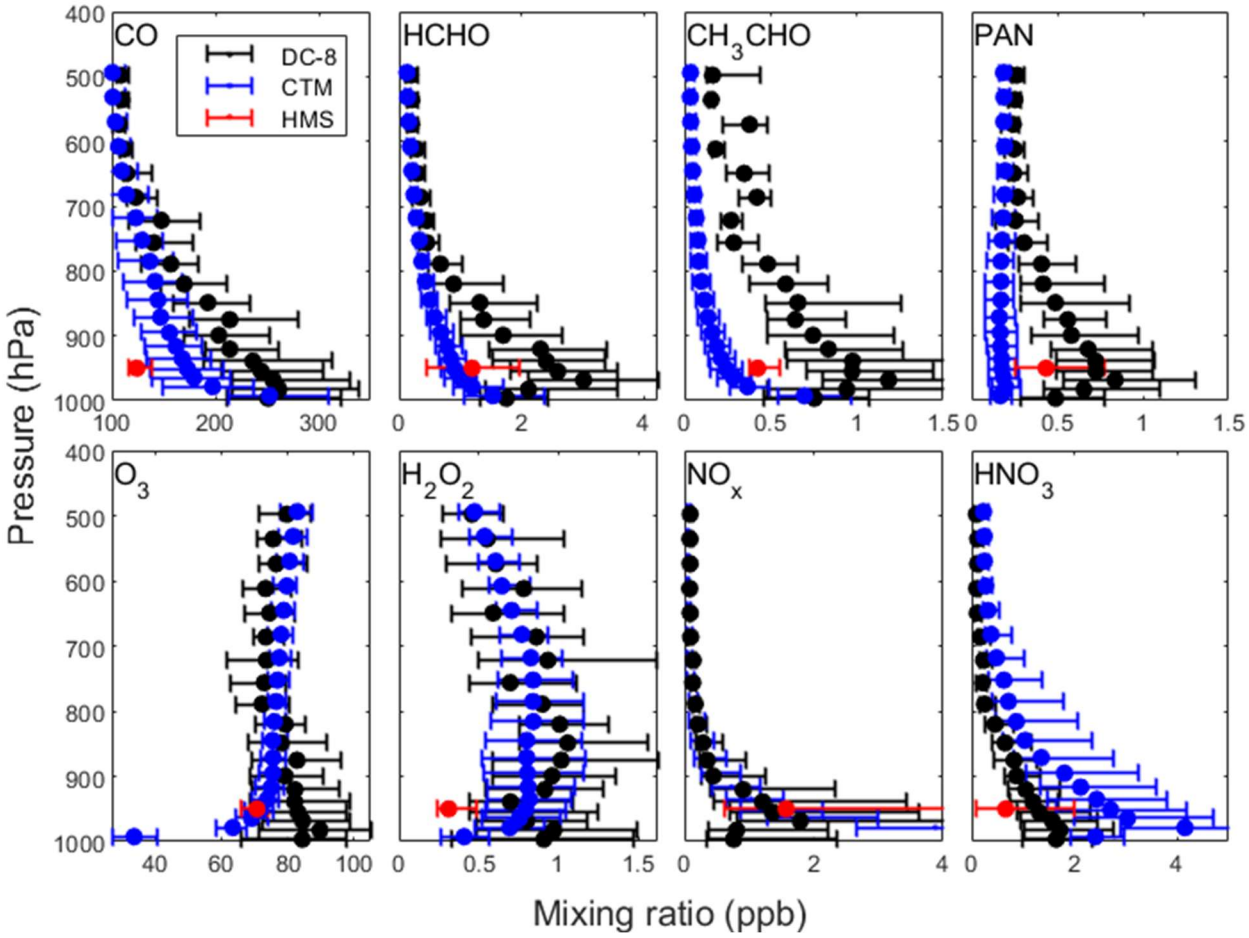

Figure 4.1: *Vertical profiles of observed (black) and CTM (blue) mole fractions with HMS boundary-layer data.*

Dots are medians and horizontal bars are lower and upper quartiles KORUS-AQ in situ DC-8 data were sampled from 08:00 to 18:00 UTC+09 between the mean edge-level pressures of the CTM on 21 flight days over South Korea (see Figure 3 from Crawford et al., 2021). Model data (CTM: daily diurnal averages; HMS: hourly) are sampled every day from 01 May to 15 June starting 00:00 UTC (HMS: 15:00 UTC) in a box from 126.5°E-129.8°E and 34.8°N-38.1°N.

2.4 Ozone lifetime in the CTM

We estimate the perturbation lifetime of tropospheric O_3 in a broad box (29.2-49.3°N, 128.8-149.1°E) enveloping the region of largest O_3 perturbations in the CTM. The box is vertically partitioned into four pressure intervals by level number: 1000-800 hPa (L1-10), 800-600 hPa (L11-16), 600-400 hPa (L17-21), and 400-300 hPa (L22-24). Beginning 01 May 2000 at 00:00 UTC, we release a 'puff' of O_3 into each vertical box partition, adding +10% O_3 mass to each

constituent 3D cell. We integrate 61 days of chemistry-transport against a control run. The O_3 lifetime in each vertical partition is computed from the time-integral of the O_3 mass perturbation divided by the initial perturbation mass. The tail of the O_3 decay beyond 61 days is extrapolated by a least-squares exponential fit using the last 10 days of data. The O_3 lifetimes in the four partitions (lowest to highest altitude) are 11.4, 13.7, 15.9, and 19.1 days. After 20 days, the CTM O_3 perturbations at all levels decay with an e-fold of around 13 days (see Fig. 2) as expected from vertical mixing rates in the troposphere (Prather 2025). These CTM lifetimes contain the feedbacks from chemistry and transport, whereas the lifetimes in the HMS, 5.8, 10.8, 17.9, and 24.2 days, were computed at fixed altitudes of 2 km, 4 km, 6 km, and 8 km without intermixing.

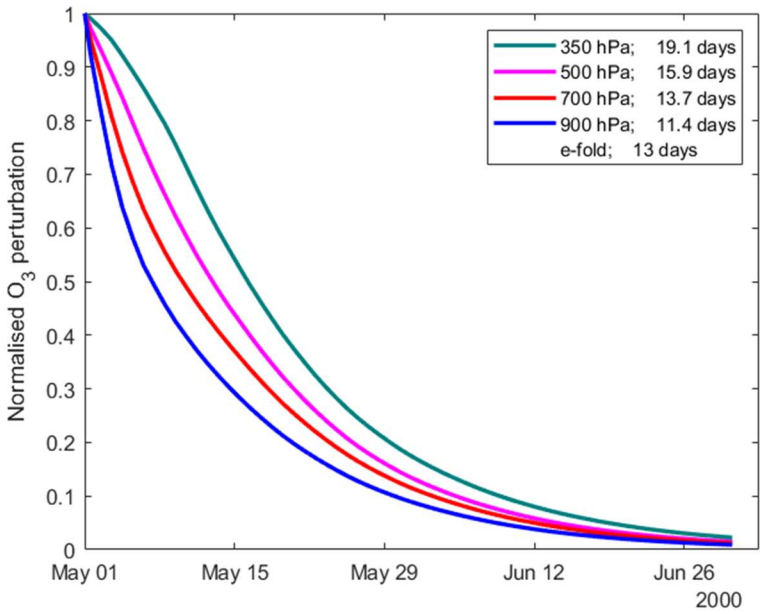

Figure 4.2: *The decay of four CTM ozone releases at 1000-800 hPa (blue), 800-600 hPa (red), 600-400 hPa (magenta), and 400-300 hPa (green).*

Perturbations are normalised to the initial O_3 release. Ozone perturbations are diagnosed daily as diurnally averaged (between 00:00 UTC) grid-box masses and spatially integrated to obtain the perturbation lifetimes (legend). The area under each curve is the perturbation lifetime. The long-term unified decay-lifetime is around 13 days.

3 Results and discussion

The total pollution-driven changes in O_3 and CH_4 from the CTM and HMS can be directly compared, but the individual modelling stages of the HMS do not have a direct CTM analogue. The CTM can approximately emulate the BL-RL stage by integrating L-CH_4 and the O_3 perturbations (δO_3; Gmol day) in a box containing grid cells in the South Korean boundary layer (33°-39°N, 125-131°E, and layers 1-8, *i.e.*, >860 hPa). Boundary-layer (BL) pollution in the CTM disperses without a clear distinction between plumes (PL) and dispersed pollution (DP) as in the HMS. We define a PL box containing plumes in the CTM that extends the BL-RL box by 5° upwind to the West, 10° in the other directions, and from surface to 600 hPa. A distance of 10° represents about one day of transport at 10 m s^{-1}. The CTM BL box is embedded within this PL box and subtracted from the PL box budgets. The DP domain is the global atmosphere, subtracting the BL and PL budgets. These domains, and the CTM budget perturbations, are illustrated in Fig. 3.

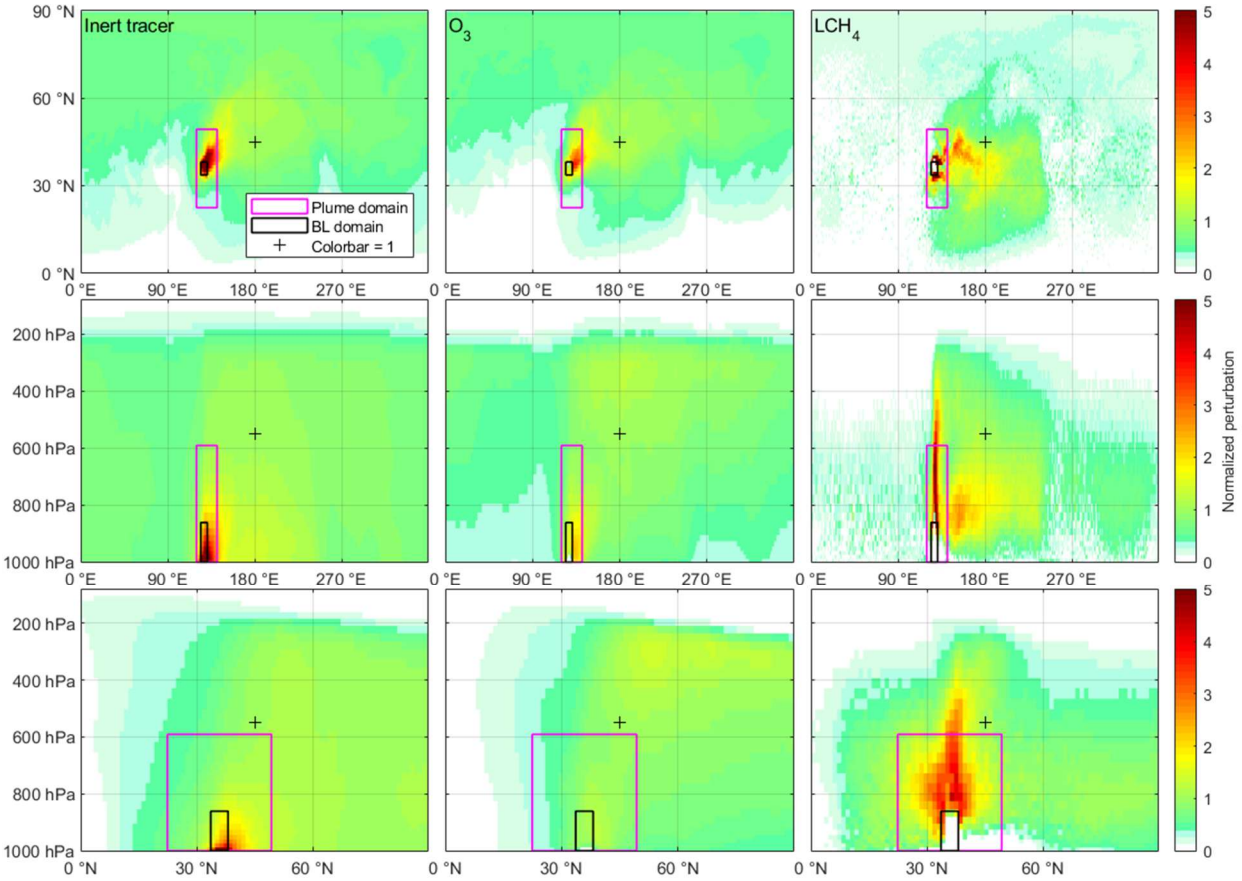

Figure 4.3: *Time-integrated inert tracer abundance (left), integrated O_3 perturbation (middle), and CH_4 loss (L-CH4; right) over 92 days from the start of emissions.*

Inert tracer is emitted with a NO_x pattern over the 45-day emission period. Data are column densities (top) or mole fractions (centre and bottom) averaged over all latitudes (middle) or all longitudes (bottom). Prior to normalisation, inert tracer and O_3 data have units of mol m^{-2} day (top) and mol mol^{-1} day (middle and bottom), and L-CH_4 data have units of mol m^{-2} (top) and mol mol^{-1} (middle and bottom). All data are normalised to one at the map centre (+). Negative perturbations, i.e. in the Korean boundary-layer (black box) and plume region (purple box), are not shown.

3.1 Budgets

Table 2 shows the CTM and HMS budget terms (δO_3, P-O_3 and L-CH_4). The δO_3 mass perturbations are similar in both models and constitute a near steady-state +0.03 DU global O_3 enhancement during the 45-day emission period. The CTM P-O_3 is, however, only 71% that of the HMS (+22.2 *vs*. +31.2 Gmol) because the lifetime of an O_3 perturbation in the CTM is longer. The CTM CH_4 loss (L-CH_4) is also smaller at 47% that of HMS (+2.0 *vs*. +4.3 Gmol). The HMS calculation is based on 3-day aging for the PL stage before dispersion; if we assume 1-

day plumes, the model discrepancies widen by about 10 percentage points (see Table 2). With 1-day plumes, the partitioning of L-CH_4 between PL and DP stages is similar in both models and likely reflects the size of PL diagnostic box in the CTM, which is based on one-day of transport distance. The dilution of emissions into coarser CTM grid-cells should nominally raise P-O_3 and L-CH_4 over the fine-grid HMS (*e.g.*, Charlton-Perez *et al.*, 2009; Holmes *et al.*, 2014), but our results show the opposite. We attribute this to the very different VOC mechanisms.

To compare the atmospheric compositions in the models, we examine the CTM control run (without the 10% added KORUS emissions) and the HMS pollution run, both of which simulate full South Korean emissions. The OH mole fraction in the entire BL domain, sampled over the first 10 days, is 0.06 ppt in the CTM *vs*. 0.11 ppt in the HMS. This is, once again, unexpected because mixing pollution over the coarse-grid CTM should raise OH (Li *et al.*, 2023). The HO_2 mole fraction (the dominant component of $HO_x = HO_2 + OH$) is similar in both models (4.2 *vs.* 4.4 ppt, respectively) with about the same overall loss frequency (1/49 *vs.* 1/56 s^{-1}) for radical-radical termination (*i.e.*, excluding OH-VOC reactions). However, the dominant termination reaction in the CTM is H_2O_2 formation, whereas in the HMS, it is HNO_3 formation.

As the pollution plumes age after leaving the BL, NO_x decays faster than VOCs, and ozone production efficiency rises (OPE = moles of O_3 produced per moles of HNO_3 formed; Liu *et al.*, 1987). In the HMS, the greatest, but not the most efficient, daily O_3 production is driven by the intense NO_x-VOC chemistry on day 1 of the PL stage (+8.0 Gmol at 7.6 OPE). Days 2 and 3 produce a combined +8.3 Gmol O_3 at 19.9 and 20.9 respective OPEs. At this stage, most of the reactive NO_x comes from organic nitrate decomposition. After day 3, in the DP stage, the dispersed plumes produce +10.9 Gmol O_3, at 27.8 OPE (NO_x alone) or 35.3 OPE (all pollution). The OPE over the full emission lifespan is 8.9. Over the combined PL and DP domains of the

CTM, the OPE is 17.1, and over the full pollution lifespan, it is 6.3. The lower total OPE of the CTM is explained by the NO_x budget. Both models emit a total of 3.51 Gmol NO_x to the BL over 45 days. Of these emissions, the HMS exports 1.27 Gmol NO_x plus 0.47 Gmol organic nitrates (including 0.25 Gmol PAN) to the PL stage as plumes. The PL NO_x then decays to 0.08 Gmol by end of day 1 while organic nitrates increase to 0.60 Gmol (0.39 Gmol PAN). The CTM, on the other hand, exports 1.17 Gmol NO_x and just 0.08 Gmol PAN to the PL domain. The CTM pollution exiting the PL domain contains 0.22 Gmol NO_x and 0.12 Gmol PAN. The low yield of PAN in the CTM greatly reduces the amount of NO_x that reaches the clean, higher OPE environment. A study of US NO_x pollution during July computed a total OPE of 7 in the global troposphere (Jacob *et al*., 1993) which intermediates our CTM and HMS values. High PAN abundance in the boundary-layer was a noted problem in the US study, in contrast with the low PAN over South Korea (see Figure 1).

We analyse L-CH_4 by defining methane destruction efficiency similarly to OPE (MDE = moles of CH_4 lost per moles of HNO_3 formed; Holmes *et al.*, 2014). In the HMS, the total MDE is 1.2 over the whole model. The MDEs in the individual model stages are: 0.2 in the BL; 0.5, 2.4, and 3.5 on days 1-3 of PL aging; and 10.0 (NO_x alone) in the DP stage, or 7.3 (all pollution). In the CTM, the overall MDE is 0.6, with negative MDE in the BL (-0.1), 0.2 MDE in the PL, and 9.1 MDE in the DP domain. The overall range of MDEs is similar to that of the HMS. We once again attribute the low L-CH_4 in the CTM *vs*. HMS to low organic nitrate yield.

Compared with a maritime shipping plume study (Holmes *et al.*, 2014), the HMS OPEs and MDEs are similar. In fresh shipping plumes (<0.5 day-aged), the respective OPEs and MDEs are 1.7 and 0.4; and globally, they are 8.5 and 3.1. Overall, our MDEs are lower because the CO:NO_x ratio of South Korean emissions is 10 times greater than that of the shipping emissions

in Holmes *et al*. (2014). The efficiency terms are defined with respect to NO_x loss; however, the O_3 and OH chemistry is sensitive to the co-emitted VOC and CO pollution.

Table 4.2: *Methane and ozone budgets from the KORUS-AQ period of emissions.*

Time-integrated diagnostics	**CTM**				**HMS: 3 days (1 day) plume aging**			
	Total	**BL box**	**PL box**	**DP region**	**Total**	**BL-RL**	**PL**	**DP**
L-CH_4 (Gmol)	+2.0	-0.2	+0.2	+2.0	+4.3 (+5.8)	+0.3	+1.7 (+0.5)	+2.3 (+5.0)
P-O_x (Gmol)	+21.4	+3.0	+6.6	+11.8	N/A	N/A	N/A	N/A
L-O_x (Gmol)	+15.1	+0.0	+1.5	+13.6	N/A	N/A	N/A	N/A
δO_3 (Gmol days)	+327	+1	+14	+312	+320 (+389)	+2	+34 (+8)	+284 (+379)
P-O_3 (Gmol)	+22.2	+0.1	+22.1		+31.2 (+35.8)	+4.0	+16.3 (+8.0)	+10.9 (+23.8)
OPE	6.3	0.0	17.7		8.9 (10.2)	2.3	11.2 (7.6)	27.8
MDE	0.6	-0.1	0.2	9.1	1.2 (1.7)	0.2	1.2 (0.4)	10.0

UCI-CTM diagnostics were calculated for a 10% KORUS-AQ emission perturbation (KORUS v5 + GFED5) in a 6°x6° degree box (100 km resolution), scaled to 100% by a factor of 10. The hybrid modelling system diagnostics were calculated for a 100% perturbation of the same emissions, but at 10 km resolution. The UCI-CTM model was run for 45 emission days + 47 spin-down days, after which the residuals were extrapolated via a least-squares exponential fit. In the CTM, the 'BL' (33°-39°N, 125-131°E, >860 hPa), 'PL' (23°-49°N, 120-141°E, 860-600 hPa), and 'dispersed' (global excluding 'BL' and 'plume' boxes) domains are spatial regions. In the hybrid model, these domains are separate modelling stages featuring chemistry, emissions, and transport in the terrestrial South Korean boundary layer and residual layer (BL), chemical integration on plumes transported offshore (PL), and dilute linearised chemistry of three-day-aged plumes (DP).

3.2 Radiative Forcing

We compute the steady-state effective radiative forcing (ERF) from the integrated O_3 and CH_4 perturbations sustained during the 45-day emission period studied here. The chemical perturbations occur out to 120 days with the remaining O_3 perturbations decaying within a month

but with the accumulated CH_4 perturbations decaying over the perturbation lifetime for global CH_4 of 12.4 years (Prather *et al.*, 2012). The global steady-state δO_3 enhancement per day of emissions is 0.03 DU in both models, calculated from time-integrated perturbation from initial emissions to final decay in DU-days divided by 45 days. At the end of the chemical integration the accumulated δCH_4 perturbations are 11.6 ppt in the CTM and 25.0 ppt in the HMS. To derive the steady-state δCH_4 sustained by the emissions, we divide the accumulated δCH_4 by 45 days and then multiply by 12.4 years to obtain -1.17 ppb and -2.52 ppb respectively.

The O_3 ERF is a combination of the spatially resolved δO_3 in the CTM with the May-to-August averaged ERF kernels from Oslo CTM (Søvde et al., 2012), mapping the Oslo 5.5° resolution onto the 1.1° UCI CTM grid via nearest neighbour interpolation. The per-day O_3 ERF is +1.13 mW m^{-2}. The CH_4 ERF uses the errata-corrected value from IPCC AR6 WGI (550 mW m^{-2} ppm^{-1}), which includes induced stratospheric H_2O and tropospheric O_3 increases, plus tropospheric feedbacks. Thus, the per-day CH_4 ERFs are -0.64 and -1.38 mW m^{-2}, for CTM and HMS respectively. The combined per-day ERFs are therefore +0.49 and -0.25 mW m^{-2}, respectively.

4 Conclusion

We benchmark the production of O_3 and destruction of CH_4 caused by 45 days of South Korean air pollution using the UCI global chemistry-transport model (CTM) against a hybrid modelling system (HMS). The CTM adopts a simplified chemical mechanism designed for clean-air chemistry. The HMS has extremely detailed chemical mechanisms but simplifies the transport and mixing of pollution after it departs the boundary-layer. The models produce similar integrated δO_3 mass perturbations, both equivalent to a steady-state +0.03 DU global enhancement over the 45-day emission period. However, the net O_3 production in the CTM is 71% that of the HMS because of the different O_3 lifetimes in each model. The CTM loss of CH_4

is half that of HMS. Combining O_3 increases (warming) with CH_4 decreases (cooling), the emissions cause net warming in the CTM (+0.49 mW m^{-2} per-day ERF) and net cooling in the HMS (-0.25 mW m^{-2}).

The smaller overall CTM perturbations to both O_3 and CH_4 reactivities are surprising because, nominally, we expect coarser resolution to rapidly dilute NO_x pollution and enhance the GHG reactivities (*e.g.*, Charlton-Perez *et al*., 2009; Holmes *et al.*, 2014). Instead, we find that (1) the Korean NO_x pollution is intense enough to suppress O_3 in some 100-km grid cells, lowering local OPE and enhancing HNO_3 production in the boundary layer and (2) the low VOC reactivity in the CTM causes low PAN yields in the polluted air, hence less NO_x reaches the cleaner atmosphere where OPE and MDE are high. The role of PAN in transporting pollution NO_x to the free troposphere and thus altering the oxidising capacity of the atmosphere is well recognized (e.g., Singh, 1987; Hudman et al., 2004), and this work emphasizes the consequences for the O_3 and CH_4 budgets.

South Korean air pollution is notably rich in aromatic species, which increase PAN (and other organic nitrates) when included in the chemical mechanism (Fischer *et al.*, 2014; Oak *et al.*, 2019), and this is found with our HMS chemistry. Adopting the MCM mechanism in the CTM is not feasible, but introducing aromatic surrogates for toluene and the xylene family would improve OH-VOC chemistry and increase PAN production. The HMS performs a reasonably seamless chemical integration over the boundary-layer and offshore plumes; however, the instantaneous dispersion in the free troposphere creates a sharp discontinuity in the chemical environment which enhances P-O_3 and L-CH_4 to an unknown degree. The transition could instead be mediated by background-air dilution steps, interspersed with chemistry steps, using theoretical dilution timescales (*e.g.*, Prather and Jaffe, 1990). Evaluating the dynamical lifespans

of pollution plumes, *i.e.*, until the onset of rapid background mixing, is a challenging problem and was found to be a major source of uncertainty in HMS budgets (Wilson and Prather, 2026). Another HMS issue is the fixed clean-air boundary condition imposed on free tropospheric air entering the BL; this approach fails to account for transboundary pollution. A time-varying background composition could be derived from assimilated chemical data (*e.g.*, Miyazaki *et al.*, 2019), although such data is limited for species that are not remotely sensed.

Our results suggest that skilful modelling of organic nitrate chemistry is a requirement for obtaining correct CH_4 and O_3 budgets. Field campaigns such as KORUS-AQ and the recent Airborne and Satellite Investigation of Asian Air Quality (ASIA-AQ) mission (Crawford *et al.*, 2022) provide useful model diagnostics (*e.g.* speciated organic nitrates) for atmospheric chemistry simulations in intensely polluted regions. A multi-model ensemble of pollution reactivities supported by airborne campaign data would give further insight into factors controlling the CH_4 and O_3 budgets and the generality of our conclusions here.

Code and data availability

All KORUS-AQ data used in this paper are available via https://doi.org/10.5067/Suborbital/KORUSAQ/DATA01 (KORUSAQ Science Team, 2019). Datasets for the CTM and HMS are available at Wilson (2026a) and Wilson (2026b) respectively.

Author contributions

CW ran the models, analysed the output, and wrote the paper. MP supervised the work, advised on the modelling, and edited the paper.

Competing interests

The contact author has declared that neither of the authors has any competing interests.

Acknowledgements

We acknowledge the Research Cyberinfrastructure Center of the University of California, Irvine, for managing the high-performance computing resources used in this work.

Financial support

This research has been supported by the National Aeronautics and Space Administration (grant no. 80NSSC21K1454) and the National Science Foundation (grant no. AGS-2135749).

References

1. Bloss, C., Wagner, V., Jenkin, M. E., Volkamer, R., Bloss, W. J., Lee, J. D., Heard, D. E., Wirtz, K., Martin-Reviejo, M., Rea, G., Wenger, J. C., and Pilling, M. J.: Development of a detailed chemical mechanism (MCMv3.1) for the atmospheric oxidation of aromatic hydrocarbons, Atmospheric Chemistry and Physics, 5, 641–664, https://doi.org/10.5194/acp-5-641-2005, 2005.
2. Carter, W. P. L.: Development of the SAPRC-07 chemical mechanism, Atmospheric Environment, 44, 5324–5335, https://doi.org/10.1016/j.atmosenv.2010.01.026, 2010.
3. Charlton-Perez, C. L., Evans, M. J., Marsham, J. H., and Esler, J. G.: The impact of resolution on ship plume simulations with NO_x chemistry, Atmospheric Chemistry and Physics, 9, 7505–7518, https://doi.org/10.5194/acp-9-7505-2009, 2009.
4. Chen, Y., Hall, J., van Wees, D., Andela, N., Hantson, S., Giglio, L., van der Werf, G. R., Morton, D. C., and Randerson, J. T.: Multi-decadal trends and variability in burned area from the fifth version of the Global Fire Emissions Database (GFED5), Earth System Science Data, 15, 5227–5259, https://doi.org/10.5194/essd-15-5227-2023, 2023.
5. Crawford, J. H., Ahn, J.-Y., Al-Saadi, J., Chang, L., Emmons, L. K., Kim, J., Lee, G., Park, J.-H., Park, R. J., Woo, J. H., Song, C.-K., Hong, J.-H., Hong, Y.-D., Lefer, B. L., Lee, M., Lee, T., Kim, S., Min, K.-E., Yum, S. S., Shin, H. J., Kim, Y.-W., Choi, J.-S., Park, J.-S., Szykman, J. J., Long, R. W., Jordan, C. E., Simpson, I. J., Fried, A., Dibb, J. E., Cho, S., and Kim, Y. P.: The Korea–United States Air Quality (KORUS-AQ) field study, Elementa: Science of the Anthropocene, 9, 00163, https://doi.org/10.1525/elementa.2020.00163, 2021.
6. Fischer, E. V., Jaffe, D. A., Reidmiller, D. R., and Jaeglé, L.: Meteorological controls on observed peroxyacetyl nitrate at Mount Bachelor during the spring of 2008, Journal of Geophysical Research: Atmospheres, 115, https://doi.org/10.1029/2009JD012776, 2010.
7. Fischer, E. V., Jacob, D. J., Yantosca, R. M., Sulprizio, M. P., Millet, D. B., Mao, J., Paulot, F., Singh, H. B., Roiger, A., Ries, L., Talbot, R. W., Dzepina, K., and Pandey Deolal, S.: Atmospheric peroxyacetyl nitrate (PAN): a global budget and source attribution, Atmos Chem Phys, 14, 2679–2698, https://doi.org/10.5194/acp-14-2679-2014, 2014.
8. Gaubert, B., Emmons, L. K., Raeder, K., Tilmes, S., Miyazaki, K., Arellano Jr., A. F., Elguindi, N., Granier, C., Tang, W., Barré, J., Worden, H. M., Buchholz, R. R., Edwards, D. P., Franke, P., Anderson, J. L., Saunois, M., Schroeder, J., Woo, J.-H., Simpson, I. J.,

Blake, D. R., Meinardi, S., Wennberg, P. O., Crounse, J., Teng, A., Kim, M., Dickerson, R. R., He, H., Ren, X., Pusede, S. E., and Diskin, G. S.: Correcting model biases of CO in East Asia: impact on oxidant distributions during KORUS-AQ, Atmospheric Chemistry and Physics, 20, 14617–14647, https://doi.org/10.5194/acp-20-14617-2020, 2020.

9. Guenther, A. B., Jiang, X., Heald, C. L., Sakulyanontvittaya, T., Duhl, T., Emmons, L. K., and Wang, X.: The Model of Emissions of Gases and Aerosols from Nature version 2.1 (MEGAN2.1): an extended and updated framework for modeling biogenic emissions, Geoscientific Model Development, 5, 1471–1492, https://doi.org/10.5194/gmd-5-1471-2012, 2012.
10. Guo, H., Flynn, C. M., Prather, M. J., Strode, S. A., Steenrod, S. D., Emmons, L., Lacey, F., Lamarque, J.-F., Fiore, A. M., Correa, G., Murray, L. T., Wolfe, G. M., St. Clair, J. M., Kim, M., Crounse, J., Diskin, G., DiGangi, J., Daube, B. C., Commane, R., McKain, K., Peischl, J., Ryerson, T. B., Thompson, C., Hanisco, T. F., Blake, D., Blake, N. J., Apel, E. C., Hornbrook, R. S., Elkins, J. W., Hintsa, E. J., Moore, F. L., and Wofsy, S. C.: Heterogeneity and chemical reactivity of the remote troposphere defined by aircraft measurements – corrected, Atmospheric Chemistry and Physics, 23, 99–117, https://doi.org/10.5194/acp-23-99-2023, 2023.
11. Gaudel, A., Cooper, O. R., Ancellet, G., Barret, B., Boynard, A., Burrows, J. P., Clerbaux, C., Coheur, P.-F., Cuesta, J., Cuevas, E., Doniki, S., Dufour, G., Ebojie, F., Foret, G., Garcia, O., Granados-Muñoz, M. J., Hannigan, J. W., Hase, F., Hassler, B., Huang, G., Hurtmans, D., Jaffe, D., Jones, N., Kalabokas, P., Kerridge, B., Kulawik, S., Latter, B., Leblanc, T., Le Flochmoën, E., Lin, W., Liu, J., Liu, X., Mahieu, E., McClure-Begley, A., Neu, J. L., Osman, M., Palm, M., Petetin, H., Petropavlovskikh, I., Querel, R., Rahpoe, N., Rozanov, A., Schultz, M. G., Schwab, J., Siddans, R., Smale, D., Steinbacher, M., Tanimoto, H., Tarasick, D. W., Thouret, V., Thompson, A. M., Trickl, T., Weatherhead, E., Wespes, C., Worden, H. M., Vigouroux, C., Xu, X., Zeng, G., and Ziemke, J.: Tropospheric Ozone Assessment Report: Present-day distribution and trends of tropospheric ozone relevant to climate and global atmospheric chemistry model evaluation, Elementa: Science of the Anthropocene, 6, 39, https://doi.org/10.1525/elementa.291, 2018.
12. Hoesly, R. M., Smith, S. J., Feng, L., Klimont, Z., Janssens-Maenhout, G., Pitkanen, T., Seibert, J. J., Vu, L., Andres, R. J., Bolt, R. M., Bond, T. C., Dawidowski, L., Kholod, N., Kurokawa, J., Li, M., Liu, L., Lu, Z., Moura, M. C. P., O'Rourke, P. R., and Zhang, Q.: Historical (1750–2014) anthropogenic emissions of reactive gases and aerosols from the Community Emissions Data System (CEDS), Geoscientific Model Development, 11, 369–408, https://doi.org/10.5194/gmd-11-369-2018, 2018.
13. Holmes, C. D., Prather, M. J., and Vinken, G. C. M.: The climate impact of ship NO_x emissions: an improved estimate accounting for plume chemistry, Atmospheric Chemistry and Physics, 14, 6801–6812, https://doi.org/10.5194/acp-14-6801-2014, 2014.
14. Hudman, R. C., Jacob, D. J., Cooper, O. R., Evans, M. J., Heald, C. L., Park, R. J., Fehsenfeld, F., Flocke, F., Holloway, J., Hübler, G., Kita, K., Koike, M., Kondo, Y., Neuman, A., Nowak, J., Oltmans, S., Parrish, D., Roberts, J. M., and Ryerson, T.: Ozone production in transpacific Asian pollution plumes and implications for ozone air quality in California, Journal of Geophysical Research: Atmospheres, 109, https://doi.org/10.1029/2004JD004974, 2004.

15. Isaksen, I. S. A. and Hov, Ø.: Calculation of trends in the tropospheric concentration of O3, OH, CO, CH4 and NOx | Tellus B: Chemical and Physical Meteorology, https://doi.org/10.3402/tellusb.v39i3.15347, 2022.
16. Jacob, D. J., Logan, J. A., Gardner, G. M., Yevich, R. M., Spivakovsky, C. M., Wofsy, S. C., Sillman, S., and Prather, M. J.: Factors regulating ozone over the United States and its export to the global atmosphere, https://doi.org/10.1029/98JD01224, 1993.
17. Jenkin, M. E., Saunders, S. M., and Pilling, M. J.: The tropospheric degradation of volatile organic compounds: a protocol for mechanism development, Atmospheric Environment, 31, 81–104, https://doi.org/10.1016/S1352-2310(96)00105-7, 1997.
18. Jenkin, M. E., Saunders, S. M., Wagner, V., and Pilling, M. J.: Protocol for the development of the Master Chemical Mechanism, MCM v3 (Part B): tropospheric degradation of aromatic volatile organic compounds, Atmospheric Chemistry and Physics, 3, 181–193, https://doi.org/10.5194/acp-3-181-2003, 2003.
19. Jenkin, M. E., Young, J. C., and Rickard, A. R.: The MCM v3.3.1 degradation scheme for isoprene, Atmospheric Chemistry and Physics, 15, 11433–11459, https://doi.org/10.5194/acp-15-11433-2015, 2015.
20. Kim, K.-M., Kim, S.-W., Seo, S., Blake, D. R., Cho, S., Crawford, J. H., Emmons, L. K., Fried, A., Herman, J. R., Hong, J., Jung, J., Pfister, G. G., Weinheimer, A. J., Woo, J.-H., and Zhang, Q.: Sensitivity of the WRF-Chem v4.4 simulations of ozone and formaldehyde and their precursors to multiple bottom-up emission inventories over East Asia during the KORUS-AQ 2016 field campaign, Geoscientific Model Development, 17, 1931–1955, https://doi.org/10.5194/gmd-17-1931-2024, 2024.
21. KORUS-AQ Science Team: KORUS-AQ NASA DC-8 airborne 10 s merged data revision 6 – ICARTT Files, NASA Langley Atmospheric Science Data Center DAAC [data set], https://doi.org/10.5067/Suborbital/KORUSAQ/DATA01, 2019.
22. Li, C., Martin, R. V., Cohen, R. C., Bindle, L., Zhang, D., Chatterjee, D., Weng, H., and Lin, J.: Variable effects of spatial resolution on modeling of nitrogen oxides, Atmospheric Chemistry and Physics, 23, 3031–3049, https://doi.org/10.5194/acp-23-3031-2023, 2023.
23. Liu, S. C., Trainer, M., Fehsenfeld, F. C., Parrish, D. D., Williams, E. J., Fahey, D. W., Hübler, G., and Murphy, P. C.: Ozone production in the rural troposphere and the implications for regional and global ozone distributions, Journal of Geophysical Research: Atmospheres, 92, 4191–4207, https://doi.org/10.1029/JD092iD04p04191, 1987.
24. Miyazaki, K., Sekiya, T., Fu, D., Bowman, K. W., Kulawik, S. S., Sudo, K., Walker, T., Kanaya, Y., Takigawa, M., Ogochi, K., Eskes, H., Boersma, K. F., Thompson, A. M., Gaubert, B., Barre, J., and Emmons, L. K.: Balance of Emission and Dynamical Controls on Ozone During the Korea-United States Air Quality Campaign From Multiconstituent Satellite Data Assimilation, Journal of Geophysical Research: Atmospheres, 124, 387–413, https://doi.org/10.1029/2018JD028912, 2019.
25. Myhre, G., D. Shindell, F.-M. Bréon, W. Collins, J. Fuglestvedt, J. Huang, D. Koch, J.-F. Lamarque, D. Lee, B. Mendoza, T. Nakajima, A. Robock, G. Stephens, T. Takemura and H. Zhang, 2013: Anthropogenic and Natural Radiative Forcing. In: Climate Change 2013: The Physical Science Basis. Contribution of Working Group I to the Fifth Assessment Report of the Intergovernmental Panel on Climate Change [Stocker, T.F., D. Qin, G.-K. Plattner, M. Tignor, S.K. Allen, J. Boschung, A. Nauels, Y. Xia, V. Bex and

P.M. Midgley (eds.)]. Cambridge University Press, Cambridge, United Kingdom and New York, NY, USA.
26. Oak, Y. J., Park, R. J., Schroeder, J. R., Crawford, J. H., Blake, D. R., Weinheimer, A. J., Woo, J.-H., Kim, S.-W., Yeo, H., Fried, A., Wisthaler, A., and Brune, W. H.: Evaluation of simulated O3 production efficiency during the KORUS-AQ campaign: Implications for anthropogenic NOx emissions in Korea, Elementa: Science of the Anthropocene, 7, 56, https://doi.org/10.1525/elementa.394, 2019.
27. Prather, M. J.: The Spillover of Tropospheric Ozone Increases Has Hidden the Extent of Stratospheric Ozone Depletion by Halogens, AGU Advances, 5, e2023AV001154, https://doi.org/10.1029/2023AV001154, 2024.
28. Prather, M. J.: Calibrating the Tropospheric Air and Ozone Mass, AGU Advances, 6, e2025AV001651, https://doi.org/10.1029/2025AV001651, 2025.
29. Prather, M. and Jaffe, A. H.: Global impact of the Antarctic ozone hole: Chemical propagation, Journal of Geophysical Research: Atmospheres, 95, 3473–3492, https://doi.org/10.1029/JD095iD04p03473, 1990.
30. Prather, M. J. and Zhu, X.: Lifetimes and timescales of tropospheric ozone, Elementa: Science of the Anthropocene, 12, 00112, https://doi.org/10.1525/elementa.2023.00112, 2024.
31. Prather, M. J., Holmes, C. D., and Hsu, J.: Reactive greenhouse gas scenarios: Systematic exploration of uncertainties and the role of atmospheric chemistry, Geophysical Research Letters, 39, https://doi.org/10.1029/2012GL051440, 2012.
32. Saunders, S. M., Jenkin, M. E., Derwent, R. G., and Pilling, M. J.: Protocol for the development of the Master Chemical Mechanism, MCM v3 (Part A): tropospheric degradation of non-aromatic volatile organic compounds, Atmospheric Chemistry and Physics, 3, 161–180, https://doi.org/10.5194/acp-3-161-2003, 2003.
33. Saunois, M., Martinez, A., Poulter, B., Zhang, Z., Raymond, P. A., Regnier, P., Canadell, J. G., Jackson, R. B., Patra, P. K., Bousquet, P., Ciais, P., Dlugokencky, E. J., Lan, X., Allen, G. H., Bastviken, D., Beerling, D. J., Belikov, D. A., Blake, D. R., Castaldi, S., Crippa, M., Deemer, B. R., Dennison, F., Etiope, G., Gedney, N., Höglund-Isaksson, L., Holgerson, M. A., Hopcroft, P. O., Hugelius, G., Ito, A., Jain, A. K., Janardanan, R., Johnson, M. S., Kleinen, T., Krummel, P. B., Lauerwald, R., Li, T., Liu, X., McDonald, K. C., Melton, J. R., Mühle, J., Müller, J., Murguia-Flores, F., Niwa, Y., Noce, S., Pan, S., Parker, R. J., Peng, C., Ramonet, M., Riley, W. J., Rocher-Ros, G., Rosentreter, J. A., Sasakawa, M., Segers, A., Smith, S. J., Stanley, E. H., Thanwerdas, J., Tian, H., Tsuruta, A., Tubiello, F. N., Weber, T. S., van der Werf, G. R., Worthy, D. E. J., Xi, Y., Yoshida, Y., Zhang, W., Zheng, B., Zhu, Q., Zhu, Q., and Zhuang, Q.: Global Methane Budget 2000–2020, Earth System Science Data, 17, 1873–1958, https://doi.org/10.5194/essd-17-1873-2025, 2025.
34. Sindelarova, K., Granier, C., Bouarar, I., Guenther, A., Tilmes, S., Stavrakou, T., Müller, J.-F., Kuhn, U., Stefani, P., and Knorr, W.: Global data set of biogenic VOC emissions calculated by the MEGAN model over the last 30 years, Atmospheric Chemistry and Physics, 14, 9317–9341, https://doi.org/10.5194/acp-14-9317-2014, 2014.
35. Singh, H. B.: Reactive nitrogen in the troposphere, Environ. Sci. Technol., 21, 320–327, https://doi.org/10.1021/es00158a001, 1987.
36. Stevenson, D. S., Zhao, A., Naik, V., O'Connor, F. M., Tilmes, S., Zeng, G., Murray, L. T., Collins, W. J., Griffiths, P. T., Shim, S., Horowitz, L. W., Sentman, L. T., and

Emmons, L.: Trends in global tropospheric hydroxyl radical and methane lifetime since 1850 from AerChemMIP, Atmospheric Chemistry and Physics, 20, 12905–12920, https://doi.org/10.5194/acp-20-12905-2020, 2020.
37. Szopa, S., V. Naik, B. Adhikary, P. Artaxo, T. Berntsen, W.D. Collins, S. Fuzzi, L. Gallardo, A. Kiendler-Scharr, Z. Klimont, H. Liao, N. Unger, and P. Zanis, 2021: Short-Lived Climate Forcers. In Climate Change 2021: The Physical Science Basis. Contribution of Working Group I to the Sixth Assessment Report of the Intergovernmental Panel on Climate Change [Masson-Delmotte, V., P. Zhai, A. Pirani, S.L. Connors, C. Péan, S. Berger, N. Caud, Y. Chen, L. Goldfarb, M.I. Gomis, M. Huang, K. Leitzell, E. Lonnoy, J.B.R. Matthews, T.K. Maycock, T. Waterfield, O. Yelekçi, R. Yu, and B. Zhou (eds.)]. Cambridge University Press, Cambridge, United Kingdom and New York, NY, USA, pp. 817–922, doi: 10.1017/9781009157896.008.
38. Wild, O., Prather, M. J., Akimoto, H., Sundet, J. K., Isaksen, I. S. A., Crawford, J. H., Davis, D. D., Avery, M. A., Kondo, Y., Sachse, G. W., and Sandholm, S. T.: Chemical transport model ozone simulations for spring 2001 over the western Pacific: Regional ozone production and its global impacts, Journal of Geophysical Research: Atmospheres, 109, https://doi.org/10.1029/2003JD004041, 2004.
39. Wilson, C.: Methane loss (L-CH_4) and tropospheric ozone (O_3) burden in response to a 10% KORUS-AQ emission perturbation in the UCI chemistry-transport model, Dryad [dataset], https://doi.org/10.5061/dryad.djh9w0wgm, 2026a.
40. Wilson, C.: Modelling system for computing the tropospheric O3 and CH4 perturbations from South Korean Emissions
41. (KORUS-AQ period), Dryad [code], https://doi.org/10.5061/dryad.f4qrfj78x, 2026b.
42. Wilson, C. P. and Prather, M. J.: Life–cycle impacts of South Korean air pollution on tropospheric ozone and methane: sensitivity to dispersion time, Atmospheric Chemistry and Physics, 26, 3995–4017, https://doi.org/10.5194/acp-26-3995-2026, 2026.
43. Woo, J.-H., Kim, Y., Kim, H.-K., Choi, K.-C., Eum, J.-H., Lee, J.-B., Lim, J.-H., Kim, J., and Seong, M.: Development of the CREATE Inventory in Support of Integrated Climate and Air Quality Modeling for Asia, Sustainability, 12, 7930, https://doi.org/10.3390/su12197930, 2020.
44. Zakoura, M. and Pandis, S. N.: Overprediction of aerosol nitrate by chemical transport models: The role of grid resolution, Atmospheric Environment, 187, 390–400, https://doi.org/10.1016/j.atmosenv.2018.05.066, 2018.
45. Ziemke, J. R., Oman, L. D., Strode, S. A., Douglass, A. R., Olsen, M. A., McPeters, R. D., Bhartia, P. K., Froidevaux, L., Labow, G. J., Witte, J. C., Thompson, A. M., Haffner, D. P., Kramarova, N. A., Frith, S. M., Huang, L.-K., Jaross, G. R., Seftor, C. J., Deland, M. T., and Taylor, S. L.: Trends in global tropospheric ozone inferred from a composite record of TOMS/OMI/MLS/OMPS satellite measurements and the MERRA-2 GMI simulation, Atmospheric Chemistry and Physics, 19, 3257–3269, https://doi.org/10.5194/acp-19-3257-2019, 2019.

Chapter 5: Coauthored publication "Projecting nitrous oxide over the 21st century, uncertainty related to stratospheric loss"

Citation

Prather, M. J. and Wilson, C. P.: Projecting nitrous oxide over the 21st century, uncertainty related to stratospheric loss, Proceedings of the National Academy of Sciences, 123, e2524123123, https://doi.org/10.1073/pnas.2524123123, 2026.

Abstract

Extending the N_2O lifetime derived from Microwave Limb Sounder satellite observations, we find a mean value of 117 y and a likely decrease of –1.4 ± 0.9% per decade over the period 2004 to 2024. This trend is consistent with the previously published 2004 to 2021 value of –2.1 ± 1.2% per decade. A more careful analysis of uncertainty now provides a more robust likely (one-sigma) range. From analyses of a range of factors controlling the N_2O lifetime, we find that the decrease in lifetime can be explained by recent changes in stratospheric circulation and temperature. Projection of the lifetime change to 2100 shows that this effect is comparable to differences across the shared socioeconomic pathways used for climate projections and cannot be ignored. An updated evaluation of the N_2O chemical feedbacks shows that this effect produces a relatively small shift in atmospheric abundance over the 21st century, but still an important shift, –11%, in the global warming potential of N_2O.

References

1. Prather, M. J. and Wilson, C. P.: Projecting nitrous oxide over the 21st century, uncertainty related to stratospheric loss, Proceedings of the National Academy of Sciences, 123, e2524123123, https://doi.org/10.1073/pnas.2524123123, 2026.

Chapter 6: Conclusion

This dissertation compiles new science on GHG reactivity caused by intense air pollution. Chapter 2 quantifies the accuracy and predictive capability of the interpolated KORUS-AQ surface data fields against ground and air observations, revealing regions that are sufficiently or insufficiently monitored for model diagnostics. Chapter 3 models South Korean summertime emissions in high chemical detail using the specialised HMS, finding they significantly increase O_3 and decrease CH_4 in the global troposphere. The magnitudes of the GHG reactivities are greatly amplified when shorter (e.g., 1 day) dynamical lifetimes are prescribed for pollution plumes before dispersion. Chapter 4 reveals agreement between the UCI CTM and HMS on the integrated O_3 mass enhancement by the pollution but computes less P-O_3 and L-CH_4 in the CTM by factors of 71% and 47% respectively. This result is surprising because typically, the coarser resolution and divergent transport in the CTM is expected to amplify P-O_3 and L-CH_4. We attribute the GHG reactivities to low VOC reactivity and insufficient organic nitrate formation in the CTM. The 45-day emission period ultimately causes net GHG warming in the CTM and net cooling in the HMS, sustaining annual ERFs of +0.49 mW m^{-2} and -0.25 mW m^{-2} respectively. Chapter 5 (coauthored) finds a continued downward trend in the lifetime of N_2O which is consistent with hastening tropical upwelling and cooling stratospheric temperatures. The previous and updated lifetime trends lead to diverged projections of N_2O abundance by the year 2100, with similar separation to fixed-lifetime projections under alternate shared socioeconomic pathways.

Chapters 3 and 4 suggest that modelling realistic CH_4 and O_3 budgets requires the good numerical modelling of pollution plumes with realistic dispersion timescales, while sequestering NO_x to organic nitrates at the appropriate rates. A simplistic scaling of P-O_3 and L-CH_4 in the

HMS to global NO_x emissions (x100) and 365 days (x365/45) would suggest 30% of global P-O_3 and 10% of L-CH_4 is attributable to anthropogenic air pollution. The ERFs from global air pollution would represent additions of -0.5% and +1.3% to the present-day ERF by anthropogenic GHG (3.8 W m^{-2}; Forster *et al*., 2021). The global air pollution ERFs estimated here are small; however, intense pollution could represent a large missing source of O_3 and sink of CH_4 in global models if they are not well-simulated. This extrapolation is tenuous however, as atmospheric chemistry rates depend on temperature and solar radiation. In winter, the loss of Eastern Chinese NO_x is mainly by heterogeneous N_2O_5 reactivity, and the NO_x lifetime (3.6 days) depends on the availability of O_3 at night (Shah *et al*., 2020). We could obtain winter HMS budgets by rescaling the KORUS-AQ all-sky J-values to winter cloud conditions. However, the prolonged NO_x lifetime in winter suggests 3D plume transport is more important to the resultant GHG budgets than in summer. Aerosol surface area density may limit the loss of NO_x pollution in some instances, and the HMS does not currently simulate physical aerosol processes.

Better agreement between the CTM and HMS budgets might be attained by adding one or more aromatic surrogates to the CTM. This would promote more realistic VOC reactivity and improve the PAN budget. A simplified oxidation scheme for toluene and xylene has been proposed by Porter *et al*. (2017), which we could implement by adding CTM species to represent toluene (xylene) and the toluene-O_2 (xylene-O_2) adduct following reaction with OH. The adduct decomposition products proposed for GEOS-Chem could be substituted with functionally analogous UCI CTM tracers (*i.e*, glyoxal := HCHO; methylglyoxal and unsaturated dicarbonyl := acetaldehyde).

Further insight on the chemical drivers of the pollution-driven GHG budgets could be gained from a multimodel ensemble perturbed by KORUS-AQ emissions. It would be interesting to

evaluate models with more sophisticated VOC chemistry against the HMS. Hence, we could compute the GHG budgets resulting from a global emission perturbation in the multimodel ensemble and evaluate the budgets using findings from the KORUS-AQ study. Agreement with the HMS might be fortuitous however, as coarse emission resolution and numerical diffusion are another likely source of error in CTMs suggested by our work. Testing the convergence of L-CH_4 and P-O_3 in a CTM under various grid refinements would reveal the magnitude of the error caused by coarse resolution, though at great computational expense.

The 2024 Airborne and Satellite Investigation of Asian Air Quality (ASIA-AQ) mission presents an opportunity to extend our HMS budgets to Taiwan, Thailand, and the Philippines. Hence, we could test the representativeness of our KORUS-AQ budgets to neighbouring countries. The current HMS version is not equipped to simulate pollution plumes from the inner continent because such plumes are presumably lifted to the free troposphere via deep convection and orography, and these dynamics are missing. Additionally, the dynamical lifetime of pollution plumes is a model uncertainty in the HMS, and the actual aging and dispersion characteristics of transboundary pollution plumes remain unknown to us. Obtaining these statistics may require future airborne campaigns with niche sampling patterns to intercept urban pollution over a range of downwind distances.

The results from this dissertation will hopefully support efforts to evaluate and improve GHG chemistry modelling in the highly polluted domain, thereby improving the CH_4 and tropospheric O_3 budget calculation.

References

1. Forster, P., T. Storelvmo, K. Armour, W. Collins, J.-L. Dufresne, D. Frame, D.J. Lunt, T. Mauritsen, M.D. Palmer, M. Watanabe, M. Wild, and H. Zhang, 2021: The Earth's Energy Budget, Climate Feedbacks, and Climate Sensitivity. In Climate Change 2021: The Physical Science Basis. Contribution of Working Group I to the Sixth Assessment

Report of the Intergovernmental Panel on Climate Change [Masson-Delmotte, V., P. Zhai, A. Pirani, S.L.
2. Porter, W. C., Safieddine, S. A., and Heald, C. L.: Impact of aromatics and monoterpenes on simulated tropospheric ozone and total OH reactivity, Atmospheric Environment, 169, 250–257, https://doi.org/10.1016/j.atmosenv.2017.08.048, 2017.
3. Shah, V., Jacob, D. J., Li, K., Silvern, R. F., Zhai, S., Liu, M., Lin, J., and Zhang, Q.: Effect of changing NO_x lifetime on the seasonality and long-term trends of satellite-observed tropospheric NO_2 columns over China, Atmospheric Chemistry and Physics, 20, 1483–1495, https://doi.org/10.5194/acp-20-1483-2020, 2020.